[21] E.E. Underwood: *Quantitative Stereology*, Addison-Wesley, Reading, Mass, 1970.

[22] G.E. Ice: in *ASM Handbook, Vol. 9 Metallography and Microstructure*, G.F. Vander Voort, eds., ASM International, Materials Park, OH, 2009

[23] Y. Murakami, T. Toriyama, E.M. Coudert: *JTEVA*, 1994, 22, pp. 318-326.

[24] J.C. Russ, R.T. Dehoff: *Practical Stereology*, Kluwer Academic/Plenum Publishers, 2000.

[25] L.M. Karlsson and L.M. Cruz-Orive: *J. Microsc.*, 1992, 165, pp. 391-415.

[26] J-Y. Buffière, S. Savelli, P.H. Jouneau, E. Maire, and R. Fougères: Mater. Sci. Eng., 2001, A316, pp. 115-126.

[27] T. Link, S. Zabler, A. Epishin, A. Haibel, M. Bansal, and X. Thibault: *Mater. Sci. Eng. A*, 2006, 425A, pp. 47-54.

[28] W. Weibull: *Fatigue Testing and Analysis of Results*, Pergamon Press, Oxford, UK, 1961.

[29] Y. Murakami and H. Usuki: *Int. J. Fatigue*, 1989, 11, pp. 299-307.

[30] Y. Murakami: *J. Res. Natl. Inst. Stand. Technol.*, 1994, 99, pp. 345-351.

[31] Y. Murakami, S. Kodama, and S. Konuma: *Int. J. Fatigue*, 1989, 11. pp. 291-298.

[32] E.J. Gumbel: *Statistics of Extremes*, Columbia University Press, New York, 1957.

[33] S. Beretta and S. Matteazzi: *Int. J. Fatigue*, 1996, 18, pp. 451-456.

[34] T. Seki: *Aichi Steel Techn. Report*, 1995, 15, pp. 24-29.

[35] H.J.G. Gundersen: *APMIS*, 1988, 96, pp. 379-394.

[36] E.J. Gumbel: *Statistics of Extremes*, Columbia University Press, 1958.

[37] S. Tin, T.M. Pollock and W.T. King: in *Superalloys 2000*, T.M. Pollock, R.D. Kissinger, R.R. Bowman, K.A. Green, M. McLean, S.L. Olson, and J.J. Schirra eds., Seven Springs, PA, TMS, 2000, pp. 201-210.

[38] K.A. Al-Jarba and G.E. Fuchs: *Mat. Sci. Eng. A*, 2004, 373, pp. 255-267.

[39] J.M. Barsom and J.M. McNicol, *ASTM STP-559*, 1974, pp. 183-204.

[40] G.T. Cashman: *J. of Eng. Mat. Tech.*, 2007, 129, pp. 293-303.

[41] D. Ma: *Metall. Mater. Trans. B*, 2002, 33, pp. 223.

[42] D.G. McCartney and J.D. Hunt: *Acta Metall.*, 1981, 29, pp. 1851-1863.

[43]   D.R. Poirier, K. Yeum, and A. Maples: *Metall. Mater. Trans*, 1987, 18, pp. 1979.

[44]   H.W. Whitesell and R.A. Overfelt: *Mat. Sci. Eng. A,* 2001, 318, pp 264-276.

[45]   J. C. Heinrich and D. R. Poirier: *C.R. Mecanique*, 2004, 332, pp. 429-45

Chapter 5

FATIGUE BEHAVIOR

In Chapter 4, it was shown that primary dendrite arm spacings were refined by approximately 50 pct using the LMC process in comparison to the conventional Bridgman process. A range in primary dendrite arm spacings and pore sizes was observed in both processes, with narrower distributions in the LMC solidified material. This chapter addresses the influence of microstructural refinement and variability in dendritic spacings on low cycle fatigue (LCF). René N5 and René N5 modified alloys using the two optimum solidification rates (LMC—12.7 mm/min and Bridgman—3.4 mm/min) were subjected to fatigue testing at 538°C. Fracture surfaces were characterized using scanning electron microscopy (SEM) to understand the deformation and damage micromechanisms that occurred during strain-controlled LCF. The nature of fatigue crack initiation in the single-crystal materials is discussed in this chapter and further fatigue crack growth analysis is presented in Chapter 6. Statistics of extreme values were used to compare the predicted pore sizes from metallographic sections to actual initiation sizes. These observations and analyses are used to construct a micromechanical model for fatigue life prediction that is presented in Chapter 7.

5.1   Fatigue Life Assessment

Strain-controlled low cycle fatigue testing was conducted at 538°C ($R = 0$), at total strain ranges between 0.6-1.1% on samples solidified at 3.4 mm/min and 12.7 mm/min withdrawal rates using the Bridgman and LMC processes, respectively. Results for these strain-controlled tests for René alloys have typically been summarized based on an alternating (pseudo) stress, σ_P defined as follows (also shown in Chapter 2):

$$\sigma_P = \frac{\Delta\varepsilon_t E}{2} \qquad\qquad\qquad [5.1]$$

where E is the elastic modulus determined from the test, and $\Delta\varepsilon_t$ is the total strain range in mm/mm. The alternating (pseudo) stress for the fatigue damage parameter is commonly used to present S-N results for strain cycle fatigue at GE Aviation in order to compare the fatigue properties of single crystals with varying orientations, and thus varying elastic modulus.

For single crystal nickel-base superalloys, the elastic modulus varies with crystallographic orientation. For example, a deviation of more than 15° with the [001] crystal axis and the tensile axis produced up to an 8% increase in E in the samples tested. The targeted alternating (pseudo) stress levels included 380 MPa, 448 MPa, 482 MPa, 551 MPa and 620 MPa, which gave various strain range levels depending on the elastic modulus for the particular specimen. The σ_P is typically determined at $N_f/2$, or at one-half the specimen life. The S-N results are presented in Figure 5.1, where the alternating (pseudo) stress is plotted as a function of the number of cycles to failure for the four variants. All results in this chapter will be presented in terms of σ_{ALT}, which is actually the alternating (pseudo) stress in units of MPa. The actual alternating (pseudo) stresses are shown in Figure 5.1 and Table 5.1, but for comparison of the fatigue lives, the targeted alternating (pseudo) stresses are indicated in most figures.

Modified-Ta René N5 fatigue lives were evaluated for samples solidified with LMC (12.7 mm/min) and Bridgman (3.4 mm/min) processes to investigate the role of increasing the resistance to shearing of γ′ precipitates during the fatigue process. The material solidified with the LMC casting process had a 3 to 7-fold increase in fatigue life, depending on the stress level.
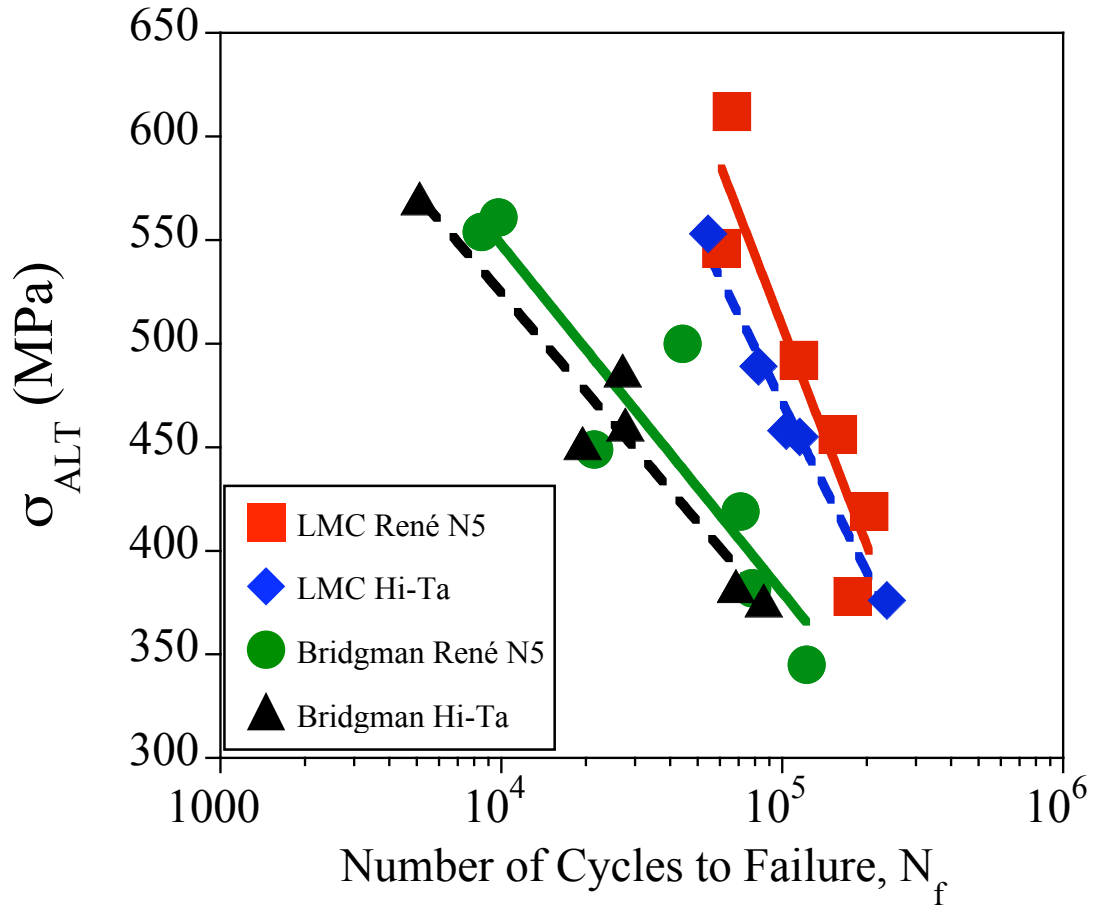
Figure 5.1 S-N curves for investigated alloys tested at 538°C, $R = 0$, f =0.5 Hz.

Table 5.1 S-N results of LMC and Bridgman solidified alloys tested at 538°C, $R = 0$, $f = 0.5$ Hz.

Variant	σ_{ALT} (MPa)	Cycles to Failure	Initiation Site Diameter (μm)
LMC N5	612	66,365	32.0
LMC N5	546	60,724	29.3
LMC N5	492	114,934	14.7
LMC N5	456	157,764	22.6
LMC N5	378	178,429	31.4
LMC N5	419	204,131	25.6
LMC Hi-Ta	553	54,534	38.5
LMC Hi-Ta	489	82,532	20.6
LMC Hi-Ta	458	103,532	25.2
LMC Hi-Ta	455	115,442	20.3
LMC Hi-Ta	376	236,218	22.1
Bridgman N5	561	9,763	54.4
Bridgman N5	554	8,499	48.9
Bridgman N5	500	44,180	73.4
Bridgman N5	449	21,410	50.4
Bridgman N5	419	70,933	59.6
Bridgman N5	382	78,180	55.0
Bridgman N5	345	122,153	36.1
Bridgman Hi-Ta	570	5,135	88.6
Bridgman Hi-Ta	487	27,063	61.8
Bridgman Hi-Ta	461	27,650	93.0
Bridgman Hi-Ta	452	19,497	73.2
Bridgman Hi-Ta	376	86,216	75.7
Bridgman Hi-Ta	383	68,500	99.5

To investigate the benefit of Ta addition on the fatigue resistance, the σ_{ALT} was normalized by the ambient temperature yield stress, Figure 5.2. Sengupta and co-workers have shown that the yield stress increases by less than 10 pct at 538°C in comparison to ambient temperature for CMSX-4.[1] The Hi-Ta material exhibited lower normalized fatigue strength in comparison to the N5 material; this is due to larger pores in this variant of material. From this it is evident that Ta addition to the N5 composition increases the fatigue strength by increasing the resistance to shearing of γ′ precipitates, providing a 2-3X increase in fatigue life. Overall, Figures 5.1 and 5.2 demonstrate a significant benefit of refining the dendritic structure using the LMC process.
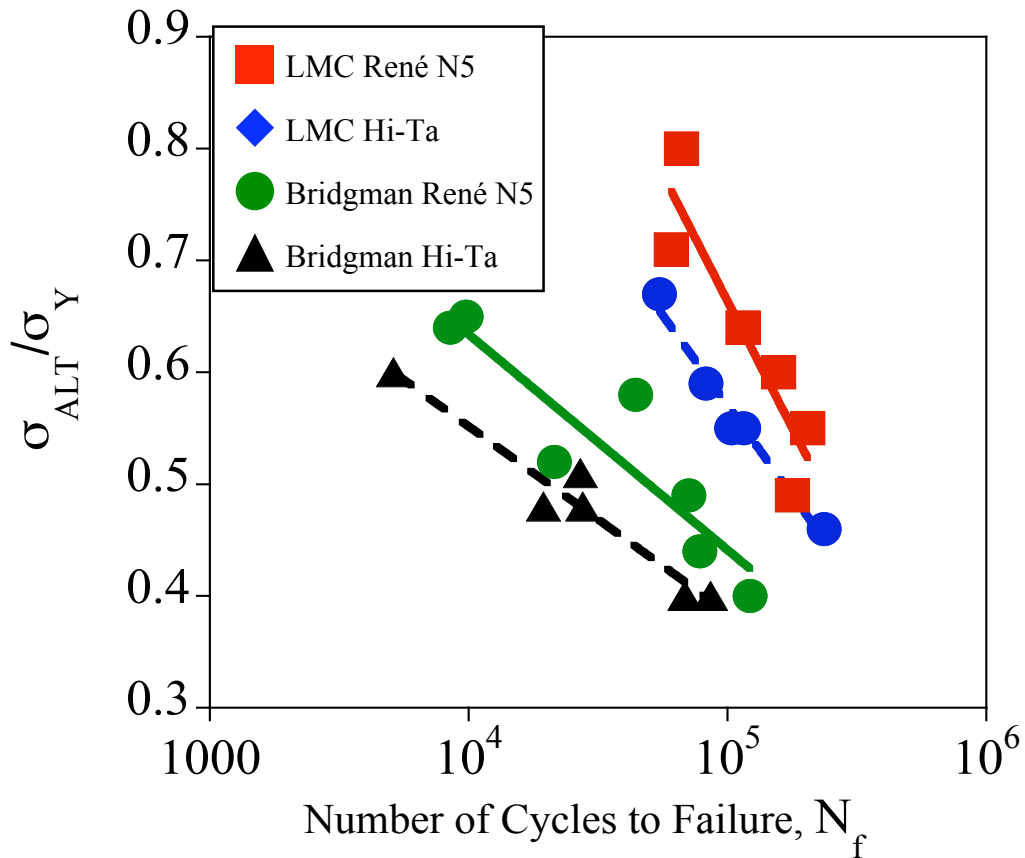
**Figure 5.2 Fatigue life (538°C, $R = 0$) for René N5 and modified alloys normalized with the yield stress.**

Table 5.2 Room temperature yield strengths for LMC (12.7 mm/min) and Bridgman (3.4 mm/min) solidified material.

| Variant	LMC N5	LMC Hi-Ta	Bridgman N5	Bridgman Hi-Ta
σ_Y (MPa)	770	880	820	950

5.1.1 Fractographic Analysis

In order to identify the life limiting features during fatigue of the René N5 alloys, fractography was performed on all failed samples. Cracks were found to initiate from casting pores for all of the investigated alloys, at internal and near-to surface locations. The equivalent circular diameter, d (Equation 5.2), and corresponding distance from the surface, t, was measured from each site. The distance was measured from the center of the pore to the free surface. A method for differentiating between surface and internal pores has been described by Murakami and was used here.[2] Specifically, if $d/t \geq 1.6$, the pore was determined as a near-to-surface pore; if $d/t < 6$, the pore was determined as an internal location. A SEM image of a representative fracture surface is shown in Figure 5.3a, with a large casting pore magnified in Figure 5.3b, for a sample tested with an alternating stress of 551 MPa. The cracks that initiated from pore sites at internal locations were inclined approximately 45° to the [001] direction. These faceted crack planes were observed in various proportions on the fracture surface, which has also been exhibited in other single-crystal alloys under similar testing conditions.[3,4] Chapter 6 will show that crack propagation within these materials occurs along {111}-type crystallographic planes.

(a)   (b)

(c)   (d)
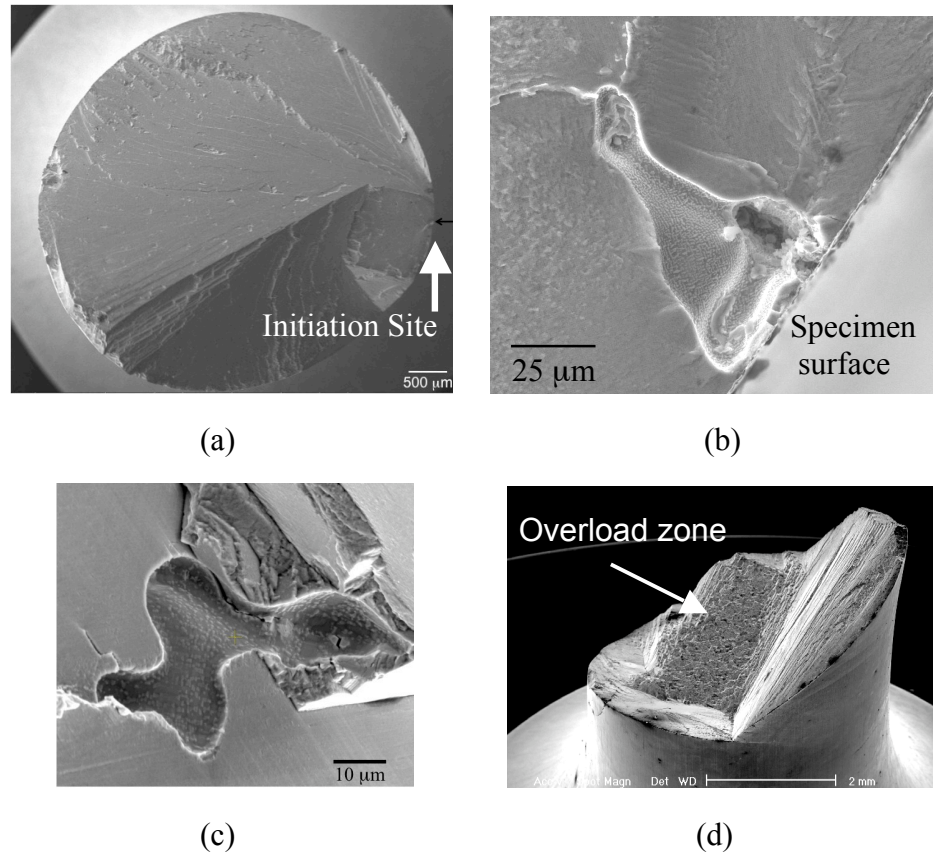
Figure 5.3 Various features of fracture surfaces of LMC and Bridgman René N5 solidified bars. (a) [001] view of a fracture surface from a Bridgman René solidified bar and (b) the corresponding initiation site at the surface (σ_{ALT} = 561 MPa, N_f = 9,763 cycles), (c) a highly magnified view of an internal initiating pore within a LMC René N5 solidified sample (σ_{ALT} = 546 MPa, N_f = 60,724 cycles) and (d) inclined facets on the surface of a LMC solidified specimen (σ_{ALT} = 456 MPa, N_f = 157,764 cycles).

The fracture planes were likely parallel to one or more of the octahedral slip systems {111}(110), characteristic of FCC single crystals. These octahedral slip systems are known to be active at temperatures less than 760°C.[5] Specimens for which fatal cracks initiated from pores at internal locations and at the lower stress levels accumulated more cycles to failure in comparison to surface initiations. Figure 5.4 shows two initiation cases: (a) a pore initiating a crack along a single plane, and (b) a pore at the intersection of three or more distinctive crystallographic planes. Cracking along a single plane indicates a dominance of one slip system during the initiation process. Alternatively, to crack initiation along a {111} octahedral plane, cracks initiated in a Mode I behavior from near-to-surface pores (Figure 5.3a) at high stress levels.

<center>(a)   (b)</center>
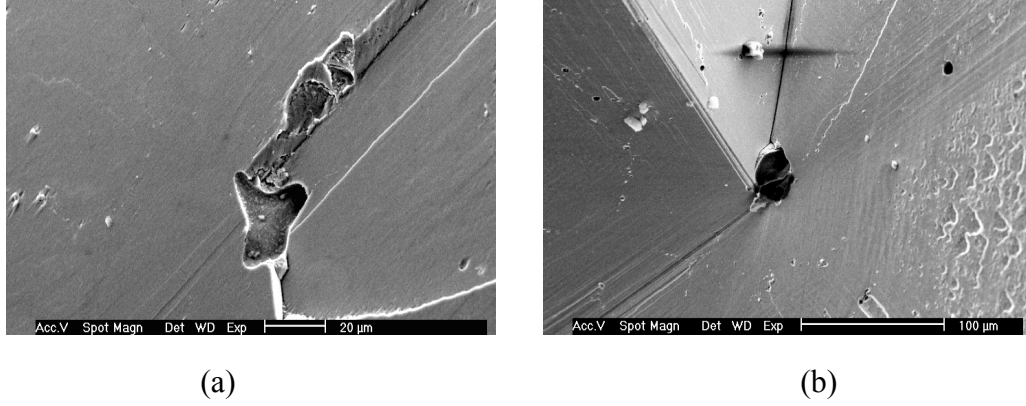
Figure 5.4 Pores initiating crack growth on (a) single crystallographic facet *(σ$_{ALT}$* = 446 MPa, N$_f$ = 157,764 cycles) and (b) multiple {111} crystallographic facets *(σ$_{ALT}$* = 380 MPa, N$_f$ = 178,429 cycles) within LMC solidified material.

Secondary electron images in Figure 5.5 show various casting pores that initiated fatigue cracks at specific alternating stresses. The initiating pore size was measured from [001] projected areas, using an equivalent circular diameter (ECD), *d*, as

$$d = \sqrt{\frac{4 * Area}{\pi}} \qquad\qquad [5.2]$$

Pore shapes were characterized using an aspect ratio, *F*, which is a function of the largest diameter, *d$_{max}$*, and smallest diameter, *d$_{min}$*, orthogonal to it:

$$F = \frac{d_{min}}{d_{max}} \qquad\qquad [5.3]$$

An aspect ratio, also known as shape factor, of 1 represents a circular pore in the plane of analysis, while values closer to 0 denote irregular shapes. Table 5.3 summarizes selected initiation site sizes and aspect ratios for the conditions tested. The René N5 alloy cast using the LMC process initiated cracks at the smallest pores and largest shape factor values, and typical pore shapes are shown in Figure 5.4 and 5.5a. More irregularly shaped, larger pores initiated cracks in the Bridgman cast material (Figure 5.5b), which significantly reduced the fatigue life.

The LMC René N5 solidified material produced the smallest initiation site sizes, followed by the LMC Hi-Ta, Bridgman René N5 and Bridgman Hi-Ta alloys. This trend in increasing pore size was also observed in metallographic measurements presented in

<center>110</center>

Figure 4.15. Larger maximum pore sizes were found in as-cast metallographically prepared samples within the LMC solidified material than what was found to initiate cracks in the fatigue specimens. Alternatively, larger pores were found to initiate cracks in the Bridgman solidified material than what was observed with metallography. In four samples, initiation sites were composed of adjacent pores, which initiated cracks in the Bridgman René N5 solidified material. One such case is shown in Figure 5.5c for the initiation site at a near-to-surface location. Adjacent pores were defined as having an edge distance no greater than the average SDAS for the material. Consequently, these adjacent pores produced the largest site sizes measured for the Bridgman tested bars. The largest initiation site diameter totaled to 99.5 μm, which was from three interconnected pores (42 μm, 61 μm and 65 μm) within a Hi-Ta modified alloy produced with Bridgman casting. These interconnected pores are especially detrimental to the fatigue life given that they amplify the stress intensity within the pore site vicinity. Rarely will these defect sizes be observed in metallographic sections. This poses a challenge for predicting maximum site sizes using the SEV approach described in Chapter 4.

|		
(a)	(b)	(c)
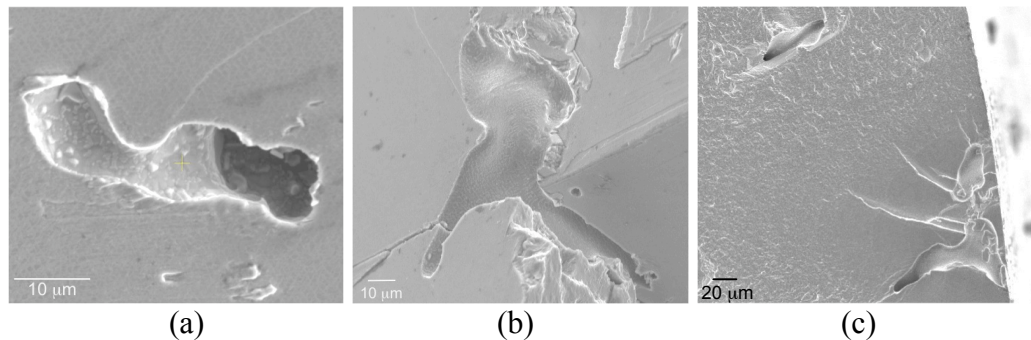
Figure 5.5 Typical pores from which fatigue cracks initiated. (a) A smaller pore developed during the LMC process initiated cracking from an internal location (σ_{ALT} = 455 MPa, N_f = 115,442 cycles). (b) An irregular shaped pore nucleated during Bridgman solidification initiated fatigue cracking (σ_{ALT} = 382 MPa, N_f = 78,180 cycles), and (c) multiple casting pores initiated fracture near the surface (σ_{ALT} = 452 MPa, N_f = 19,497 cycles).

It should be noted that since the maximum pore size was shown to scale with the primary and secondary dendrite arm spacings in Chapter 4, it is apparent that the refinement in spacings using the LMC process was the major contributing factor to increasing the fatigue life of the alloys. Figure 5.6 shows each initiation site diameter as

a function of the alternating stress level for all samples tested. Open symbols represent near-to-surface initiations, which only occurred in Bridgman tested material.

Table 5.3 Summary of fatigue crack initiation site sizes for LMC and Bridgman cast bars.

Processing Condition	Alloy	Maximum Initiation Site Diameter (μm)	Minimum Initiation Site Diameter (μm)	Pore Aspect Ratio Range
LMC	René N5	32	15	0.19-0.69
LMC	Hi-Ta	38	20	0.12-0.41
Bridgman	René N5	73	36	0.10-0.29
Bridgman	Hi-Ta	99	62	0.03-0.24
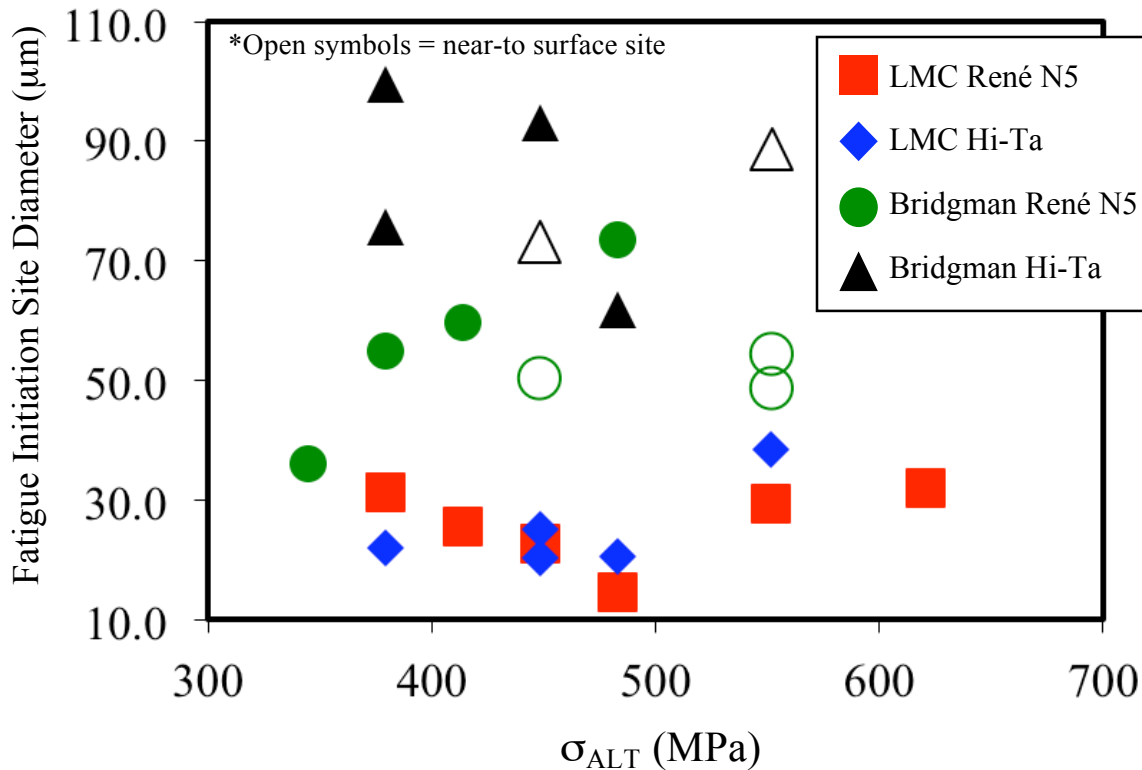
Figure 5.6 Measurements of fatigue initiation site sizes measured from fracture surfaces. Each site size is plotted against its representative applied stress level. Open symbols represent near-to-surface sites.

A decrease in fatigue life was produced with increasing pore size for the four variants shown in Figure 5.7 at $\sigma_{ALT} \sim 448$ MPa. A Bridgman Hi-Ta sample containing a pore diameter of 93 μm initiated a crack internally and produced a longer life in comparison to the samples that initiated cracks at near-to-surface pores. Each fatigue

initiation site presented in Figure 5.7 is shown in Figure 5.8 (right-hand column, A-F), with the corresponding fracture surfaces shown in the left-hand column. Arrows indicate the initiation site for each specimen. Slip offsets were observed near pore surfaces, shown in fractographs A and F of Figure 5.8 (right-hand column).

Figure 5.9 shows the effect of pore diameter on fatigue life for three stress levels tested. Open symbols represent near-to-surface crack initiation sites. A similar effect of pore diameter on the fatigue life was exhibited at stress levels of 448 MPa and 482 MPa.
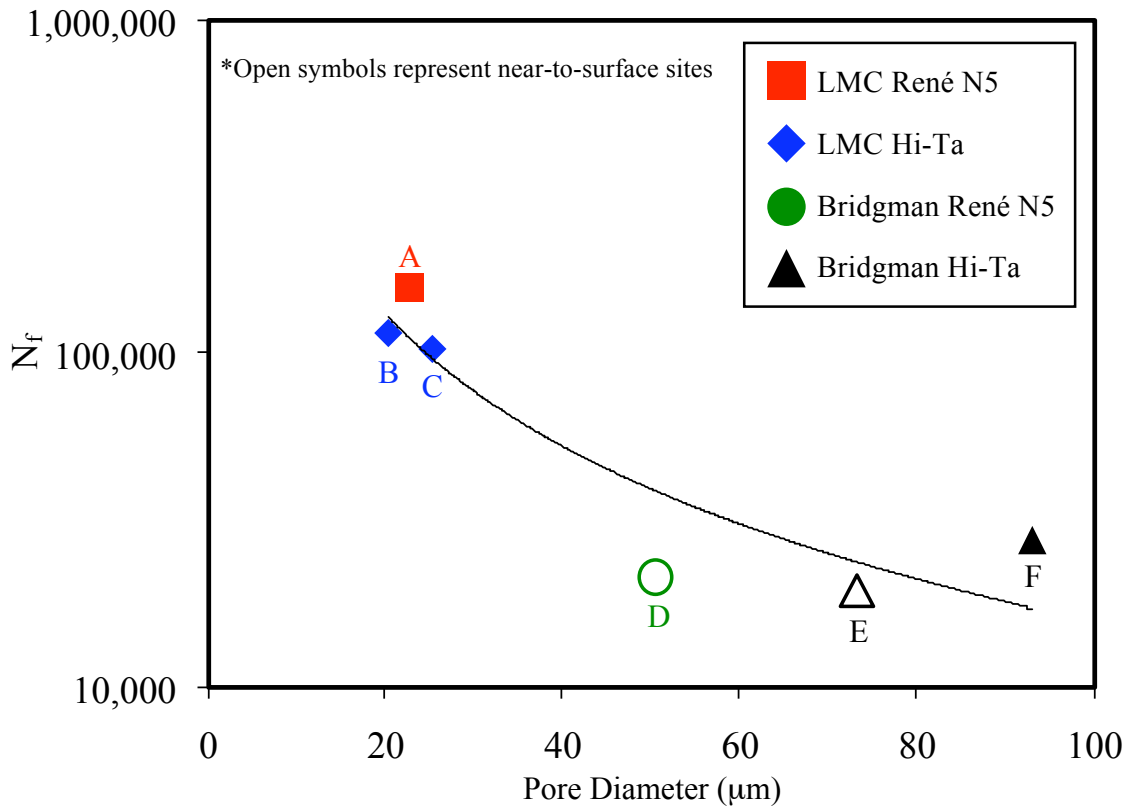
Figure 5.7 Effect of surface pore diameter on the fatigue life of René N5 alloys at a $\sigma_{ALT} \sim$ 448 MPa. Open symbols represent near-to-surface sites.
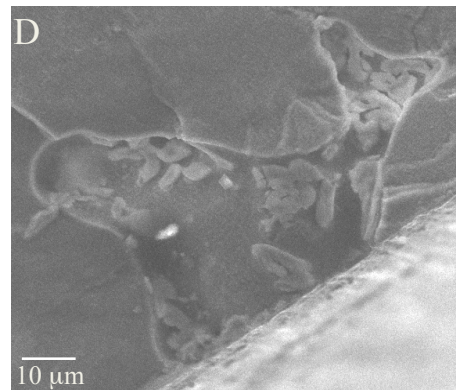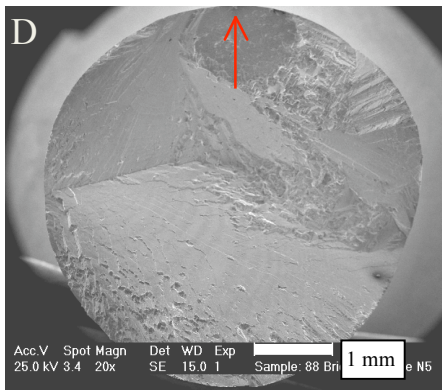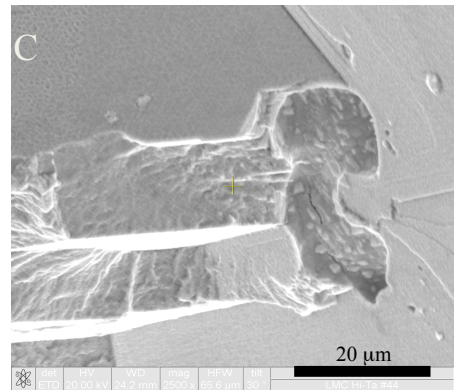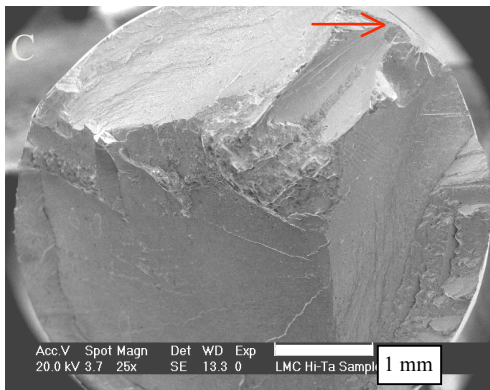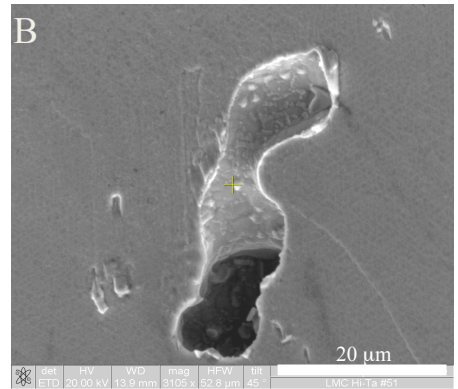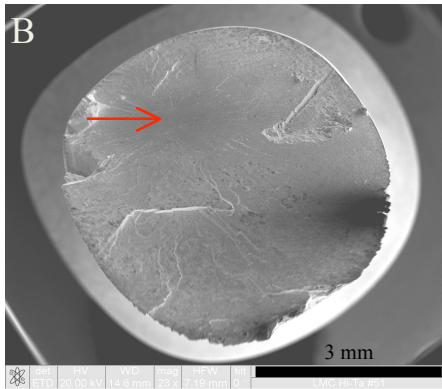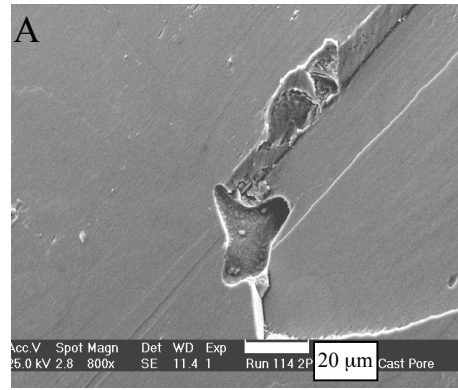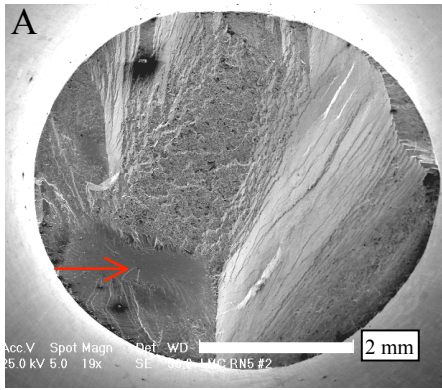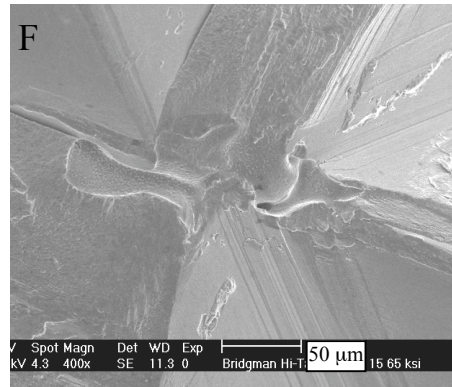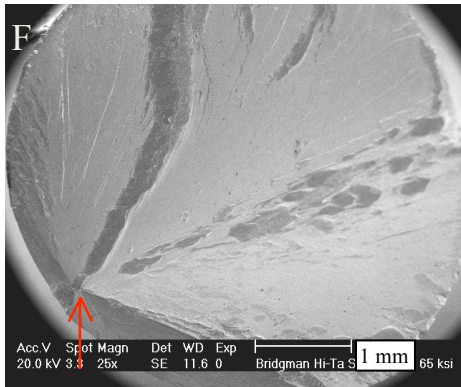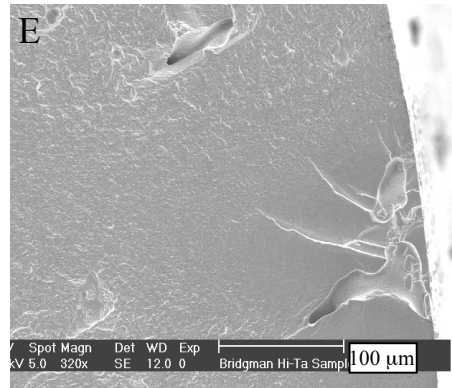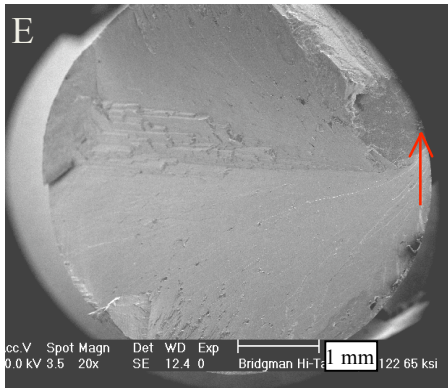
Figure 5.8 Fractographs of fatigue initiating pore sites (right hand column) and the corresponding full fracture surface (left hand column) for samples A-F shown in Figure 5.7. Samples were tested at $\sigma_{ALT} \sim$ 448 MPa at 538°C, R = 0.
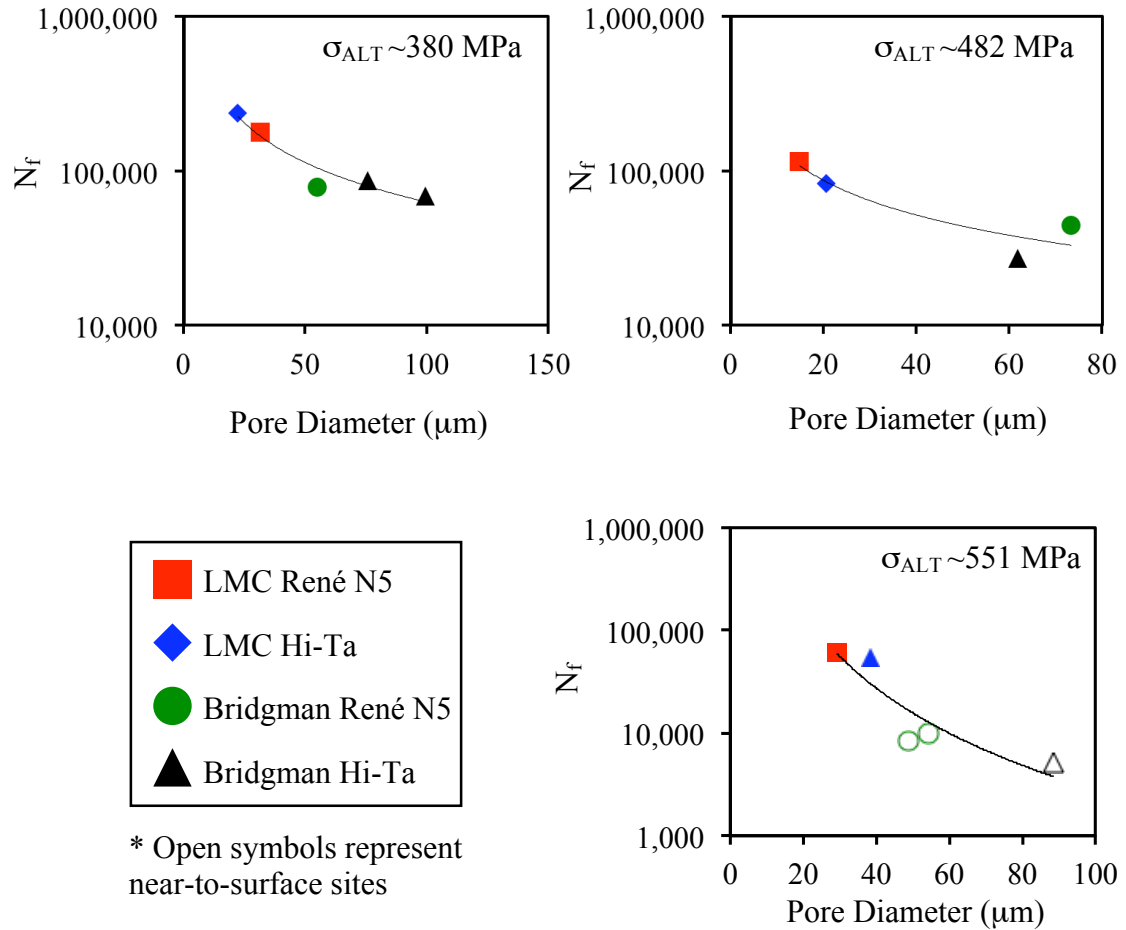
Figure 5.9 Effect of pore diameter on the fatigue life of N5 and Hi-Ta alloys solidified with the LMC and Bridgman process. Specimens were tested at various stress levels at 538°C, *R*= 0 as indicated in the plots. Open symbols represent near-to-surface initiations.

It is expected that the crack initiation process exhibited in these alloys is controlled by cyclic plastic deformation. Even though the samples contained a large range of pore sizes (Figure 4.14) cracks should initiate at locations where cyclic plastic deformation is localized.

Figure 5.10 displays the slip offsets observed near a fatigue crack initiating pore surface of a René N5 specimen solidified with the Bridgman process. This is evidence of the irreversible deformation processes that occurred in the bulk and resulted in un-reversed slip offsets at the pore surface. For a given alternating stress, a critical number of cycles, N_{crit}, will be necessary to develop a critical surface topography at which cracks initiate.[6] The critical number of cycles will be longer, the smaller the alternating stress.
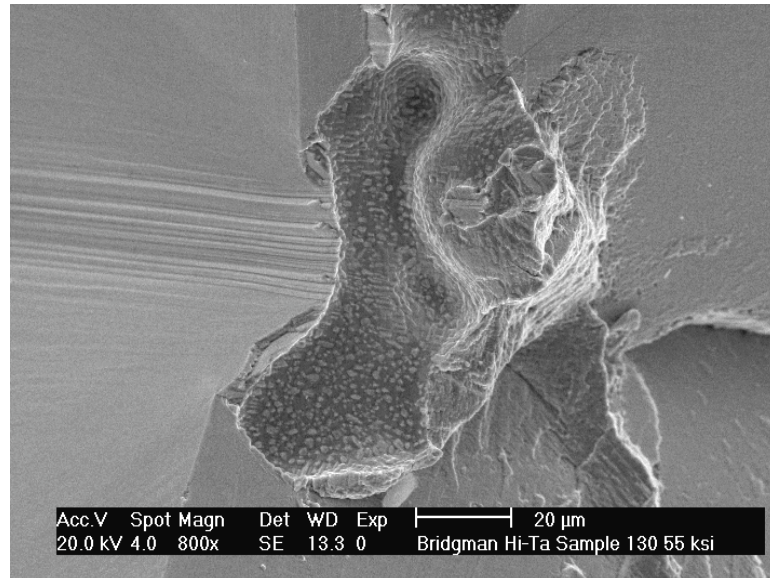
Figure 5.10 Slip offsets near an irregular shaped pore within a Bridgman solidified sample cycled at 380 MPa, (N_f = 86,216)

5.2   Pore Population and Fatigue

The maximum defect size within the material was predicted for a René N5 alloy in Chapter 4 based on statistics of extreme value analysis, with the procedure described by Murakami and co-workers.[7-10] This section will compare the actual site sizes observed from fractography to predicted sizes from each material variant using SEV analysis of pores measured from as-cast metallographic sections.

Pore data was acquired from metallographic sections with an inspection area of S_0 = 2.79 × 10^{-1} mm^2. Figure 5.11 demonstrates that the casting pores follow a lognormal distribution, allowing the largest pore to be estimated for a predicted volume, V.[11] The y-oridinate is presented in terms of the the $-\ln(-\ln(F(x)))$, where $F(x)$, the cumulative probability function (CDF) given as

$$F(x) = \frac{j \times 100}{n+1}(\%)$$

[5.4]

with $j = 1 \ldots n$. The sampled pores are indexed by j to n starting with the smallest defect area:

$$y_i = -\ln\left[-\ln\left(\frac{j}{n+1}\right)\right]$$ [5.5]
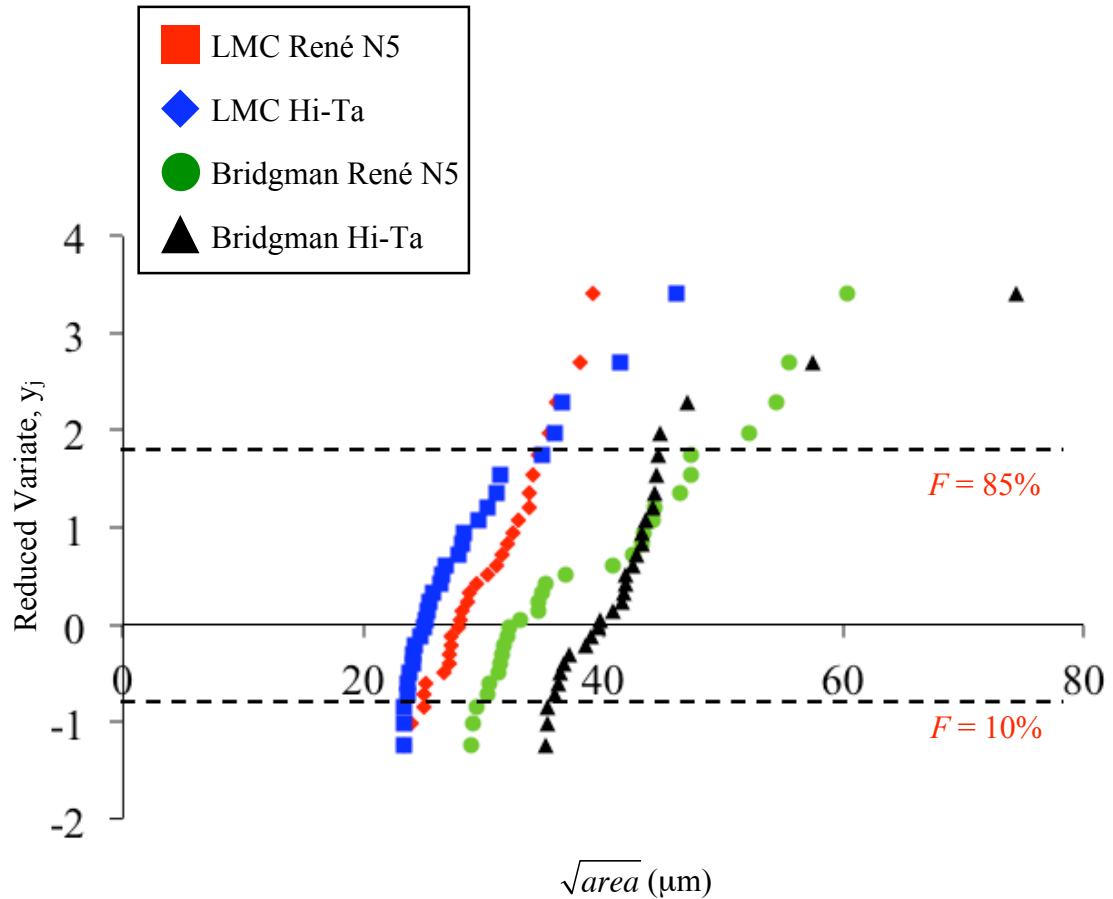
Figure 5.11 Extreme distribution of pore sizes measured from inspection area, $S_0 = 2.79 \times 10^{-1}$ mm^2.

When comparing the distributions for each variant, LMC solidified specimens should contain smaller pore sizes than those solidified with Bridgman casting. Data residing outside of the dashed lines in the figure are outside of the confidence bounds for the lognormal distribution, according to the requirements of Gumbel plots.[9] In order to predict the value of $\sqrt{area}_{max}$ of casting pores contained in a volume, the inspection domain should be in 3-D rather than 2-D. A proposed method shown by Murakami and Toriyama[11] generates a volume by giving a certain thickness to a 2-D area. The standard inspection volume is then describes as $V_0 = h \times S_0$, where h is the thickness. The data in Figure 5.11 enables one to predict the maximum casting defect size in a fatigue

specimen gage section using an h of 1.9 cm. The return period, T, can be calculated for gage volume equal to 389 mm^3 for a fatigue specimen, where

$$T = \frac{V + V_0}{V_0}$$ [5.6]

The predicted defect sizes are shown in Figure 5.12. For comparison, fatigue crack initiating pore sizes are shown in the plot. Instead of treating crack initiation sites as one equivalent circular diameter, adjacent pores were measured separately. The disparity observed between the predicted and actual initiation site size within the Bridgman solidified alloys is likely due to the large mutually interconnected cluster of pores that initiated cracks during fatigue (Figure 5.5c), yet were separately measured with metallography.
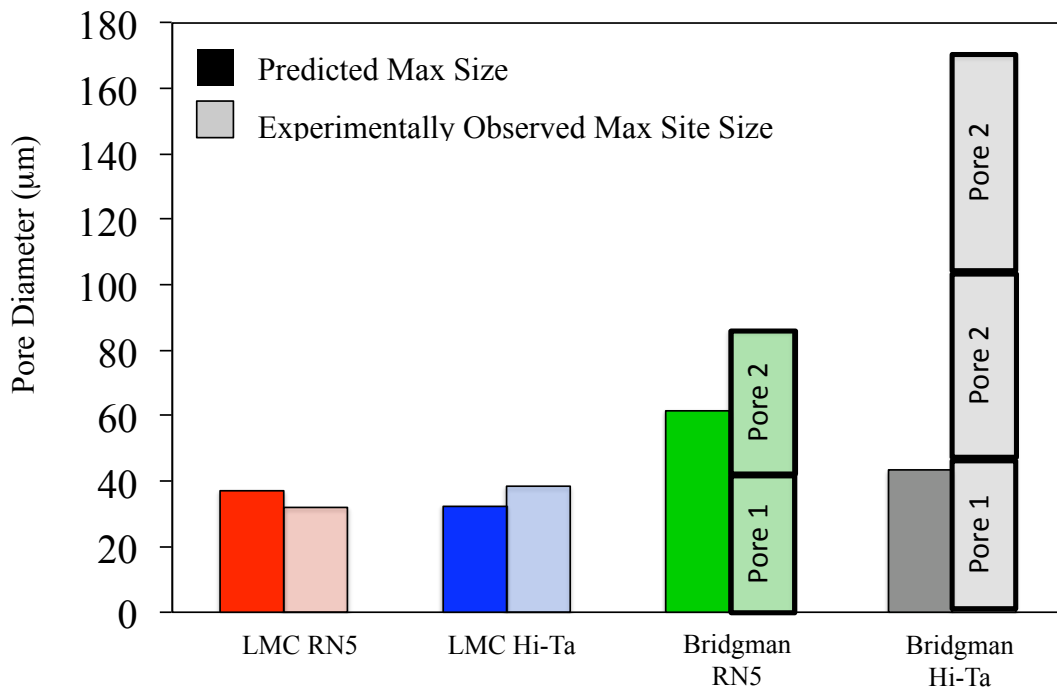
Figure 5.12 Predicted fatigue initiation site diameters using a statistics of extremes methodology.

For the stress ranges investigated, approximately 28% of the samples contained a crack that initiated from an interconnected pore within the Bridgman N5 solidified material. Alternatively, 83% of the Hi-Ta alloy samples solidified with the Bridgman

process initiated cracks from interconnected pores, with a typical example shown in Figure 5.13. In this example, three connected pores were responsible for the fatigue initiation site, in which the average diameter equated to 56 μm. Figure 5.14 shows a projected view of two large pores with an edge distance of approximately 6 μm that initiated a fatigue crack on separate facets $(\sigma_{ALT} \sim 480$ MPa) in a Bridgman René N5 specimen. Slip offsets can be observed, emanating from the pore surfaces. This is an important feature since it indicates a region of strain amplification. It is likely that this small spacing induced severe pore interactions, resulting in plastic shear strain intensification. Unfortunately, the applied method for the determination of extreme values of casting defects does not account for pore clustering, which increases the difficulty in predicting the maximum fatigue initiation site size. This discrepancy will be taken into account when developing a micromechanical model in Chapter 7.
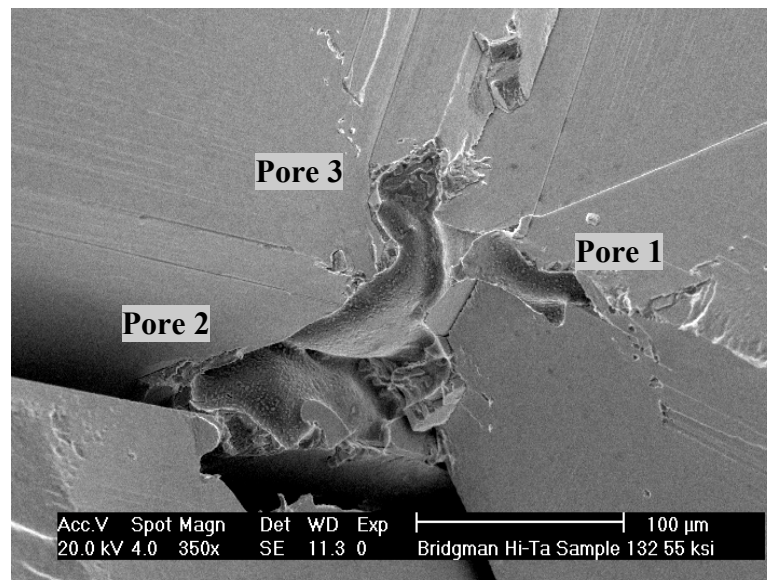
Figure 5.13 Micrograph of a fatigue initiation site consisting of three mutually interconnected pores within a Bridgman solidified Hi-Ta alloy (σ_{ALT} = 380 MPa 68,500 cycles).

120
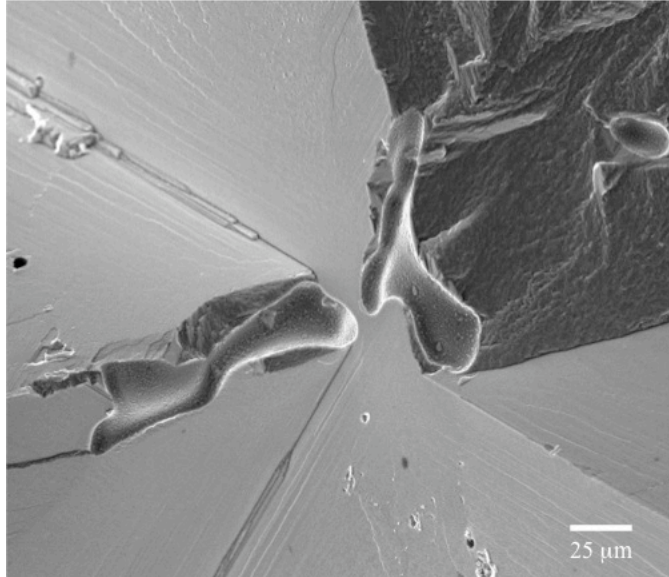
Figure 5.14 Fatigue initiating pores with an approximate 6 μm edge to edge distance within a Bridgman N5 solidified specimen. Sample tested at σ_{ALT} = 482 MPa, N_f = 44,180 cycles.

Given that 83% of the Hi-Ta alloys solidified with the Bridgman process initiated cracks from mutually interconnected pores, a high amount of plastic strain intensification occurred within the samples tested, lowering the fatigue lives. It is clear that adjusting the processing conditions to prevent formation of interconnected pores, which is due to the dendritic structure and tortuous fluid flow path, is necessary. Therefore, goals for casting single crystals should include: (1) minimizing the pore area, (2) avoiding nucleation of larger pores near the surface, and (3) minimize or eliminate pore clusters.

5.2.1 Effect of Pore Clustering on Local Plastic Strain

Predicting the local cyclic plasticity effects at surface or internal regions of a single crystal component during fatigue is of importance in avoiding failure. Couper *et al.*[12] have detailed the effects of localized cyclic plastic shear strain in the interdendritic region of Al alloys under fatigue loading. Experimental results and theoretical analysis by Ting and Lawrence have shown that there exists an intensification of cyclic plastic strain between pores and the free surface.[13] The intense plastic strain concentration/slip between pores and the free surface was considered by finite element analysis (FEA) by Fan *et al.*,[14] with an example illustrated in Figure 5.15. In this example, the contours represent the maximum plastic shear strain for an applied strain amplitude of ε_a = 0.2%

(R = -1), for a slip band approximately 45° to the free surface. The authors have identified locations of maximum plastic shear strain values occurring near the tips of the ellipses, representative of pores, which are nearest to the free surface. Fan *et al.* detailed that when the pore size increased from 55 to 168 μm, the maximum effective plastic strain increased from 1260 με to 21,500 με.[14] The intensification of strain near the free surface for the ellipse shown in Figure 5.15 is a factor of 13X. It is assumed that a similar amplification of plastic strain existed near the pore sites during the LCF process investigated here.
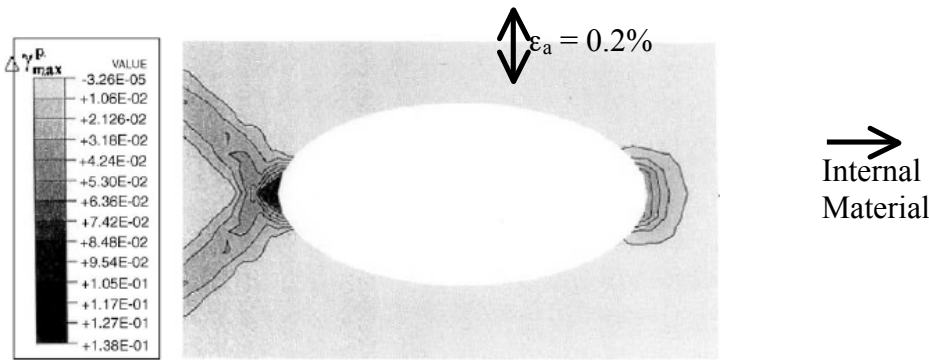
Figure 5.15 FEA results of contours of the maximum plastic shear strain range in the vicinity of a casting pore near the free surface (left) of a A356-T6 Al alloy (R = -1, d_{max} = 40 μm, ε_a = 0.2%.[14]

Hence, the pores—which reside as the largest stress concentrators within the single crystal material—are critical factors to the fatigue life of the investigated alloys. It is clear that the large pores produced with the slower withdrawal rate are especially potent in degrading the fatigue resistance. Since the stress state near pores is critical to the fatigue life, it is highly desirable to predict the maximum pore size within the as-cast microstructure and to develop a protocol for characterization that permits fatigue life prediction.

To investigate the relative effects of size, spacing, local curvature, and clustering of pores on fatigue crack initiation, an idealized pore cluster with four pores arranged in the pattern of Figure 5.16 was analyzed for plastic microstrain development.[14] In order to simulate the pore interactions, symmetry boundary conditions were used, which allowed the four pores to be considered as a periodic array along both longitudinal and transverse directions. Realistic microstructures, where randomly distributed pores were present, were modeled as well. The definitions for B and L as the longitudinal and

transverse spacing direction, respectively, are shown in the figure. The contours in Figure 5.17 represent the microplastic strain concentration that developed near the pore tips in a realistic microstructure, in terms of effective plastic strain. Using the analyses, it was determined that fatigue life was mainly controlled by the largest pores.
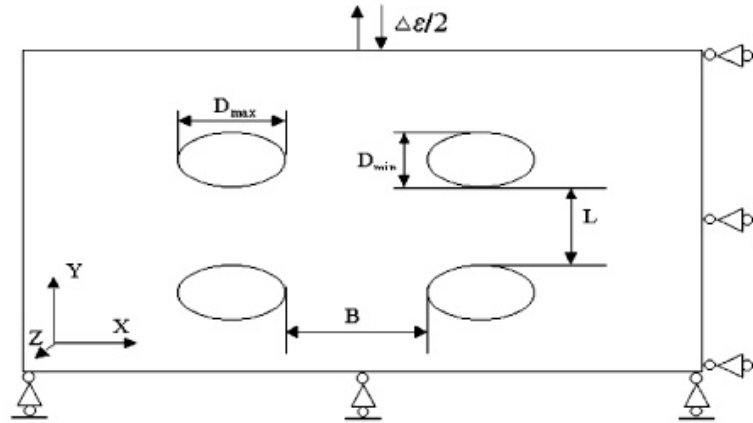
Figure 5.16 Definitions of the notations used for the numerical analyses of the interaction effects between pores.[14]
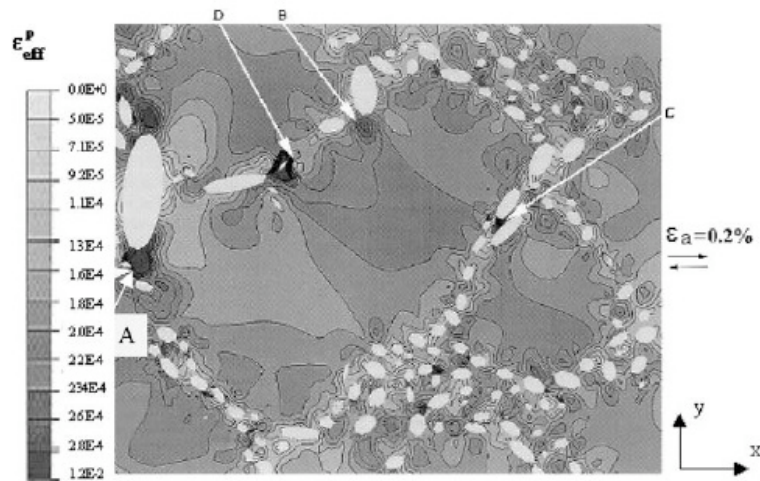
Figure 5.17 Distribution of effective plastic strain within a realistic cast A356-T6 Al alloy microstructure subjected to fatigue at $R = -1$, $\varepsilon_a = 0.2\%$. "D" points to a microcrack site between particles (site C) and "A" and "B" represent microplastic strain near particle tips.[14]

Distributions of the maximum principal stress and maximum plastic shear strain in the pore cluster were obtained in order to observe the effects of pore spacing on the crack incubation life. Here the crack incubation life, N_{inc}, is equivalent to the crack initiation life used in the current study. It can be observed in Figure 5.18 and 5.19, that

the largest pores produced larger $\Delta\gamma^{p*}_{max}$, a shorter initiation life, and a local maximum of $\Delta\gamma^{p*}_{max}$ at a size, d ($= D$) of approximately 180 μm.
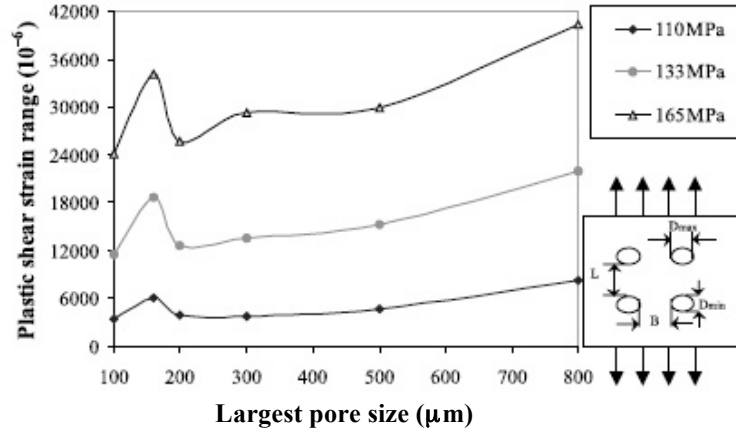
Figure 5.18 Influence of pore size on the maximum plastic shear strain range applied to a cluster of four pores for various applied stress amplitudes at $R = -1$, $D_{max}/D_{min} = 2$, $B = L = 720$ μm.[14]
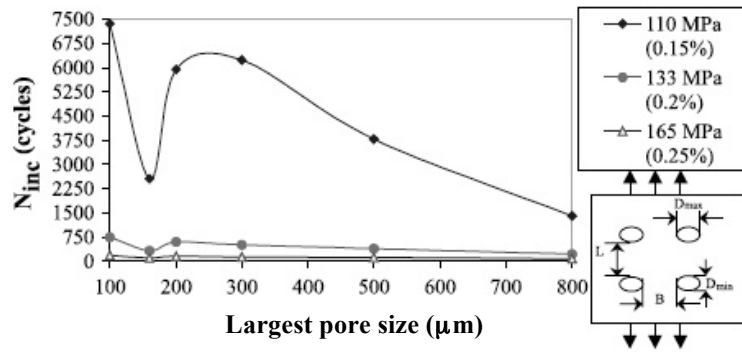
Figure 5.19 Effect of pore size on the crack initiation life for a contrived cluster of four pores at various stress amplitudes ($R = -1$, $D_{max}/D_{min} = 2$, $B = L = 720$ μm).[14]

5.2.2 Evaluation of the Crack Initiation Process

The analysis of the fracture surfaces of the Bridgman solidified material exemplified the transition of internal to surface pore initiations with increasing stress level, producing shorter lives. It should be noted that surface sites are more detrimental due to the higher stresses near the surface and lower degree of constraint of the near-surface volumes of cyclically loaded material.[15]   Lukáš[16] has noted this effect from analyzing second-phase particles at the free surface and interior regions. For example, the stress concentrating effect of a spherical particle at the surface (modeled by a

124

hemispherical pit) was about 7% higher than that of the sample spherical particle in the interior (modeled by a spherical cavity).[16]

From the statistical analysis using Voronoi Tessellations exhibited in Chapter 4, it was demonstrated that pores are scattered throughout the microstructure within the interdendritic area. Therefore, it can be assumed that pores large enough to generate fatigue cracks likely resided at both surface and interior regions of the gage section. Hence, the likelihood of a pore initiating at the surface is determined solely by the availability of a pore at the surface. With the reduction in pore size using LMC casting, higher stress levels can be applied, since more cycles are needed to accumulate plastic strain from internal initiations.

5.3   Fatigue Life Prediction

It is still a question of debate as to whether crack initiation process begins very early in the fatigue cycle or towards the end of life.[17,18] Remy and Fleury[19] have suggested that the total life of a single crystal component encompasses a significant proportion of time initiating cracks, followed by microcrack growth. This is likely the process exhibited in the alloys tested in this study, with the initial flaw size representative of a pore size, a_0. Although it is difficult to define crack initiation precisely, a crack is assumed to be initiated once a certain criterion has been met, such as a critical crack length, local plastic strain or strain energy density.[20,21] A few studies have specifically defined crack initiation as possessing 200-300 μm of crack depth,[22,23] which would be much larger than the pore diameters exhibited in Table 5.3. Therefore, the crack initiation process in these single crystals, especially solidified with LMC, requires further investigation to predict the fatigue life.

It has been shown the fatigue life decreases with increasing pore area for a given stress level. Therefore, it is of particular interest to investigate whether the fatigue crack growth stage dominates for a given pore size. Typically for single crystals, the crack initiation life has been considered negligible and the total fatigue life has been estimated by integrating the Paris-Erdogen law or by using a small-crack based growth law from the initiation pore size to the final crack size determined by the material's fracture

toughness.[24] Using a damage tolerance approach, the application of fracture mechanics can be assessed through Equation 5.7 of the form,[24]

$$\frac{da}{dN} = C(\Delta K)^m$$
[5.7]

where da/dN is the rate of crack propagation, C and m are constants of 10^{-11} MPa$^{-3.6}$-m$^{-1.81}$ and 3.6, respectively, for single crystal René N5.[25] The ΔK $(=Y\Delta\sigma(\pi a)^{0.5})$ is the stress intensity factor, a_o is the initial flaw size taken as the fatigue crack initiating pore radius, and a_f is the final crack length. Integration of this equation provides the residual lives of specimens through the following equation:

$$N_f = \frac{1}{C\Delta\sigma^m Y^m \pi^{m/2}} \left[\frac{2a_0^{1-m/2} - 2a_f^{1-m/2}}{m-2} \right]$$
[5.8]

where m ≠ 2. Table 5.4 displays the predicted lives based on the crack growth equation, and are shorter than the experimentally measured fatigue lives. This suggests that initiation does not occur immediately during cycling and the crack initiation life dominates the total life.

Table 5.4 Lifetime data for selected LCF (538°C, R=0) specimens compared to model predictions using the Paris-Erdogan relation.

Material	σ_{ALT} (MPa)	a_o (μm)	Predicted	Actual Life
Bridgman N5	551	27.1	1,489	9,763
Bridgman Hi-Ta	570	44.2	715	5,135
Bridgman N5	551	19.4	1,750	8,499
Bridgman N5	448	25.2	1,488	21,410
Bridgman Hi-Ta	448	36.6	836	19,497
LMC N5	546	14.6	2,489	60,724
LMC N5	419	12.8	3,358	204,131

Since LCF lives at 538°C ($R = 0$), were pore size driven, stress intensities at initiation sites are considered. Based on the defect sizes, the initial stress intensity factor, K_I, was calculated using the following formulae:[26]

$$K_I = 0.65\sigma\sqrt{\pi\sqrt{A_{defect}}}$$
[5.9]

126

for surface crack initiation, and

$$K_I = 0.5\sigma \sqrt{\pi \sqrt{A_{defect}}}$$ [5.10]

for internal crack initiation, where σ is the stress range applied and A_{defect} is the area of the pore measured from a projection on a plane perpendicular to the stress axis. Examples of surface and internal pores are shown in Figure 5.20. Modification of these equations to reflect an initial Mode II stress intensity factor, K_{II}, is is shown as

$$K_{II} = Y\tau \sqrt{\pi \sqrt{A_{defect}}}$$ [5.11]

where Y equals 0.5 or 0.65 for internal or near-to-surface initiations, respectively, and τ is the shear stress range.

(a)   (b)
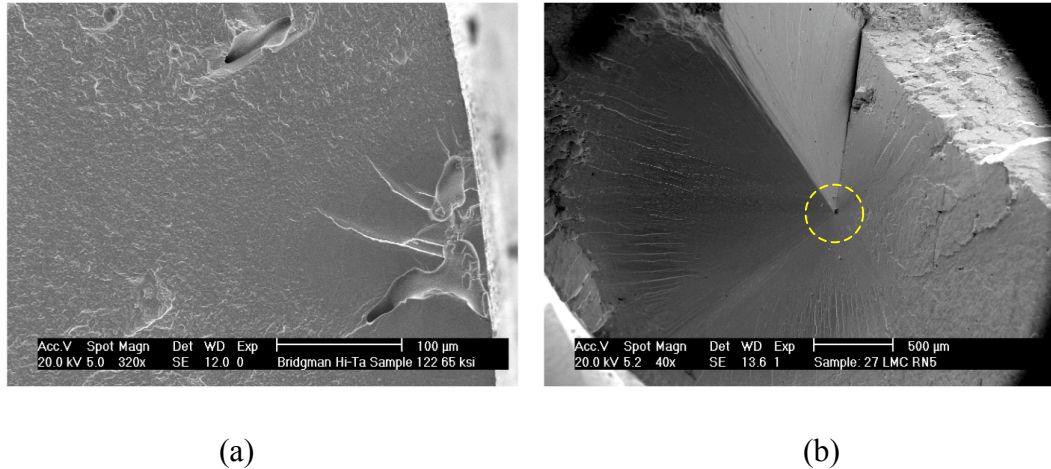
Figure 5.20 Examples of (a) surface and (b) internal crack initiating pores within a single crystal specimen tested at 538°C. High magnification fractograph of internal pore shown in Figure 5.4b.

Fatigue lives depend primarily on the defect size and location (near-to-surface vs internal). Pore shape, on the other hand, appears to exert much less influence on fatigue life.[27] Studies have indicated that the size of the defects, rather than the shape, is important to crack initiation,[28-30] and therefore this aspect of structure was not taken into account in subsequent analysis.

For the purpose of initially developing a simple model describing the role of defect size on fatigue life, the initial stress intensities associated with small cracks

emanating from pores were determined for pore sizes observed on post-fatigued specimens. Figure 5.21 displays the relationship between stress intensity using Equations 5.9-5.11 and the number of cycles to failure. For the four alloy/process variants analyzed, the lives decreased with an increase in initial stress intensity.
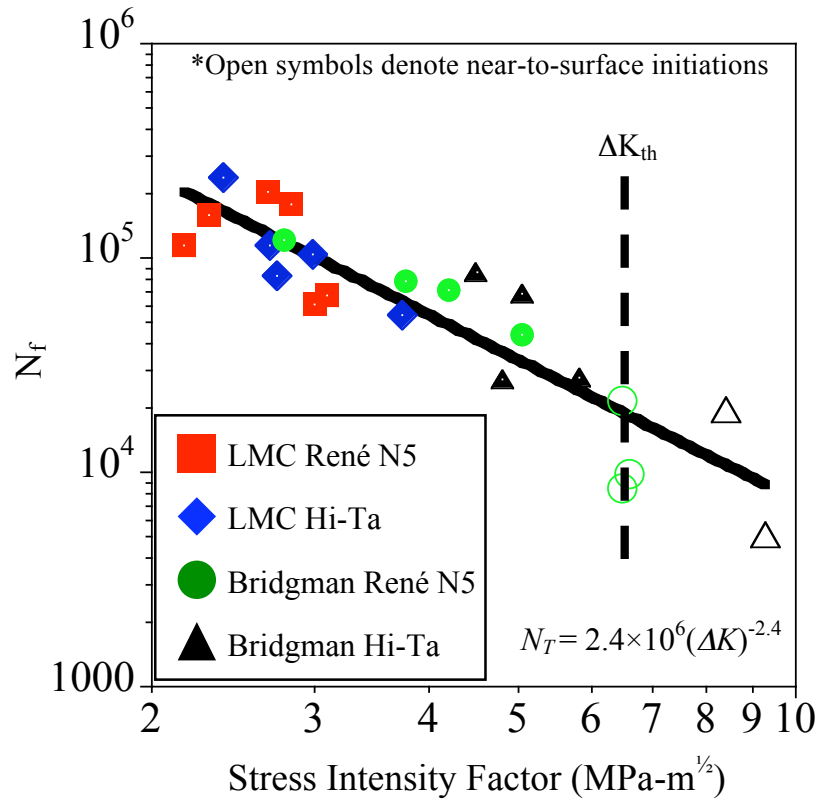
Figure 5.21 Stress intensities plotted for LMC and Bridgman solidified René N5 and modified René N5 alloys from LCF testing at 538°C.

Smaller stress intensities were associated with the pores with the LMC refined microstructure. In the LMC-processed materials, the stress intensities were far below the ΔK_{th} of René N5,[31] represented by a dashed line in the figure. Yet, crack growth still occurred, leading to failure. Open symbols represent near-to-surface initiations from pores. It should be noted that these initiations produced shorter lives in comparison to internal fractures. Interestingly, near-to-surface initiations occurred at intensity values near or greater than the threshold. The data presented in Figure 5.21 can be represented by the following power-law relationship:

$$N_T = 2.4 \times 10^6 \left(\Delta K \right)^{-2.4}$$ [5.12]

The stress intensity takes into account pore location (surface or internal) and either Mode I or mixed-mode stress intensity. The implications of this relationship will be addressed in Chapter 7, which presents a microstructure–based fatigue modeling approach for single crystal material. Additionally, a crack initiation model is necessary to combine to the crack growth law in order to estimate the fatigue lives for a range of pore sizes. With the substantial effect of refinement on the initiating pore size, it is also of interest to examine the influence of refinement on the crack growth behavior. Chapter 6 presents crack growth studies on coarse and finer-scaled microstructures to address this issue.

5.4   Summary

Up to a 7X increase in strain-controlled low cycle fatigue life (538°C, $R = 0$) was produced in the single crystals solidified with the LMC process, in comparison to Bridgman processed samples. The increase in fatigue life using LMC casting was attributed to the 65 pct reduction in maximum pore size using a solidification rate of 12.7 mm/min.

Smaller casting pores, either near the specimen surface or in the interior, were found to be responsible for crack initiation in all tested specimens. Cycling at alternating stresses between 380-551 MPa led to the formation of intense slip bands near pore surfaces and represented sites for the crack initiation. Initiating pores were found to be smaller in the LMC solidified alloys in comparison to the samples cast with the Bridgman process. The initiation site diameters followed a lognormal distribution, which allowed for statistics of extreme value analysis (SEV) comparisons to the predicted sizes determined in Chapter 4. An increased amount of Ta produced larger casting pore diameters and larger fatigue initiation sites sizes. Due to interconnected pores created during solidification, a high probability of initiating a crack from adjacent pores was found in the Bridgman Hi-Ta material, yielding underpredictions of site diameters using SEV analysis. However, similar lives were observed for the René N5 and modified alloys due to the increase in yield strength from Ta addition.

129

Significant underestimation of the fatigue life using the crack growth law requires the implementation of a crack initiation based model, especially for internal initiations. Internal sites are preferred over near-to-surface crack initiation since it requires more cycles to initiate cracks. Two distinct crack initiation behaviors were exhibited: (1) highly faceted initiation along {111} crystallographic planes at lower stress levels, and (2) Mode I opening behavior from near-to-surface pores at higher stress levels. The influence of these two crack growth modes on the fatigue life will be addressed in Chapter 6.

[1]   A. Sengupta, S.K. Putatunda, L. Bartosiewicz, J. Hangas, P.J. Nailos, M. Peputapeck, and F.E. Alberts: *J. of Mater. Eng. Perfomance*, 1994, 3, pp. 664-672.

[2]   Y. Murakami: *Metal Fatigue: Effects of Small Defects and Nonmetallic Inclusions,* Elsevier Science, 2002.

[3]   P.J.E. Forsyth: *A Two-Stage Process of Fatigue Crack Growth, Pro. Crack Propagation Symp,* The College of Aeronautics, Cranfield, 1961, pp. 76-94.

[4]   G.R. Leverant and M. Gell: *Metall. Trans. A*, 1975, 6, pp. 367-71.

[5]   D.H. Chen and Z.Y. Wen: *Aeronautics Mater.*, 1983, 5, pp. 1-5.

[6]   H. Mughrabi: Fat. Fract. Engng. Mater. Struct., 2002, 25, pp. 755-764.

[7]   Y. Murakami and M. Endo: *Int. J. of Fat.*, 1994, 16, pp. 163.

[8]   B. Epstein: *Technometrics*, 1960, 2, pp. 27

[9]   E.J. Gumbel: *Statistics of Extremes*, Columbia University Press, 1958.

[10]   P.G. Forrest: *Fatigue of Metals*, Oxford, Pergamon Press, 1962.

[11]   Y. Murakami, T. Toriyama, and E.M. Coudert: *J. Testing and Evaluation*, 1994, 22, pp. 318-326.

[12]   M.J. Couper, A.E. Neeson, and J.R. Griffith: *Fat. Fract. Mater. Struct.*, 1990, 13, pp. 213-.27.

[13]   J.C. Ting and F.V. Lawrence: *Fat. Fract. Engng. Mat. Struct.*, 1993, 16, pp. 631-47.

[14]   J. Fan, D.L. McDowell, M.F. Horstemeyer, and K.A. Gall: *Engng. Fract. Mech.*, 2003, 70, pp. 1281-1302.

[15]   G.T. Cashman: *J. Eng. Tech*., 2007, 129, pp. 293-303.

[16]   P. Lukáš and L. Kunz: *Mater. Sci. Eng. A*, 2001, A314, pp. 75-80.

[17]   T.P. Gabb, J. Gayda, and R.V. Miner: *Metall. Mater. Trans. A*, 1986, 17, pp. 497-505.

[18]   A. Hyunna, V.T. Kuokkala, J. Laurila, and P. Kettunen: *J. Mat. Engng. Performance*., 1993, 2, pp. 531-536.

[19]   E. Fleury and L. Rémy: *Mater. Sci. Eng. A*, 1993, 167, pp. 22-30.

[20]   K. Tanaka and T.T. Mura: *J. of Appl. Mech.*, 1981, 48, pp. 97-103.

[21]   K. Shiozawa, Y. Tohda, and S.M. Sun: *Fat. Frac. Eng. Mater. Struct.*, 1997, 20, pp. 237-247.

[22]   J. Reuchet and L. Rémy: *Mater. Sci. Eng.*, 1983, 58, pp. 19-42.

[23]   M. Reger and L. Remy, *Mater. Sci. Eng. A*, 1988, 101, pp. 47-63.

[24]   P.C. Paris and F. Erdogan: *J. of Basic Engr.,* 1963, 85, pp. 528-534.

[25]   C. Yablinsky: *PhD Thesis*, The Ohio State University, Columbus, OH, 2010.

[26]   Y. Murakami: *Metal Fatigue: Effects of Small Defects and Nonmetallic Inclusions,* Elsevier Science, 2002.

[27]   J.-Y. Buffière, S. Savelli, P.H. Jounweau, E. Maire, and R. Fougères: *Mater. Sci. Eng. A,* 2001, A316, pp. 115-126.

[28]   Y.X. Gao, J.Z. Yi, P.D. Lee, and T.C. Lindley: *Fat. Fract. Eng. Mater. Struct*., 2004, 27, pp. 559–70.

[29]   Y. Murakami and M. Endo: *Int. J. Fatigue*, 1994, 16, pp. 163–82.

[30]   K. Gall, M.F. Horstemeyer, B.W. Degner, D.L. McDowell, and J. Fan: *Int. J. Fract*., 2001, 108, pp. 207–33.

[31]   C. Yablinsky: *PhD Thesis*, The Ohio State University, Columbus, OH, 2010

Chapter 6

IN-SITU OBSERVATIONS OF FATIGUE CRACK GROWTH

Chapter 6 describes the _in-situ_ fatigue experiments conducted on LMC and Bridgman solidified René N5 alloys that were conducted to examine the influence of microstructure on crack growth behavior. A novel X-ray synchrotron radiation approach was employed to acquire unique observations of fatigue cracking within the dendritic microstructure at temperatures ranging from 23°C to 720°C. Two microstructure scales were investigated, for samples containing an average SDAS of 25 and 65 μm, solidified with LMC ($V = 12.7$ mm/min) and Bridgman ($V = 3.4$ mm/min) processes, respectively.

This chapter first describes the _in-situ_ loading/imaging system to observe real-time fatigue crack growth under positive mean stresses and at high frequency ($f = 20$ kHz) cycling. This unique fatigue apparatus (detailed in Chapter 2) was installed at the Advanced Photon Source (APS), a 3rd generation synchrotron facility located at Argonne National Laboratory. The tests conducted and the _in-situ_ observations are described in the remainder of the chapter.

Characterization of the crack growth behavior at various microstructure scales will provide an integral component for a fatigue property model and provide insight for the usefulness of utilizing innovative solidification processes to refine the dendritic structure. The influence of microstructure scale on crack growth mode will be discussed, and the implications for modeling the fatigue behavior of single crystal superalloys will be presented in Chapter 7.

6.1   High Brilliance X-Ray Radiation Imaging

The experimental setup of the portable ultrasonic fatigue apparatus at the APS synchrotron facility was described in detail in Chapter 2. Microspecimens tested in this apparatus were fabricated by electrodischarge machining blanks from a heat-treated single crystal cylindrical bar. The thin-sheets were then metallographically prepared with hand grinding and polishing steps to a desired thickness between 170 and 200 μm. The tensile axis was in the [001] direction and the width was parallel to the [010] direction. An edge notch was produced in the center of the gage section using a femtosecond laser as described in Chapter 2.

Figure 6.1 shows the 2 mm circular imaged area of the laser notched fatigue specimen mounted in the portable fatigue instrument during imaging with synchrotron X-radiation prior to fatigue testing. Owing to the coherence of the beam, carbide and pore boundaries produced constructive and destructive interference fringes characteristic of phase contrast imaging, due to the abrupt change in electron density. The dendritic structure is clearly delineated due to absorption contrast imaging of differing elemental compositions within the dendritic and interdendritic regions.[1] Optical images revealing the two dendritic microstructures investigated are shown in Figure 6.2 and 6.3 for the LMC and Bridgman solidified castings at 12.7 mm/min and 3.4 mm/min, respectively. As detailed in Chapter 3, these solidified structures were composed of average secondary dendrite arm spacings of 25 μm and 65 μm for the fine and coarse microstructures, respectively. It was assumed that no more than one dendrite core is present in the thickness direction for a given sample.
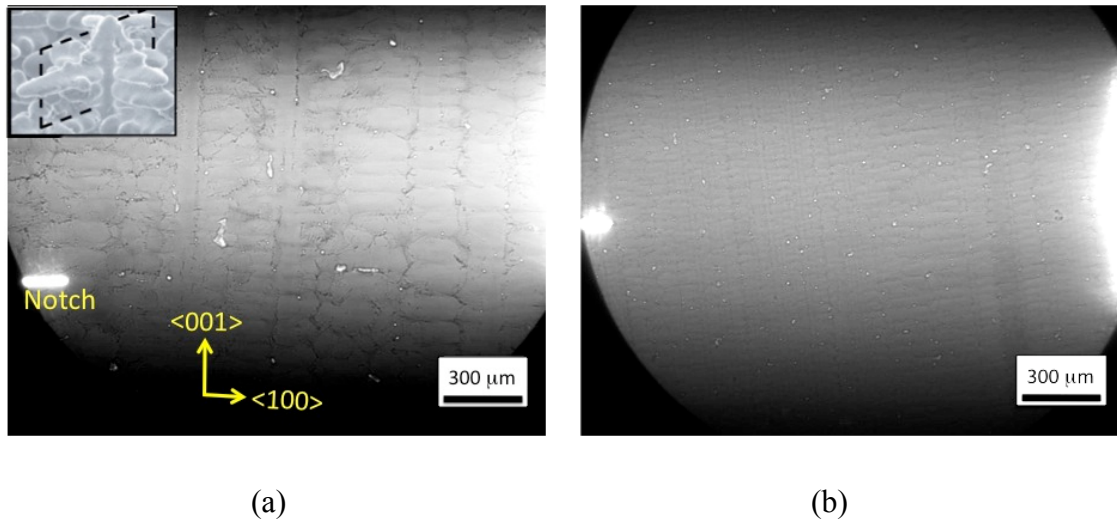
(a) (b)

Figure 6.1 Synchrotron X-ray image of the 2 mm view of thin-sheet René N5 nickel-base superalloy specimens, displaying dendritic and interdendritic features highlighted due to phase and absorption contrast imaging. Samples are from directionally solidified bars sliced parallel to the withdrawal axis with average secondary dendrite arm spacings of (a) 25 µm from a high solidification velocity (12.7 mm/min) and (b) 65 µm of a low solidification velocity (3.4 mm/min).
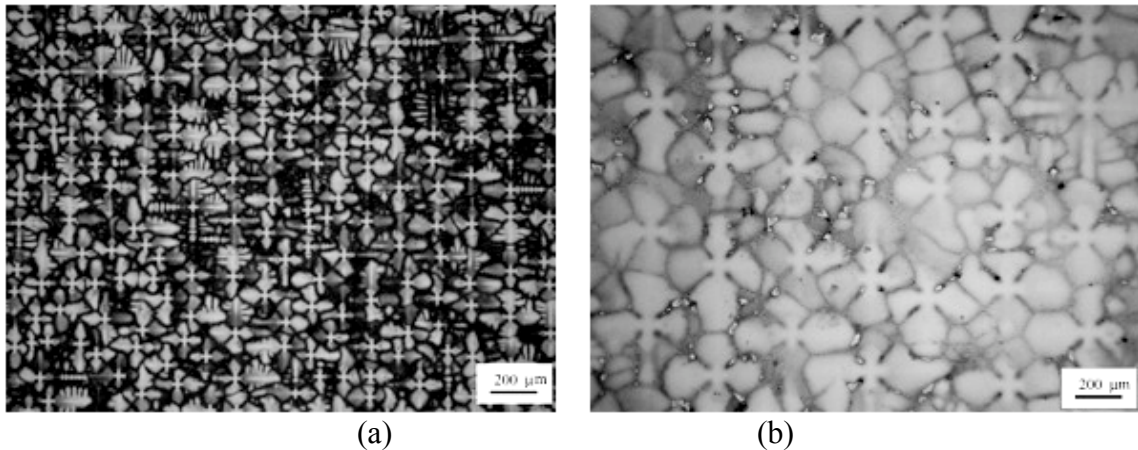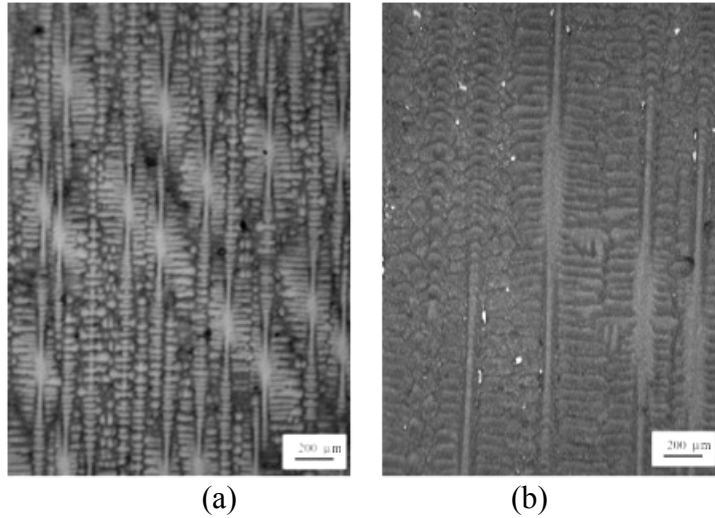

(a) (b)

Figure 6.2 Variation in primary dendrite arm spacing and dendrite morphology with casting withdrawal rate. Optical images viewed normal to the [001] growth direction for average primary dendrite arm spacings of (a) 150 µm and (b) 350 µm for LMC and Bridgman solidified René N5 alloys, respectively.

134

(a)   (b)

Figure 6.3 Variation in secondary dendrite arm spacing and dendrite morphology with casting withdrawal rate. Optical images are viewed parallel to the [001] growth direction for average secondary dendrite arm spacings of (a) 25 μm and (b) 65 μm for a René N5 alloy.

6.2   Thin-Sheet Specimen Design

In order to achieve 20 kHz frequency cycling in resonance for the thin-sheet microspecimens, finite element modeling (FEM) analysis was conducted to ascertain the appropriate geometry based on the density and Young's modulus. Liu *et al.*[2,3] have conducted 3-D static, linear FEM analyses for the carrier and the attached microspecimen in order to characterize the elastic stress distribution produced in the fatigue specimen by the displacement of the pin loading positions of the carrier. The Ti-6Al-4V carrier specimen and attached microspecimen are shown in Figure 6.4. It should be noted that the cyclic stresses were kept low enough to prevent fatigue failure in the Ti-6Al-4V carrier specimen at a typical load, yet large enough to initiate a fatigue crack at the notch tip in the microspecimen. A stress-life approach verified that the carrier could be used for many tests before exhibiting any structural damage.
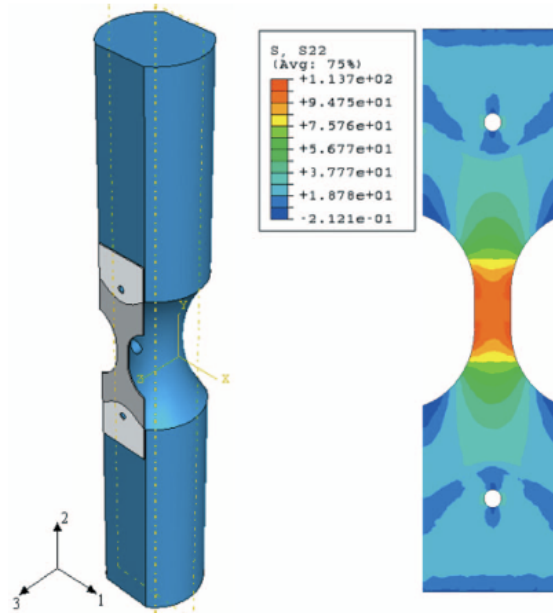
135

Figure 6.4 Details of the finite element analysis results for the stress distribution in the microspecimen during loading. The color key represents the tensile stress σ_{22} in MPa.[3]

(a)　　　　　　　(b)　　　　　　　(c)
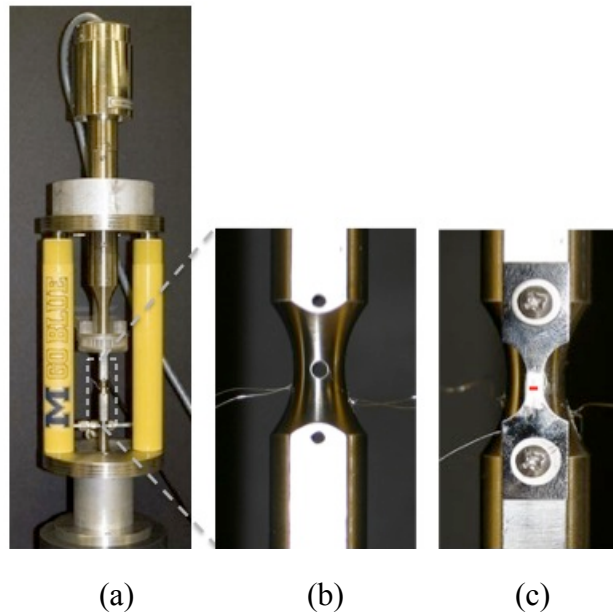
Figure 6.5 Images of the (a) fatigue apparatus, (b) Ti-6Al-4V carrier specimen and (c) single crystal microspecimen rigidly attached to the carrier specimen. The red line on the microspecimen illustrates the location of the edge notch. (Figure presented in Chapter 2)

6.2.1 Stress Distribution on Microspecimens

The stress and strain applied to each component were estimated from the carrier and microspecimen dimensions before fatigue experiments were conducted. The ratio of the loading between the carrier and the microspecimen was identified based on numerical

136

analysis and experimental verification. Since the applied load was controlled by the displacement of the carrier, the load was transferred from the carrier to the fatigue specimen at the shoulder connections, as illustrated in Figure 6.5. Therefore, the loading ratio was dependent on the specimen geometry and the elastic modulus for the carrier and microspecimen.

Based on FEM analysis, the maximum stress occurred in the gage section of the micro-specimen.[2] The ratio between the maximum stress in the microspecimen and in the carrier was determined as 73%. Strain measurements within the gage section validated the stress ratio. Due to the small thickness of the microspecimen, it was assumed that the thin sheets deformed under plane stress conditions, where the stresses acting normal to the sheet plane are negligible in comparison to the in-plane components.

6.3   Data Acquisition

A total of 12 fatigue tests were conducted at a stress ratio of $R = 0.1$ at temperatures between 23°C to 750°C. Table 6.1 displays the list of the specimens and conditions used for high cycle fatigue testing of the samples. The ΔK_{app} value was measured from the stress range applied to initiate a crack from the notch ($Y = 1$) until failure. Inclination angles of the cracks are given with respect of the notch plane. A stress ratio of $R = 0.1$ was chosen to avoid buckling of the specimen. The resonant frequency during cycling was approximately 20 kHz. The 20 kHz pulse and pause durations were 0.1 s and 2.0 seconds, respectively, to minimize any temperature rise from internal friction at high strain rates. A schematic of the pulse and pause segments during cycling is shown in Figure 6.6. Images were collected during each of the block segments as illustrated. Images of 500 μm by 800 μm were corrected with image processing and compiled into real-time movies to allow for *in-situ* crack growth imaging, crack length measurements, and observations of microstructural interactions with propagating cracks. *In-situ* imaging during the high frequency cycling also allowed for monitoring of the cracks and provided the option of pausing the test for rotating and translating the crack planes.
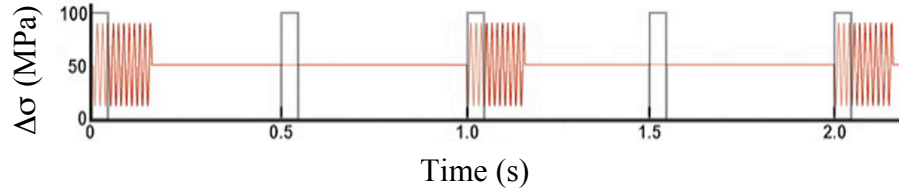
Figure 6.6 Schematic of the pulse and pause segments during high frequency fatigue cycling. X-ray images were acquired using a CCD device during each of the time blocks shown. Figure drawn by Naji Husseini.

Table 6.1 Summary of conditions of microspecimens subjected to high cycle fatigue testing.

Sample #	Temp (^{o}C)	$\Delta\sigma$ (MPa)	ΔK_{app} (MPa-m$^{1/2}$)	Notch Length (μm)	Inclination Angle from Notch (^{o})	Laue, γ (^{o})
LMC-1	23	137	4.6	366	45	4.3
LMC-2	23	132	4.0	356	45	4.3
Bridgman-3	23	102	3.6	262	45	7
LMC-4	538	158	4.6	277	15	5.5
LMC-5	538	144	4.5	320	15 + 30	5.5
Bridgman-6	538	313	11.8	451	0 + 45	7.4
Bridgman-7	538	281	8.6	302	20	7.4
LMC-8	580	83	2.9	397	20 + 0	4.3
LMC-9	580	83	2.7	339	0 + 35 + 20	4.3
LMC-10	720	113	3.2	260	0	5.5
LMC-11	720	75	2.5	324	0	5.5
Bridgman-12	720	424	11.8	367	25	7.4

In order to conduct fatigue tests within the very high cycle regime in a timely manner, a step test procedure was implemented. By controlling the voltage of the system, a low stress was applied to a sample for 10^7 cycles. If the crack did not grow within that cycling period, the mean stress and stress amplitude were both increased by 10% for an additional 10^7 cycles, and henceforth until a crack initiated from the notch root. The strain amplitude was then kept constant until the specimen failed. If the maximum amplitude of the fatigue system was attained before crack initiation occurred during a step test, the sample was cycled for no more than 4 hours before stopping the test. Based on the amplitude required to nucleate a crack from the notch, an initial Mode I stress intensity factor was recorded based on the notch geometry ($Y = 2/\pi$), notch length

and applied stress level. The stress intensity factor required to initiate a crack during the step test was designated as ΔK_{app}.
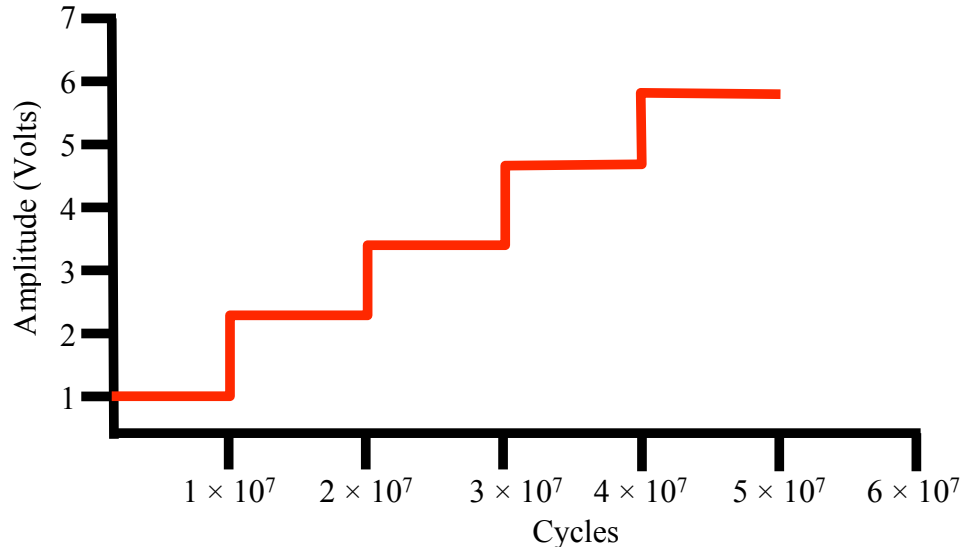
Figure 6.7 Schematic of step-test procedure used for fatigue testing of thin-sheet microspecimens.

6.4   Inclined Cracks

Figure 6.8 displays an X-ray image and an optical image of a fatigue crack within a Bridgman solidified sample tested at ambient temperature. The micrograph shows a crack that extended through the entire thickness of the sample at an inclined angle, which indicated that 3-D information could be captured from a 2-D projection of a crack. River marks, pores and metal carbides were observed in the X-ray image, as detailed in Figure 6.8. The thickness of the microspecimen, ΔK_{app} and cycles endured to grow the crack are displayed in the insert.
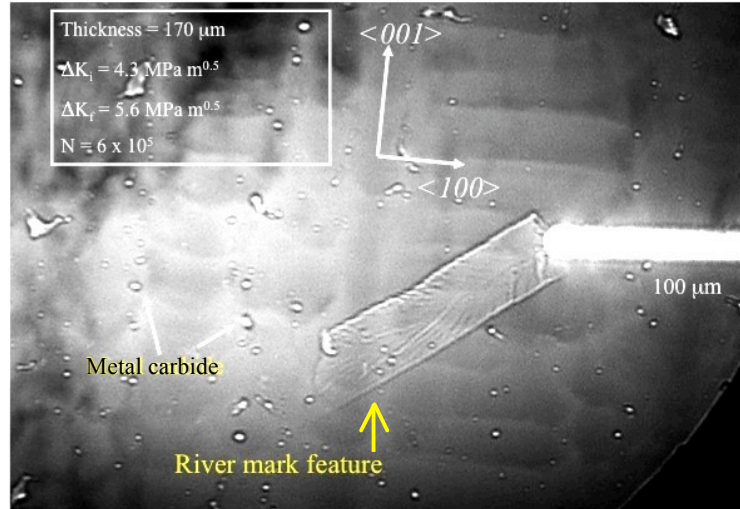
(a)
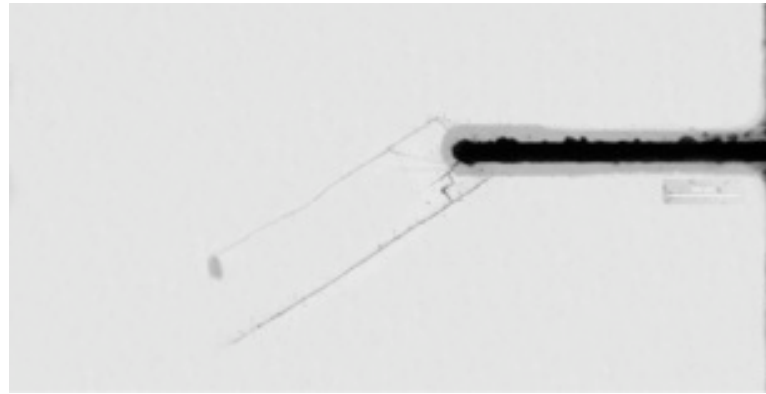
(b)

Figure 6.8 Images of a fatigue crack produced by high cycle fatigue. (a) X-ray image showing the front and back surface of a crack, which has extended through the entire thickness of the sample. (b) Merged optical images of the crack revealing the relative intersections of the crack with the front and back surfaces of the specimen.[2]

A series of X-ray images displaying the growth of a fatigue crack with increasing cycles is shown in Figure 6.9 for a LMC solidified sample ($\lambda_2 = 25$ μm) tested at ambient temperature. Similar to Figure 6.8, the crack emanated from the notch at an inclined angle. A plot for the crack extension with increasing cycles is presented in Figure 6.10. The initial Mode I stress intensity value (K_{app}) was 4.6 MPa-m$^{\frac{1}{2}}$ respectively, which corresponded to the notch depth. The intensities were calculated based on the notch geometry, Y, using Equation 6.1 as

$$K_I = Y \Delta \sigma \sqrt{\pi a} \qquad\qquad [6.1]$$

where $\Delta\sigma$ is the stress amplitude.

(a)   (b)

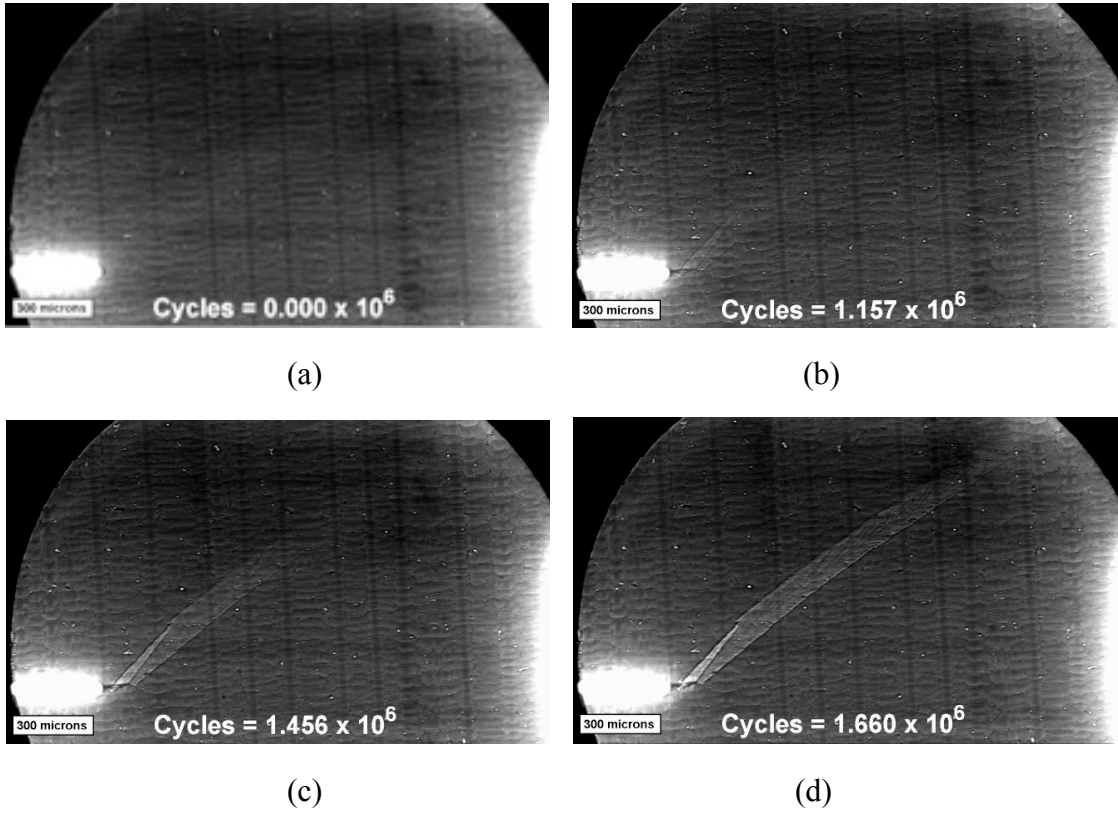(c)   (d)

Figure 6.9 Series of X-ray images demonstrating the growth of an inclined fatigue crack emanating from the laser notch.
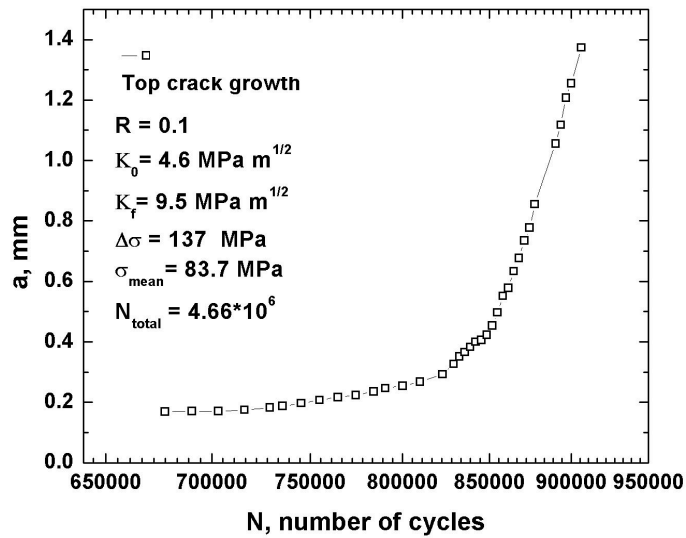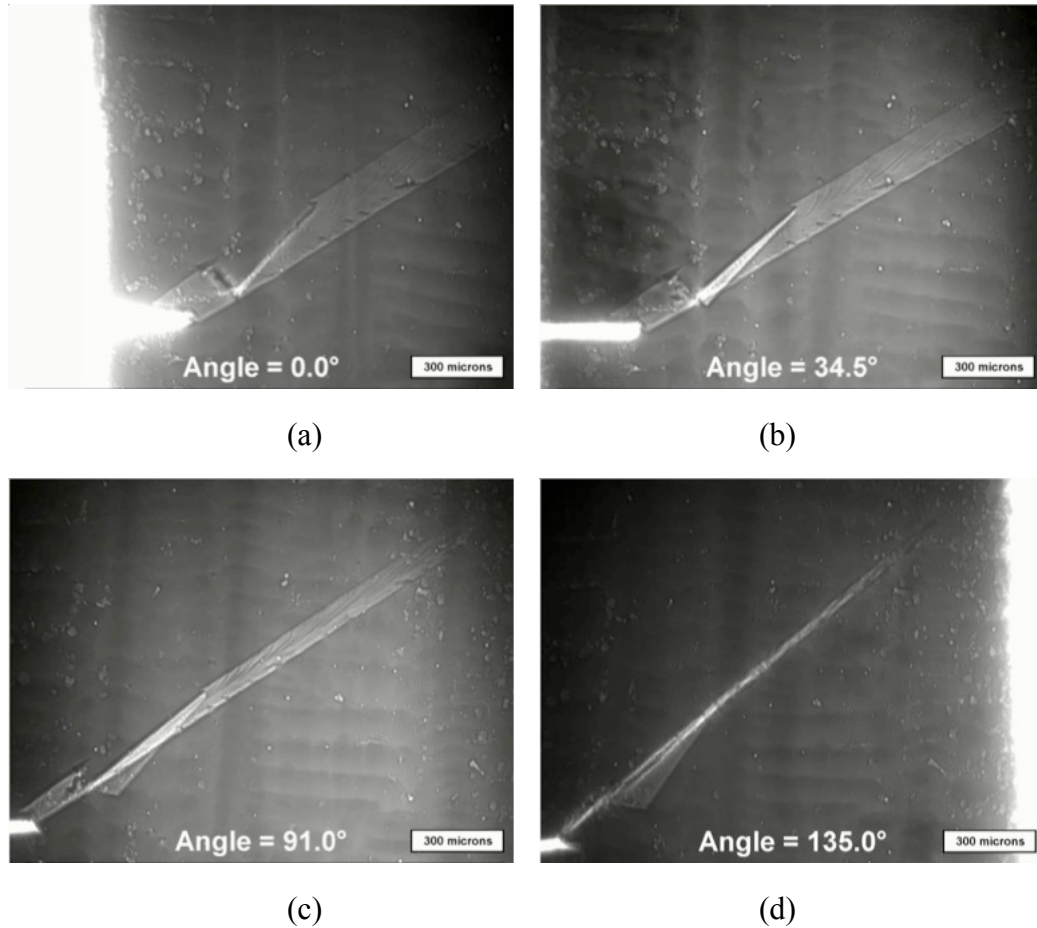

Figure 6.10 Crack extension per cycle for a LMC solidified René N5 sample tested at ambient temperature.

(a)   (b)

(c)   (d)

Figure 6.11 Rotation of a post cracked sample with respect to the incident X-ray beam. Each rotation angle with respect to the beam is indicated in each X-ray image for a-d.

The inclination angle between the fracture surface and the notch surface was calculated for each sample with an example of an angle measurement shown in the SEM image (Figure 6.12). The analytical geometry relation assumes that the notch surface is perpendicular to the <001> direction, the thickness direction of the micro-specimen is in the <100>, and the width direction is in the <010>. From this example, it can be seen that the inclination angle between the notch surface and the crack is 38°. Assuming that the deformation occurred along a single <111> plane in this case, the deviation from 45° is likely due to the misalignment of the dendrite direction ($\gamma = 4.3^o$) with respect to the stress axis. The symbol γ is defined here as Laue angle for the misalignment between the primary dendrite axis with the solidification direction. A schematic showing defined Laue angles is shown in Figure 6.13.
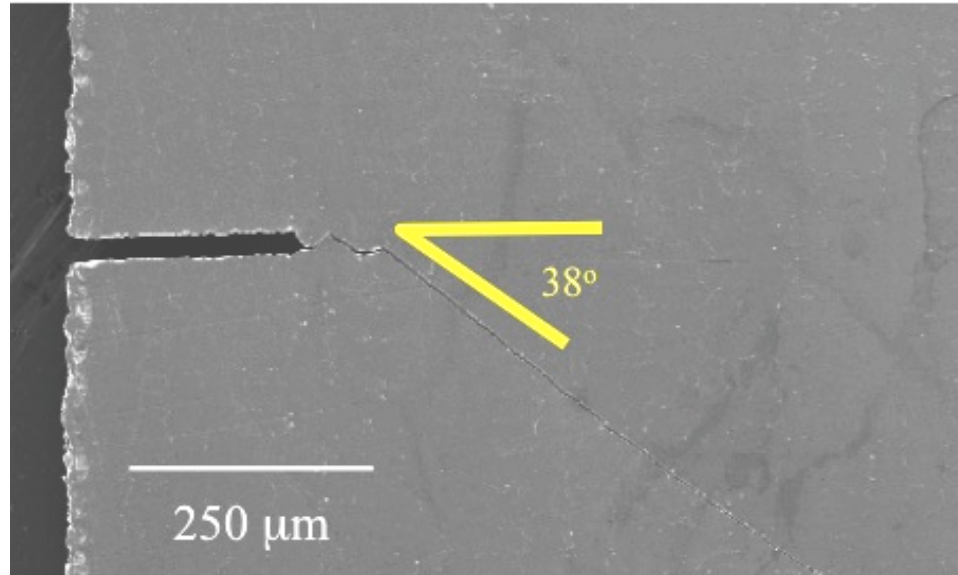
Figure 6.12 SEM image of the free surface of the cracked specimen (Bridgman solidified). The inclination angle of the crack path with respect to the notch and stress axis is indicated.
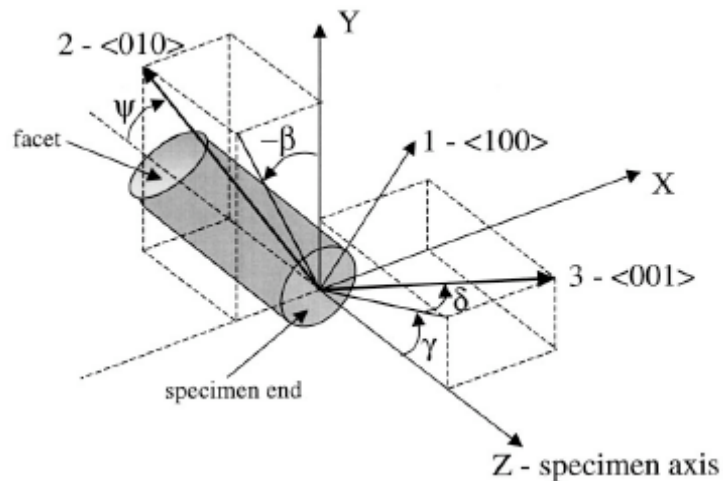
Figure 6.13 Definition of typical Laue angles, δ, β, γ, ψ for single crystal orientation.[4]

Chan and Cruse[5] have shown that an isotropic Mode I stress intensity factor solution is applicable to single crystal crack growth at inclination angles less than 30° from the starter notch. However, due to the fact that inclined crack shown in Figure 6.12 is inclined closer to 45° with respect of the notch, Mode I stress intensity factor calculations are invalid, which necessitated the use of a stress intensity factor solution that incorporated mixed-mode conditions for the inclined crack paths.

6.5   Mixed-Mode Stress Intensity

Due to the crack inclination angles with respect to the loading axis, thickness and width directions, crystallographic analyses were performed in order to determine the fatigue crack propagation mechanism. It should be noted that the single crystal [001] orientation deviated no greater than 15° with respect to the loading direction. The specific crystal orientations for each thin-sheet sample are detailed in Table 6.1.

Section 6.5.1 details the crystallographic analyses employed for measurement of crack planes and propagation directions. Earlier detailed analyses[2] have considered the full set of 12 slip systems using 3-D fracture mechanics analysis to investigate the crack propagation mechanisms at 23°C for a given specimen geometry.   The active crack-tip slip systems and the calculated stress intensity factors for a CMSX-4 alloy will be compared to the cracking behavior exhibited in the present work.

6.5.1   Crystallographic Analysis of Crack Planes

According to crystallographic analyses of cracking planes at notch tips, mixed-mode cracks can be classified into three types as shown in Figure 6.14.[6]   Here, the inclined crack possesses mixed mode I/II components (Figure 6.14a), and an inclined and twisted crack contains mixed mode I, II and III (Figure 6.14b), while a twisted crack has Mode I/III components (Figure 6.14c). It is clear that there exists local mixed-mode stress intensity factors at the crystallographic crack tips regardless of being subjected to nominal Mode I loading.

(a)   (b)

(c)
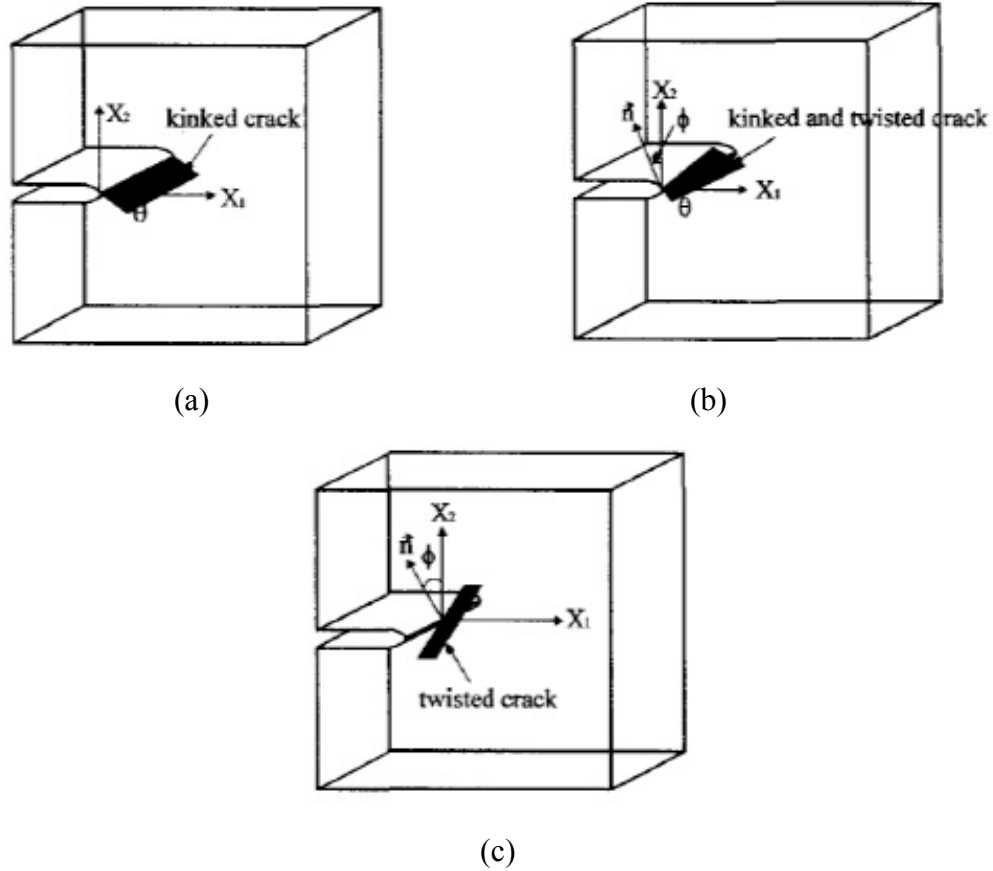
Figure 6.14 Schematic illustration of three possible types of mixed-mode cracks from a notch. (a) Inclined, (b) inclined and twisted and (c) twisted cracks are shown.[6]

As a result of the mixed mode cracking, it is necessary to quantify the locally high shear and tear components at the crystallographic crack tips that would naturally promote the localization of slip and crack propagation along a single {111} slip plane. The direction of load application with respect to the crystal orientation determines the resolved shear stress for each of the {111}<110> slip plane/slip direction sets. An example of octahedral planes and family of slip directions for a single crystal is illustrated in Figure 6.15.
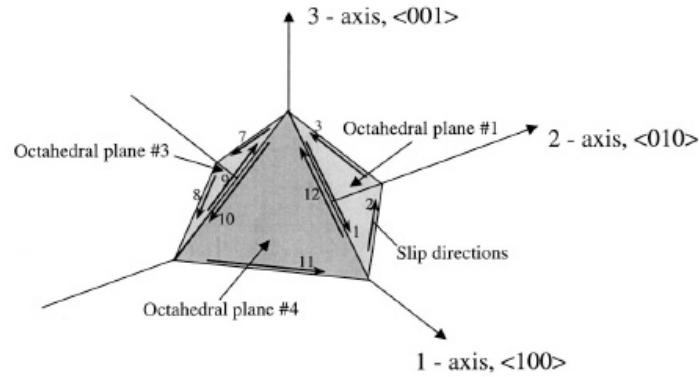
Figure 6.15 Schematic of planes and directions within the octahedral slip system for a single crystal[4]

When the resolved shear stress on any slip system is sufficiently high, slip will occur along that slip system. This information is of relevance since the cyclic stress produces alternating slip reversals on the critical slip systems, which eventually results in the nucleation of a fatigue crack along a critical octahedral plane, as exemplified in bulk samples presented in Chapter 5.

When there are a sufficient number of slip reversals on the critical slip system, fatigue crack initiation occurs along a critical octahedral plane. The stresses and strains along the crystallographic octahedral planes and corresponding slip systems can be determined using 3-D transformation equations. Due to the difference in the orientation of the single crystal axes in 3-D with respect to the loading axis, the use of appropriate 3-D transformation equations for the stress and strain tensors are needed to determine the stress and strains along the crystallographic axes. The three Laue angles, δ, γ, and β, define the direction cosines between the loading axes (X-Y-Z) and crystal axes (1-2-3). The angle, ψ, shown in Figure 6.13 can be given as[7]

$$\tan(\psi) = \frac{\cos(\delta)\cos(\gamma)}{\sin(\delta)\sin(\beta)+\cos(\beta)\cos(\delta)\sin(\gamma)} \qquad [6.2]$$

The direction cosines can be found using classical properties and relationships of direction cosines. The direction cosines, a_{11}, a_{12} and a_{13} can be determined as

$$a_{11} = a_{22} * a_{33} - a_{23} * a_{32} \qquad [6.3]$$

146

$$a_{12} = a_{23} * a_{31} - a_{21} * a_{33} \qquad [6.4]$$

$$a_{13} = a_{21} * a_{32} - a_{21} * a_{31} \qquad [6.5]$$

The 3-D transformation of elastic stresses, $\{\sigma_{XYZ}\}$, in the loading coordinate system to the stresses, $\{\sigma_{123}\}$, is given by the following matrix equation:

$$\{\sigma_{123}\} = [P]^{-1}\{\sigma_{XYZ}\} \qquad [6.6]$$

where the transformation matrices, $[P]$ and $[Q]$ are given in terms of the direction cosines as:[7]

$$[P] = \begin{bmatrix} a_{11}^2 & a_{12}^2 & a_{13}^2 & 2a_{11}a_{12} & 2a_{12}a_{13} & 2a_{11}a_{13} \\ a_{21}^2 & a_{22}^2 & a_{23}^2 & 2a_{21}a_{32} & 2a_{22}a_{23} & 2a_{21}a_{23} \\ a_{31}^2 & a_{32}^2 & a_{33}^2 & 2a_{31}a_{32} & 2a_{32}a_{33} & 2a_{31}a_{33} \\ a_{11}a_{21} & a_{12}a_{22} & a_{13}a_{23} & a_{11}a_{22}+a_{12}a_{21} & a_{12}a_{23}+a_{13}a_{22} & a_{13}a_{21}+a_{11}a_{23} \\ a_{21}a_{31} & a_{22}a_{32} & a_{23}a_{33} & a_{22}a_{31}+a_{21}a_{32} & a_{23}a_{32}+a_{22}a_{33} & a_{21}a_{33}+a_{23}a_{31} \\ a_{11}a_{31} & a_{12}a_{32} & a_{13}a_{33} & a_{11}a_{32}+a_{12}a_{31} & a_{12}a_{33}+a_{13}a_{32} & a_{13}a_{31}+a_{11}a_{33} \end{bmatrix} \qquad [6.7]$$

$$[Q] = \begin{bmatrix} a_{11}^2 & a_{12}^2 & a_{13}^2 & a_{11}a_{12} & a_{12}a_{13} & a_{11}a_{13} \\ a_{21}^2 & a_{22}^2 & a_{23}^2 & a_{21}a_{32} & a_{22}a_{23} & a_{21}a_{23} \\ a_{31}^2 & a_{32}^2 & a_{33}^2 & a_{31}a_{32} & a_{32}a_{33} & a_{31}a_{33} \\ 2a_{11}a_{21} & 2a_{12}a_{22} & 2a_{13}a_{23} & a_{11}a_{22}+a_{12}a_{21} & a_{12}a_{23}+a_{13}a_{22} & a_{13}a_{21}+a_{11}a_{23} \\ 2a_{21}a_{31} & 2a_{22}a_{32} & 2a_{23}a_{33} & a_{22}a_{31}+a_{21}a_{32} & a_{23}a_{32}+a_{22}a_{33} & a_{21}a_{33}+a_{23}a_{31} \\ 2a_{11}a_{31} & 2a_{12}a_{32} & 2a_{13}a_{33} & a_{11}a_{32}+a_{12}a_{31} & a_{12}a_{33}+a_{13}a_{32} & a_{13}a_{31}+a_{11}a_{33} \end{bmatrix} \qquad [6.8]$$

The transformation of the elastic strains $\{\varepsilon_{XYZ}\}$ is shown as

$$\{\varepsilon_{123}\} = [Q]^{-1}\{\varepsilon_{XYZ}\} \qquad [6.9]$$

Therefore, the transformed stiffness matrix in the specimen coordinate system is described by the following transformation:

$$[C_{ij}] = [P][C_{i'j'}][Q]^{-1} \qquad [6.10]$$

147

where $[C_{ij}]$ and $[C_{i'j'}]$ are the elastic stiffness matrices in the specimen geometry and crystal coordinate, respectively. Since $\sigma_i = \Sigma\, C_{ij}\varepsilon_j$, the transformed compliance matrix can be determined when the elastic constants, E, ν and G are known in the crystal coordinate system and direction cosines between the crystal and loading coordinate systems. Liu *et al.*[2] have determined constants of $C_{11} = 245$ GPa, $C_{12} = 155$ GPa and $C_{44} = 129$ GPa for CMSX-4 at $T = 23^{\circ}$C. It is expected that similar constants are exhibited in the René N5 specimen since it possesses a similar alloy composition and Young's modulus (129 GPa).

Using 3-D linear elastic fracture mechanics analyses,[2] the crack tip stress components can be expressed as

$$\sigma_{ij}(r,\theta) = \frac{1}{\sqrt{2\pi r}}\left[K_I f_{ij}(\theta) + K_{II} g_{ij}(\theta) + K_{III} h_{ij}(\theta)\right] \tag{6.11}$$

where f_{ij}, g_{ij} and h_{ij} represent the geometrical functions defining the angular dependency of the stress field, with r being the radial distance from the crack tip and θ is equal to the angle between the trace of a particular slip plane on the faces of the specimen and horizontal axis. K_I, K_{II} and K_{III} are the Mode I, II and III stress intensity factors, respectively, that reflect the redistribution of stress in the thin-sheet due to the introduction of a crack.

Figure 6.16a shows Mode I and II stress intensity factor calculations for the inclined crack shown in Figure 6.16b, and the corresponding da/dN vs ΔK data. For an infinite plate with a crack with length $2a$ and subjected to a normal stress σ_y and shear stresses τ_{xy} and τ_{yz}, the stress intensity factors can be defined as[8]

$$K_I = \sigma_y\sqrt{\pi a} \tag{6.12}$$

$$K_{II} = \tau_{xy}\sqrt{\pi a} \tag{6.13}$$

$$K_{III} = \tau_{yz}\sqrt{\pi a} \tag{6.14}$$

The difference in Mode I and II intensities for a normally oriented crack is shown in Figure 6.18, where the contribution of Mode I dominates Mode II. The greatest difference in ΔK occurs during the long crack growth period.

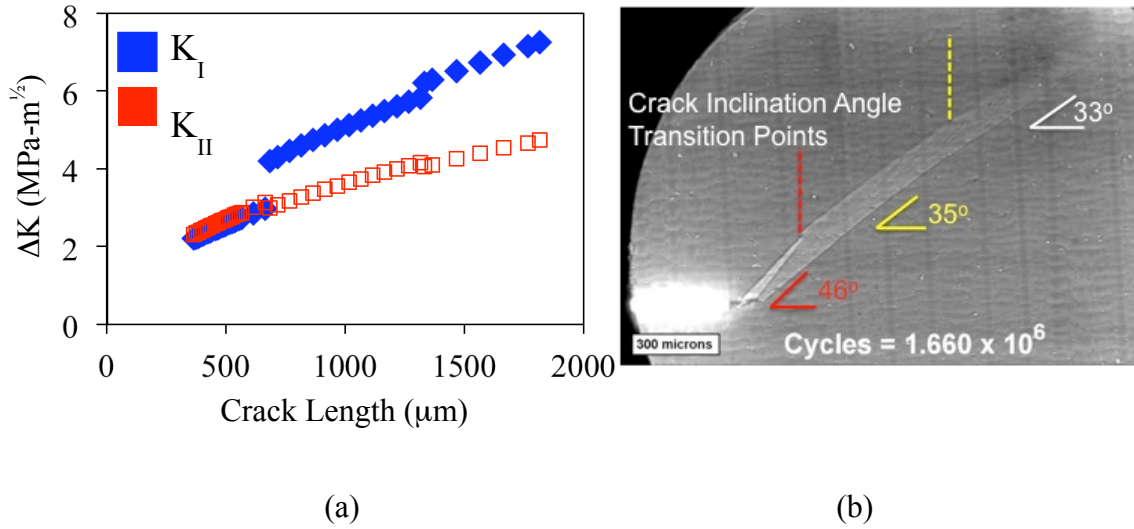(a)   (b)

Figure 6.16 (a) Mode I and II stress intensity calculations for a fatigued LMC solidified sample (b) shown for the inclined crack. Cycled at $T = 23^o$C.
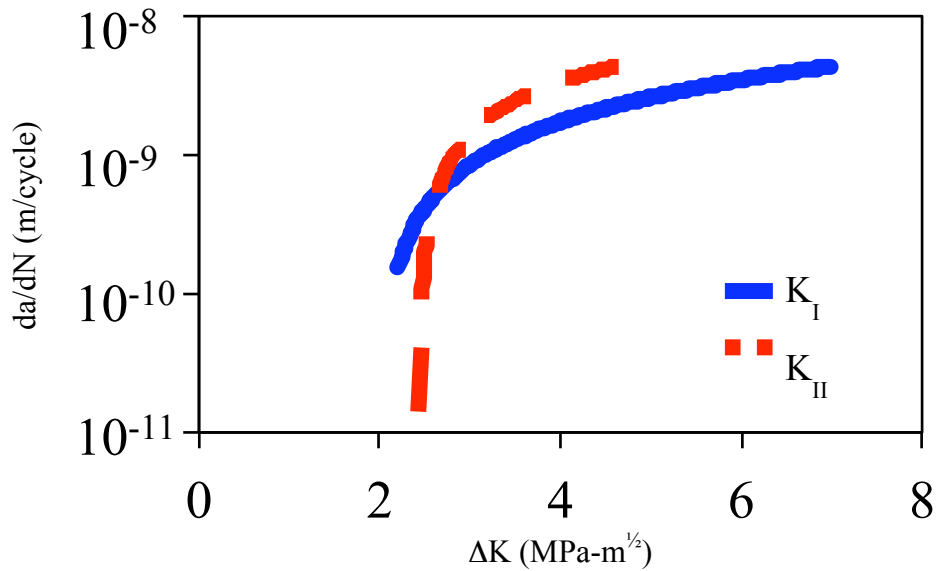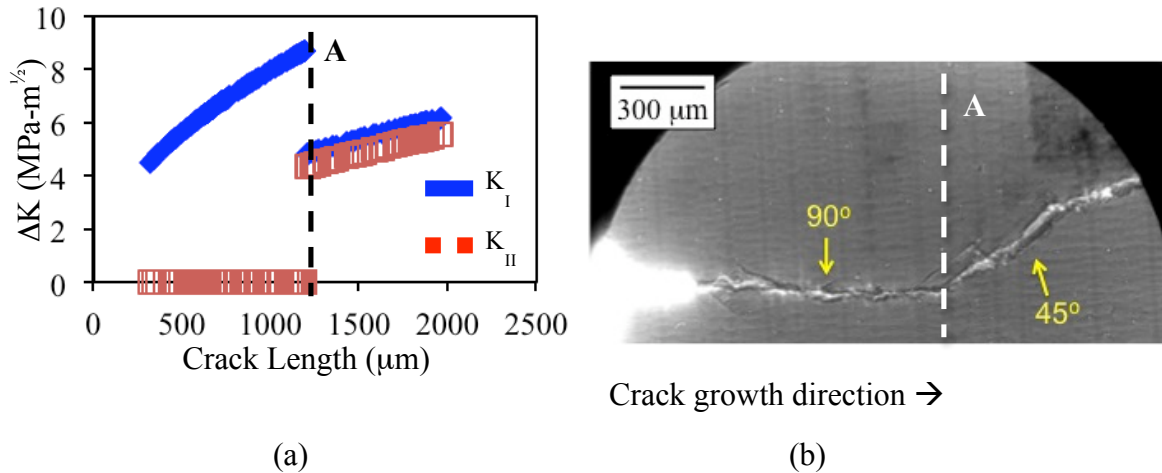

Figure 6.17 Crack growth rate measurements using Mode I and II stress intensities for LMC solidified sample shown in Figure 6.9. Cycled at $T = 23^o$C.

Crack growth direction →

(a)   (b)

Figure 6.18 (a) Mode I and II stress intensity factor measurements for LMC solidified sample tested at 580°C shown in (b). Dashed line, A, indicates the crack mode transition point shown in X-ray image (b).

6.6   Crack Plane Transition

Figure 6.19 displays X-ray images collected during cycling of a LMC and Bridgman solidified sample coincident with octahedral {111}<110> systems. The cracks initiated and propagated through the samples at various inclination angles as detailed in Table 6.1. In both samples, the crack plane transitioned onto an alternate plane after a given distance, then continued to propagate through the remaining single crystal material. Arrows on the micrographs indicate position of the crack plane transition. The crack extension per cycle for the front and back faces of the cracks in Figure 6.19b is shown in Figure 6.20. A notable period of crack arrest was observed in this sample, in which the crack front was arrested near a pore (Figure 6.19b) before changing to an alternate crack plane.

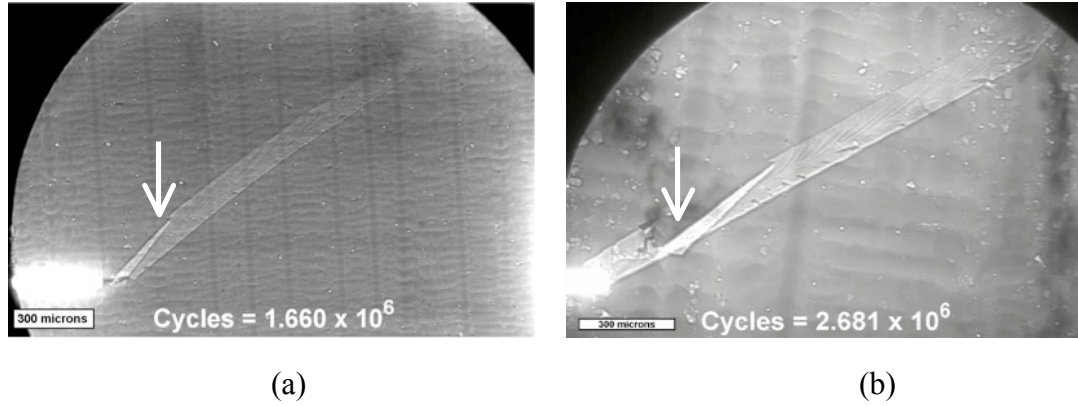(a)   (b)

Figure 6.19 Synchrotron X-ray images of fatigue cracks grown under constant displacement amplitude at ambient temperature. The loading axis is vertical to the notch plane. Image in (a) was taken of a LMC solidified sample, whereas (b) shows a Bridgman solidified sample with larger primary dendrite spacings. Arrows indicate the location of a crack plane transition.
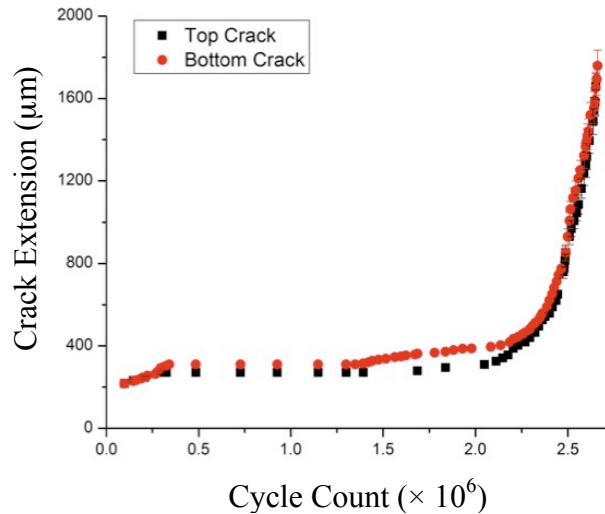
Figure 6.20 Projected crack length per cycle count during crack growth of a Bridgman solidified sample at ambient temperature. Measurements of the crack on front and back faces of the specimens are indicated.

Interestingly, all LMC solidified samples exhibited a crack plane transition after a distance of approximately 330 μm from the notch root. The multiple through-thickness cracks near the notch indicate that crystallographic cracking can occur on two or more slip planes simultaneously. The crack paths shown were generated along planes that were subjected to large shear stresses and shear strains. A slip-band decohesion model[9] has been used to describe the reversed motion of dislocations on a series of parallel planes forming an array of dipoles in the plastic zone. The stress causes localized

151

separation of the atomic bonds across the slip plane, causing the formation of a crack, which is detailed with the through-thickness imaging.

A magnified view of a crack that has transitioned to an alternate crack plane is shown in Figure 6.21. This transition was exhibited at an identical distance from the notch tip within both samples containing a $\lambda_2 = 25$ μm. Since the presence of a notch serves as a stress concentration, leading to a localized increase in stresses and strains, it is of importance to understand the impact of the residual stress field on crack plane transitions. Stress intensity factors can be determined from the limiting values of elastic stress concentration factors as the notch root radius approaches zero, see Equation 6.11. Assuming the notch, shown in Figure 6.21, is embedded within a Mode I stress field, the maximum stress, σ_{max}, will occur directly ahead of the notch as

$$\sigma_{max} = 2\sigma_{nom}\sqrt{\frac{a}{\rho}} \qquad [6.15]$$

where σ_{nom} is the nominal applied tensile stress, a is the edge notch length, and ρ is the radius of curvature of the crack tip. The stresses in a sheet containing a notch (with diameter a) and axially loaded can be expressed as[10]

$$\sigma_{rr} = \frac{\sigma}{2}\left(1-\frac{a^2}{r^2}\right)+\frac{\sigma}{2}\left(1+3\frac{a^4}{r^4}-4\frac{a^2}{r^2}\right)\cos(2\theta) \qquad [6.16]$$

$$\sigma_{\theta\theta} = \frac{\sigma}{2}\left(1+\frac{a^2}{r^2}\right)-\frac{\sigma}{2}\left(1+3\frac{a^4}{r^4}\right)\cos(2\theta) \qquad [6.17]$$

$$\sigma_{r\theta} = -\frac{\sigma}{2}\left(1-3\frac{a^4}{r^4}-\frac{2a^2}{r^2}\right)\sin(2\theta) \qquad [6.18]$$

According the Equations 6.16-6.18, the end of the tensile residual field would occur after an inclined crack length of 310 μm, which was near the distance of the crack plane transition point from the notch. It is evident that the $1/\sqrt{r}$ type singularity in the stress field equation is a controlling feature in fracture size effects, crack plane transitions

within a stress field due to a notch, and provides the relationship of stress concentration to stress intensity factor.
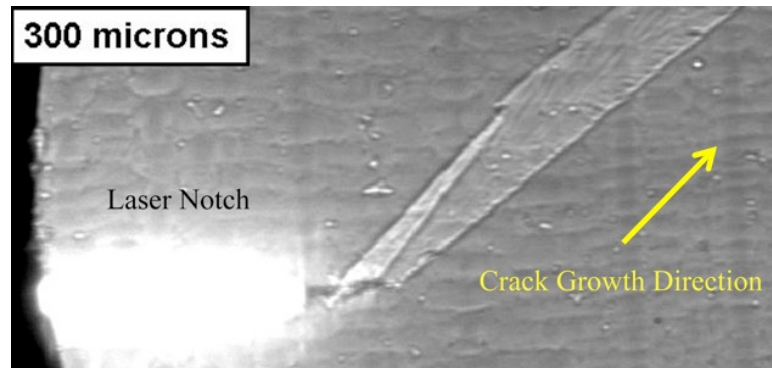
Figure 6.21 X-ray radiograph of a fatigue crack in a LMC solidified sample (T= 23°C) near the laser notch.
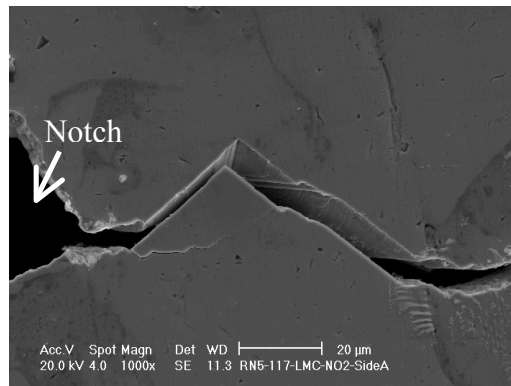
Figure 6.22 SEM image of a fatigue crack (T=23°C) that initiated from the notch within a LMC solidified sample during high frequency cycling. Image was taken near the notch tip to emphasize the alteration in crack propagation plane during the initial stages of crack growth.

Contrastingly, the Bridgman solidified samples did not always exhibit the same behavior during each test. An example of smooth crystallographic cracking along a single crack plane within a Bridgman solidified is shown in Figure 6.23 for comparison to Figure 6.19b. The SEM images in Figure 6.24 present various fracture surface features exhibited at ambient temperature for all samples tested, specifically the smoothed faceted surface and slip band formation.
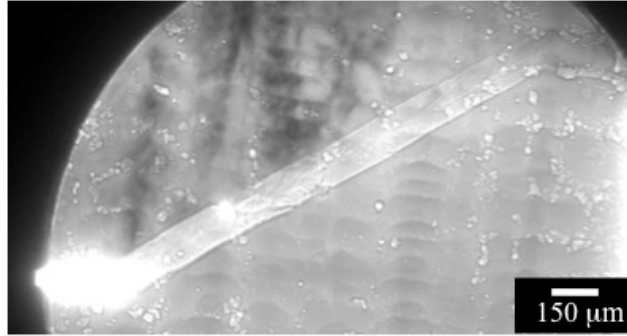
Figure 6.23 Inclined crack path of a Bridgman solidified sample tested at ambient temperature.

(a)

(b)

(c)
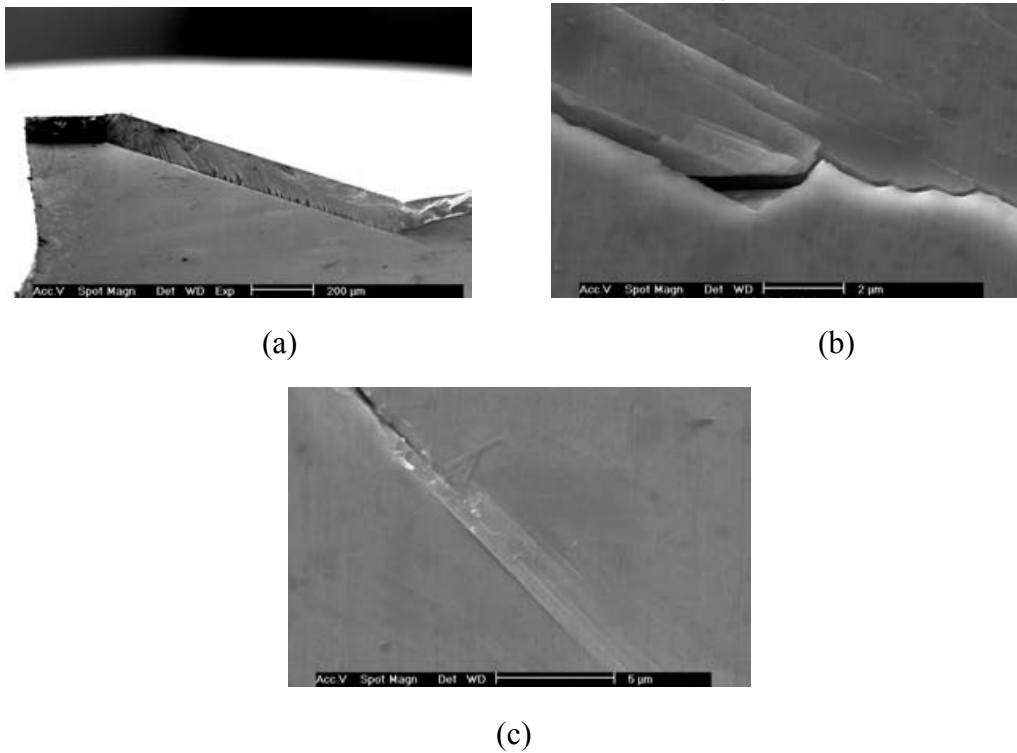
Figure 6.24 SEM images displaying typical crack propagation features of thin-sheet specimens at room temperature. Examples of a (a) planar fracture surface, (b) opening of a fatigue crack near slip bands and (c) slip bands formation at the free surface.

Similar instances of slip band formation have been investigated in single crystal nickel base superalloys CM186LC and CMSX-4 under ultra-high cycle fatigue conditions at 850°C ($f = 95$ Hz).[11] Figure 6.25 presents the features of the bands with SEM and TEM techniques. The favorable conditions for slip band formation in single crystals will be discussed in detail in Section 6.8.
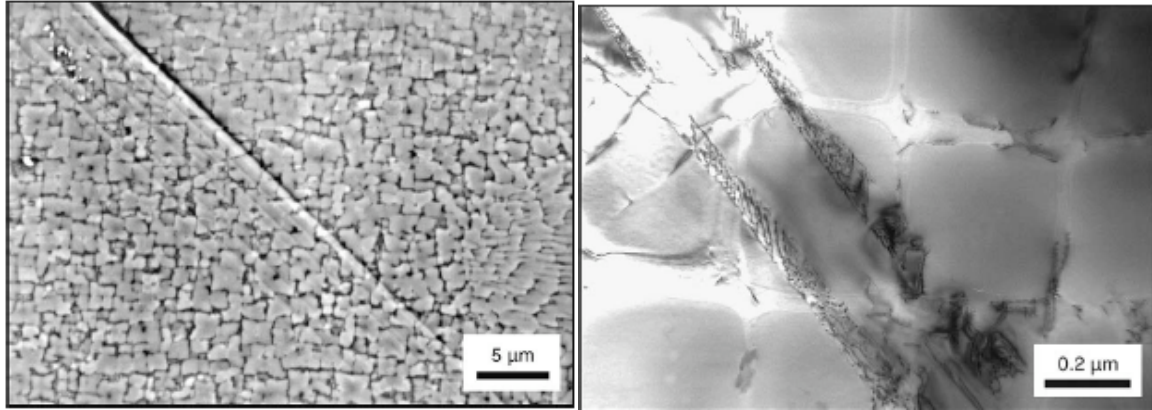
(a)   (b)

Figure 6.25 (a) Slip bands observed in CM186LC single crystal cycled at σ_a = 120 MPa, T = 850°C. (b) TEM image of slip bands observed in CMSX-4 single crystal at σ_a = 120 MPa, T = 850°C.[11]

In-situ images and post-mortem SEM analysis of the inclination angles of the fracture plane and crack growth direction indicated that cracking at ambient temperature occurs on planes coincident with the {111}<110> crystallographic slip system. Figure 6.26 displays the various angles measured within a failed sample, exemplifying the inclination of the crack with the thickness, loading and width direction. A schematic of the possible slip systems for the single crystal crack displayed in Figure 6.9 (LMC-1) at ambient temperature is shown in Figure 6.27.

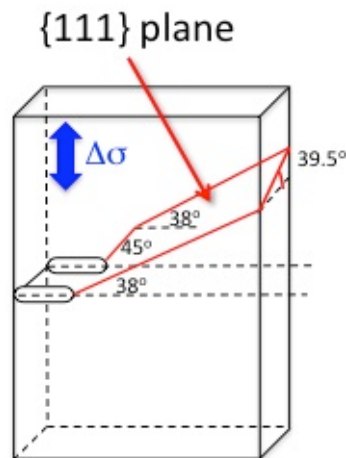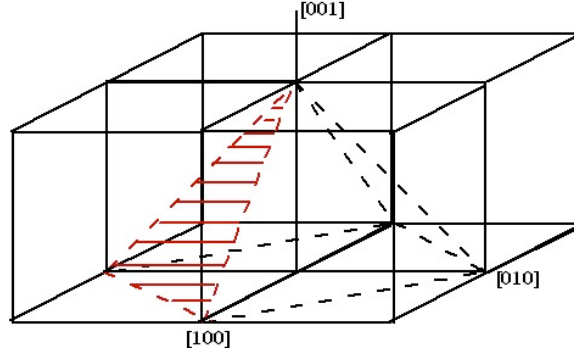**Figure 6.26 Schematic of the various inclination angles of a crack (sample LMC-1) with respect to the loading axis, specimen thickness and width direction.**

155

Figure 6.27 Schematic of possible octahedral planes for crystallographic cracking.[2]

6.6.1 Crystallographic Crack Growth

Due to the change in crack plane, it is important to consider the contributions from the stress intensity factors that are present due to the normal and shear stresses imposed on the octahedral slip systems during the cyclic slip localization process near the notch root. Liu *et al.*[2] have used Equations 6.19 and 6.20 to describe a resolved normal stress intensity coefficient, K_{RNSIC}, and resolved shear stress intensity coefficient, K_{RSSIC} as:

$$K_{RSSIC} = [b_{i'}][a_{i'j}][K_I, K_{II}, K_{III}, f(\theta_s)][a_{ij'}][n_{j'}] \qquad [6.19]$$

$$K_{RNSIC} = [n_{i'}][a_{i'j}][K_I, K_{II}, K_{III}, f(\theta_s)][a_{ij'}][n_{j'}] \qquad [6.20]$$

where K_{RNSIC} and K_{RSSIC} are analogues to K_I and K_{II}, respectively. The K_{RSSIC} parameter represents the driving force for shear decohesion of the active slip plane, while K_{RNSIC} is the intensity of the normal stress acting on the active slip plane, which causes separation of the surfaces. As discussed in Chapter 5, these surfaces are separated due to the cyclic slip localization process on slip planes weakened by the dislocation movement. K_{RNSIC} and K_{RSSIC} have been used to characterize inclined cracks within the thin-sheet material of CMSX-4[2] to explain the crack growth transition from one slip plane to an alternative one. The calculations indicate that a crack could initiate on multiple slip planes from the laser notch root. However, with continued growth during cycling, the stronger contribution from the K_{RSSIC} determines the possibility of a transition to an alternate crack plane or continued growth on the initial plane. This evidently was the cause of the crack

156

plane transitions exemplified in the two LMC solidified specimens (LMC-1 and LMC-2), where one sample is magnified in Figure 6.21. The crack plane change near an interdendritic feature in sample Bridgman-3, shown in Figure 6.11, will be discussed in Section 6.8, since it was a unique behavior in comparison to all other cracks grown at ambient temperature. This was the only crack plane change exhibited in the coarse scale microstructure.

6.7 Crack Growth at Elevated Temperatures

Figure 6.28 presents X-ray images of fatigue cracks produced within a LMC cast sample at 538°C, identified as LMC-4 and LMC-5 in Table 6.1. A rougher fracture surface can be observed in the X-ray images, compared to room temperature tested samples. The crack inclination angles were notably smaller than crack angle measurements exhibited at ambient temperature.

In Figure 6.28a, an abrupt crack plane change was observed after 290 μm of crack extension from the notch. The crack subsequently grew on that particular {111} plane until complete fracture. Crack deflection was observed in Figure 6.28b after 651 μm of crack growth from the notch onto an alternate {111} plane. Figure 6.29 presents the crack extension per cycle for each of the samples tested, with the crack deflection point indicated with the dashed line.

(a)   (b)
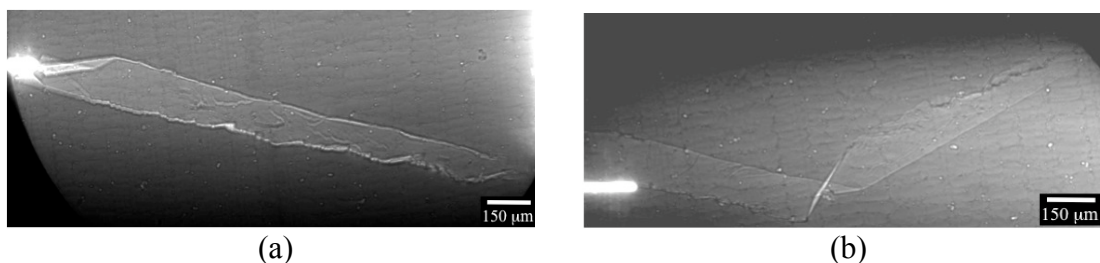
Figure 6.28 X-ray images of high cycle fatigue cracks tested at 538°C for a René N5 microspecimens solidified with the LMC process for samples (a) LMC-4 and (b) LMC-5.
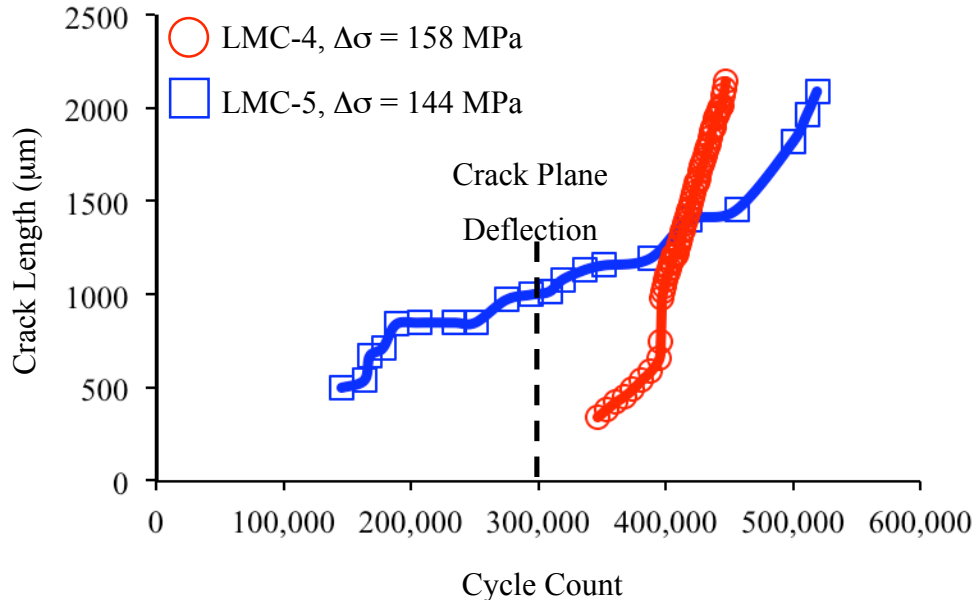
Figure 6.29 Crack growth measurements for two LMC solidified samples tested at 538°C, *R* = 0.1.

There was a marked change in the crack growth rate in sample LMC-4, with the crack initially growing at a slower rate from the notch, followed by faster crack growth after 381 μm of crack extension.

In sample LMC-5, the crack grew at a 35° inclination angle from the notch, followed by a deflection of 15° with respect to the notch plane until failure. Figure 6.30 shows a magnified view of the angle of the crack deflection from the initiation plane to final crack plane. The plot (Figure 6.29) details the decrease in crack growth rate as it deflected on to an alternate plane at a 45° angle with respect to the previous crack plane.
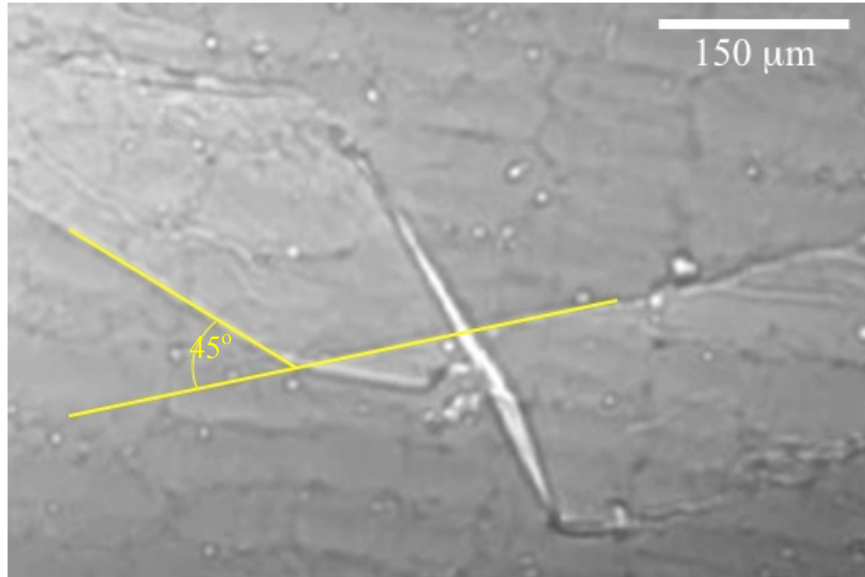
Figure 6.30 Magnified view of sample LMC-5 (T = 538$^{\text{o}}$C), emphasizing the crack deflection angle, which initiated from the notch onto another plane {111}.

Fractography of the samples revealed faceted fracture surfaces, similar to the samples tested at room temperature tested samples. Similar to ambient temperature, these samples exhibited cracking along octahedral crystallographic planes. Figure 6.31-6.33 displays SEM images magnified near the crack deflection point in each sample. The bands that were exhibited near the deflection points indicated that samples endured an intensified slip localization process during fatigue.
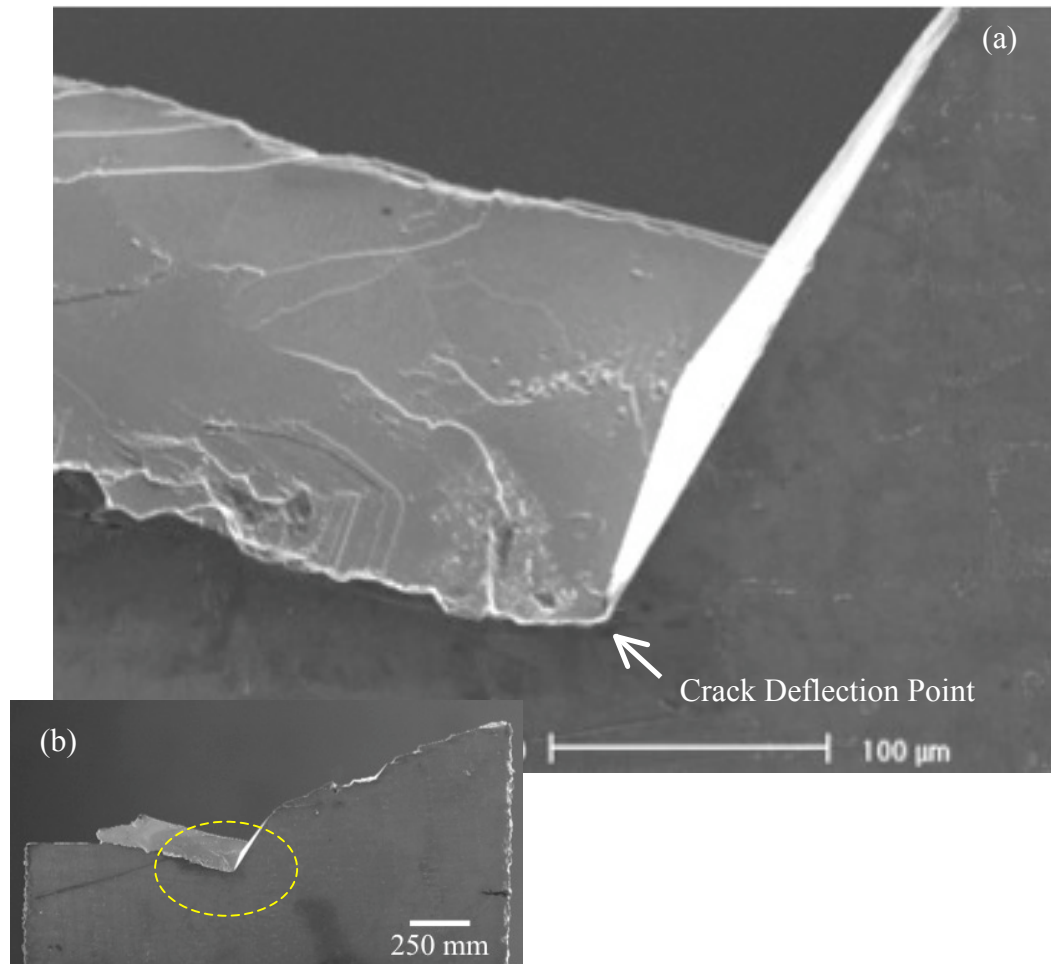
Figure 6.31 (a) SEM image of a highly magnified view of a deflected crack in sample, LMC-5. The inset image displays the low magnification image of free surface.
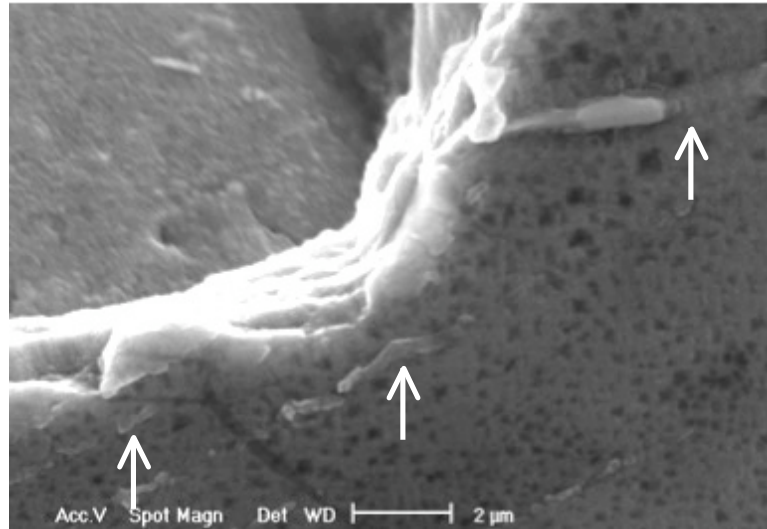
Figure 6.32 SEM image of a magnified view of the crack deflection point in sample, LMC-5. Slip bands, marked with arrows, on the free-surface along one direction can be observed near the deflection point.
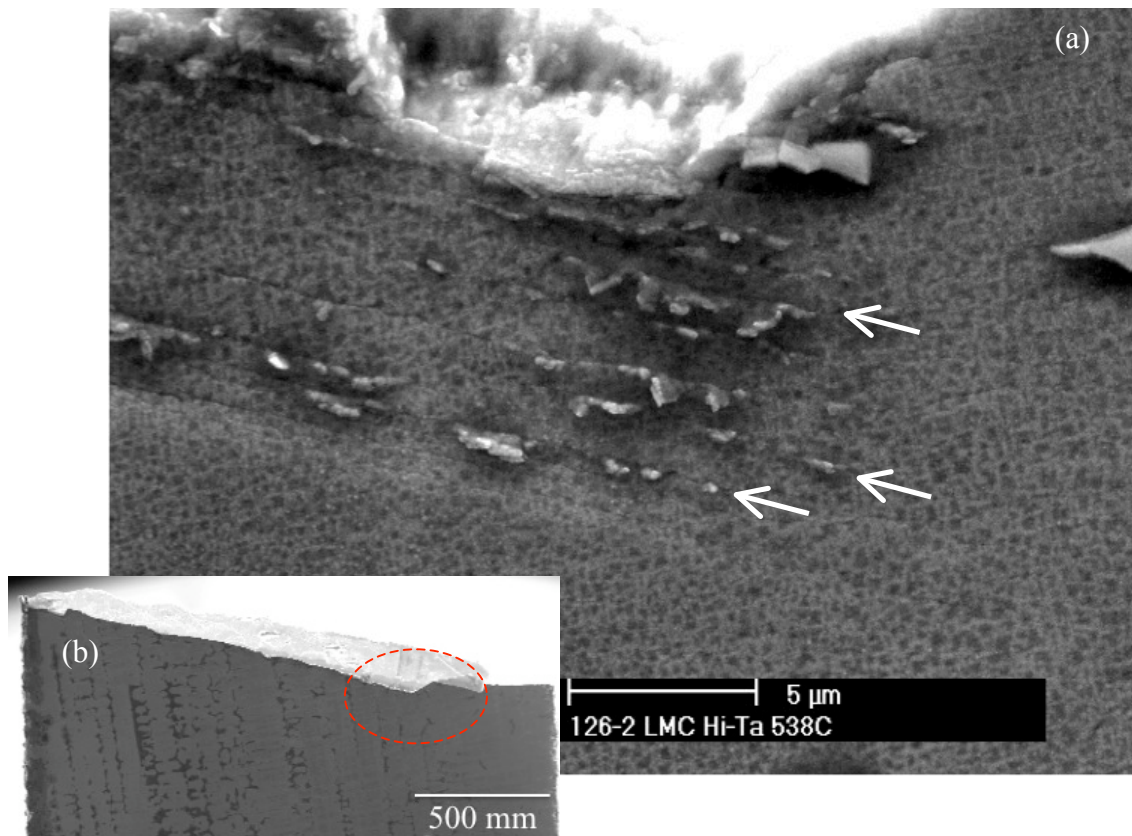
Figure 6.33 SEM image of a highly magnified view of a crack that switched to an alternate plane in sample LMC-4. The white arrow in the image identifies a slip band. The inset image (b) displays the low magnification image of free surface.

161

The highly faceted fracture surfaces observed in the thin-sheet samples were consistent with the fractures in bulk samples tested at 20 kHz at 538°C, Figure 6.34, where highly crystallographic cracks grew on one or more intersecting {111} type planes.[12] This indicates that no critical differences on the crack growth behavior in thin sections and bulk samples existed.
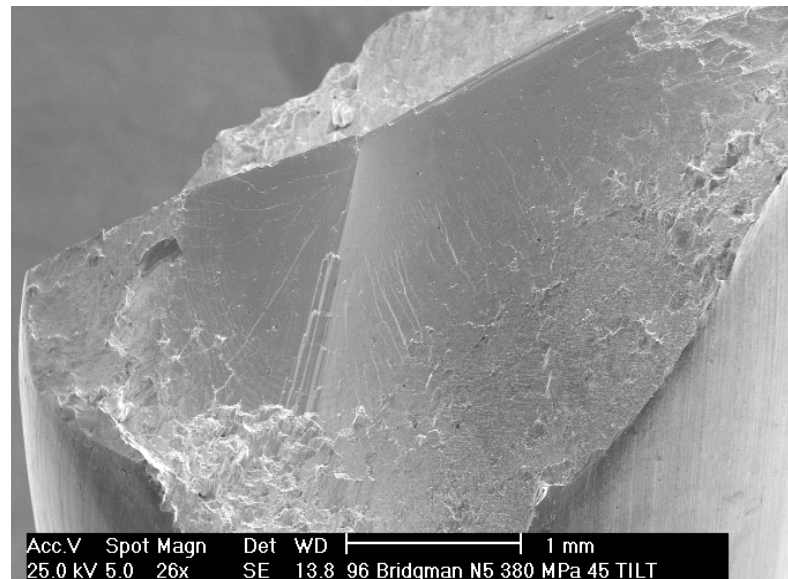
Figure 6.34 A tilted view of the fracture surface within a Bridgman solidified bulk sample fatigued at 538°C, $R = 0$, $\Delta\sigma = 380$ MPa.

6.7.1 Transition of Crack Growth Mode at Elevated Temperature

Two LMC solidified samples were subjected to fatigue testing at 580°C. Cracking began immediately at the lowest amplitude value available for the step test ($\Delta\varepsilon_{amp} = 400$ µε). Figure 6.35 presents the fatigue cracks exhibited for applied stress ranges of 83.6 and 83.7 MPa for (a) and (b), respectively. In Figure 6.35a, the crack propagated predominately perpendicular to the stress axis. After approximately 650 µm of crack growth, the crack began to grow crystallographically along an inclined angle. At the end of the Mode I crack, slip lines propagating at complementary angles with respect to one another are magnified in Figure 6.36. Subsequently, the dominant crack continued to propagate through the microstructure until final fracture.

162

(a)   (b)
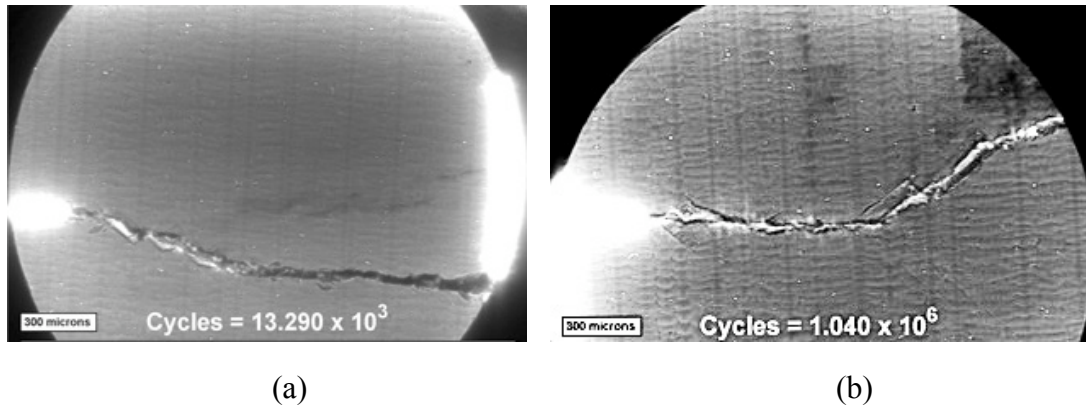
Figure 6.35 X-ray images of LMC solidified samples tested at 580°C.
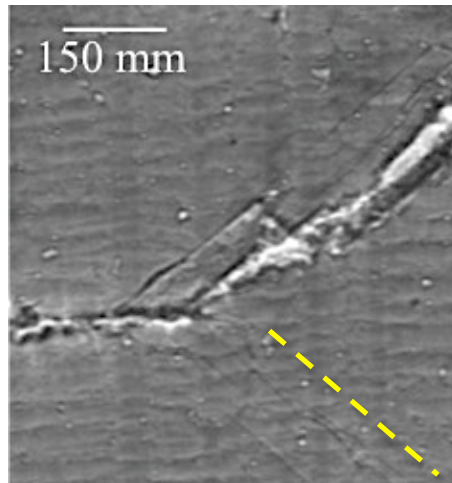
Figure 6.36 Magnified view of the transition of Mode I to mixed-mode crack growth in a 580°C tested sample. Visible slip lines at a 45° angle, complementary to the inclined fatigue crack, are highlighted with the yellow dashed line.
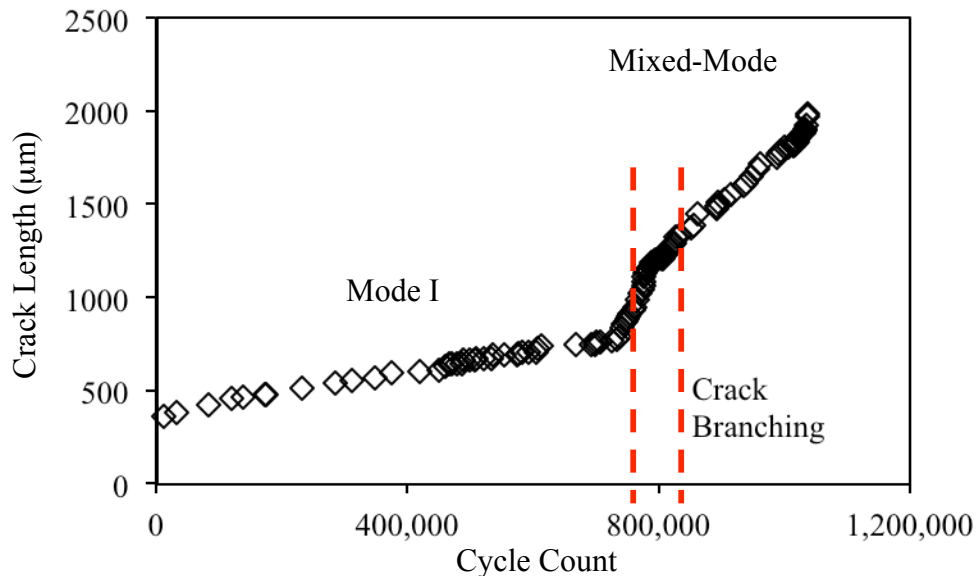
Figure 6.37 Crack growth measurements for LMC-9 tested at 580°C (sample shown in Figure 6.36). Points A and B display the fluctuations in crack growth rate corresponding to the locations that the crack attempted to transition to an alternate {111} plane.

Numerous studies have been conducted in order to understand the fatigue life and fatigue crack propagation behavior as a function of cyclic frequency, temperature and environment.[9,13,14,18] These studies have collectively demonstrated that fatigue crack propagation in nominally [001] oriented single crystals favors either growth along octahedral {111} planes or follows a Mode I path perpendicular to the tensile axis. Crack growth on octahedral planes is favored at lower temperatures and higher frequencies (>10 Hz) and is associated with the formation of localized cyclic deformation on FCC slip systems. This formation is highly dependent on the combined shear and normal stresses, with the former associated with the damage accumulation from irreversible cyclic deformation, while the latter is required to cause crack growth in the damaged regions.

Predicting the damage tolerance for turbine airfoils has been an arduous task due to the advances in turbine blade materials, which have addressed the need for higher strength at higher temperatures. Due to the differences in alloy composition within single crystal superalloys, the fracture properties can vary with operating temperature, stress state and frequency.[15] For the refined microstructure ($\lambda_2 = 25$ μm), the temperature range for mixed-mode cracking along specific crystallographic planes ($T < 538$°C) and Mode I type behavior has been determined. This information is especially relevant for

164

applying a damage tolerant life prediction model for turbine engine components subjected to steady and vibratory stresses at elevated temperature. The fracture modes observed in the thin-sheet René N5 single crystals are in agreement with findings elsewhere.[15,18] In general, accurate life predictions for single crystal alloys require the ability to predict the mode of fracture operates at a specific temperature. It is clear that cracks may propagate at different rates and along different paths, depending on the fracture mode.

6.7.2   Failure Mode Transition

The transition of the fatigue cracking from a Mode I to a {111} octahedral mode (Figure 6.31b) can be explained by invoking environmental damage mechanisms. A similar failure mode transition was reported by Cunningham *et al.*[15] for single crystal PWA 1484 fatigued at lower temperatures in air. They observed global octahedral fracture in single crystals at 204°C; however, at 427°C the failure mode was determined as Mode I. Global octahedral fracture is defined here as crack propagation through the crystal lattice along the global {111} planes. The change in crack growth mode was attributed to environmental damage by oxygen embrittlement. In this mechanism, the formation of an oxide layer ahead of the crack tip or the embrittling effect of bulk oxygen absorption ahead of the crack tip can occur during fatigue.[16] An oxidized free surface of a sample fatigued at 538°C with an initial Mode I crack is displayed in Figure 6.38. Regions of the oxidized layer that spalled from the surface are indicated in the figure.
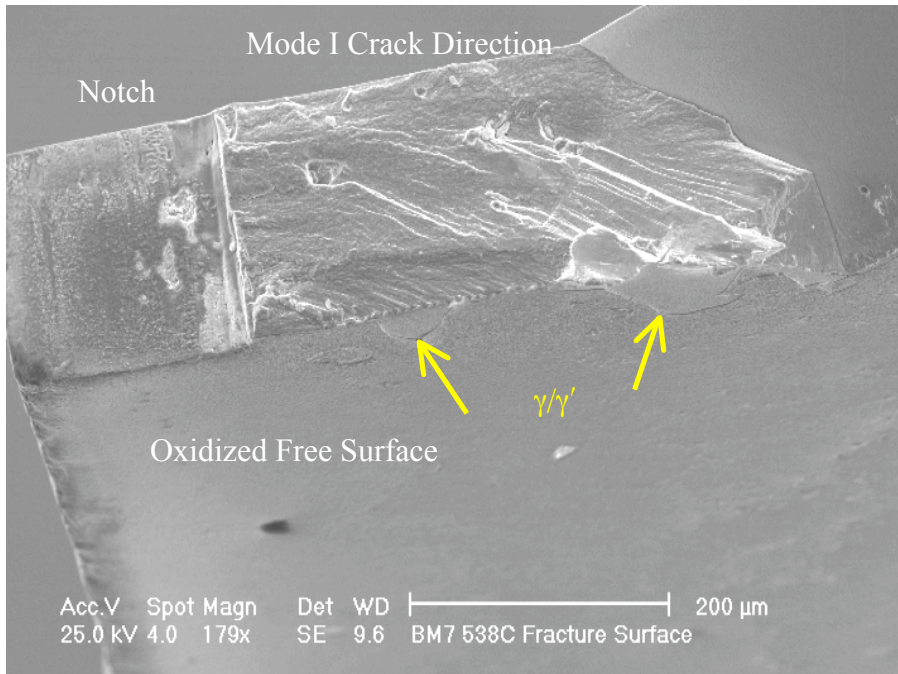
(a)
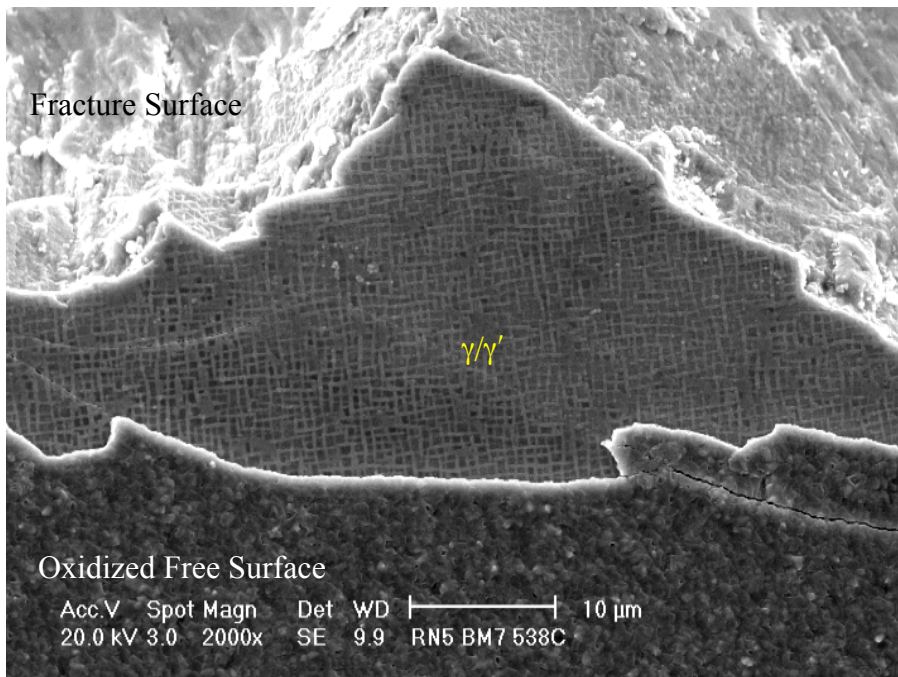
(b)

Figure 6.38 (a) A portion of a fracture surface of thin-sheet specimen (Bridgman-6) tested at 538°C displaying evidence of oxidation. (b) High magnification SEM image near fracture surface of sample Bridgman-6.

Crack growth rates in air (Figure 6.39) can be compared to those in vacuum (Figure 6.40) for René N5 at various temperatures at f = 10 Hz .[20] A decrease in crack growth rate at the higher stress intensities can be observed for tests performed in air, owing to the oxide-induced crack closer effects.
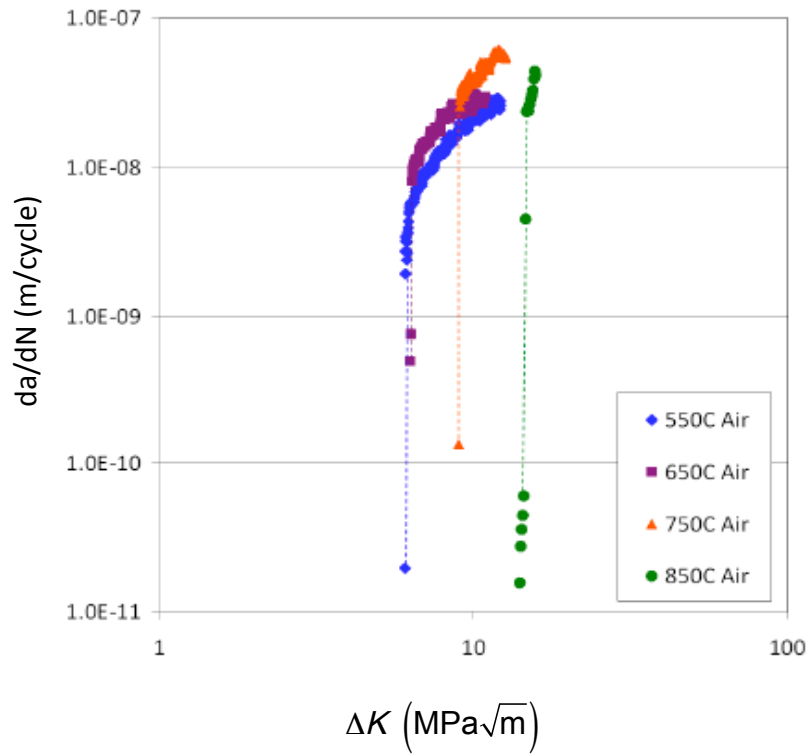
Figure 6.39 Crack growth rate vs. stress intensity factor at various temperatures tested in air for a René N5 superalloy.[20]
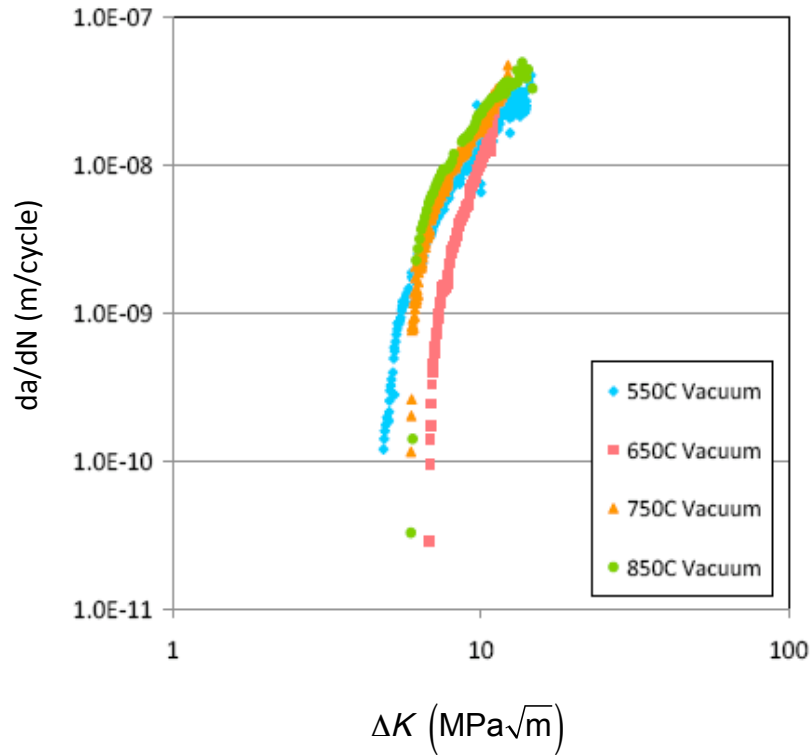
Figure 6.40 Crack growth rate vs. stress intensity factor at various temperatures tested in vacuum for a René N5 superalloy.[20]

McGowan and Liu[17] have suggested that for a given ΔK, there exists a corresponding fatigue crack increment cycle Δa_f, which is caused by the fatigue process, devoid of the environmental influence. If Δa_f is substantially greater than the depth of environmental penetration per cycle, Δa_p, then the fatigue cracking is influenced primarily by a non-environmental fatigue process. However, if Δa_p is greater than Δa_f, then the environmental mechanisms determine the fatigue crack growth behavior. A decrease in frequency has been shown to allow more time for oxygen penetration depth to increase and drive the failure mode away from an octahedral to a non-crystallographic Mode I type.[18] The same type of mechanism can be used to explain the transition from Mode I to octahedral fracture which occurred for sample Figure 6.35b. The transition can be explained by observing that the change to an octahedral failure mode occurred in the high da/dN and high ΔK regime. It is likely that at these stress intensities, the resultant fatigue crack growth rates exceeded the rates of oxygen penetration at the crack tip, which is in agreement with the hypothesis put forth by McGowan and Liu.[17]

168

[001]   Crack Growth Direction →
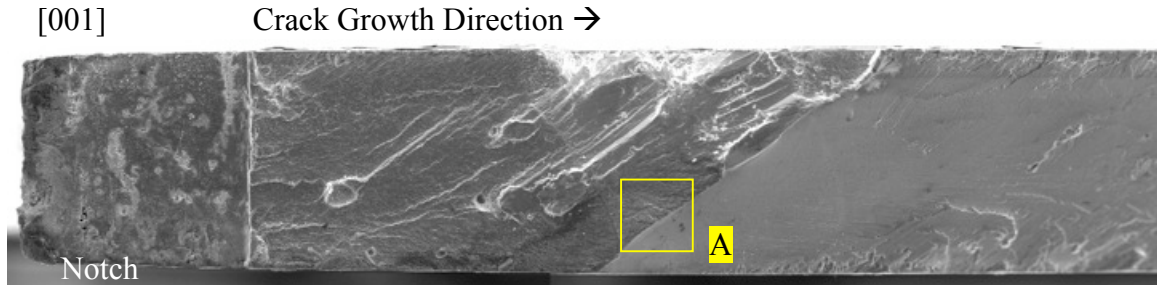
(a)
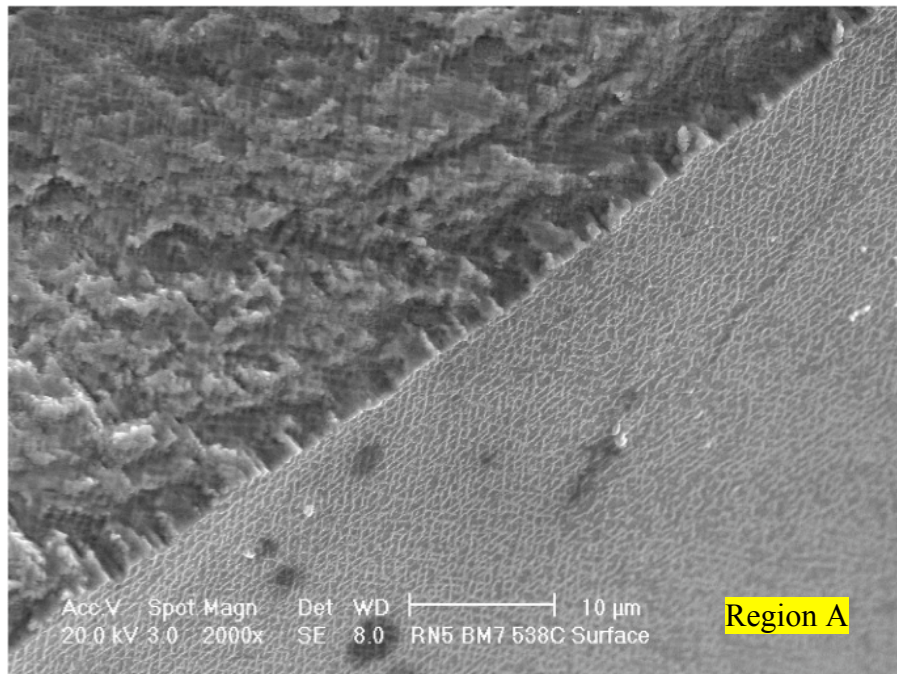
(b)

Figure 6.41 (a) Fracture surface of Bridgman-6 sample tested at 538ºC, displaying the transition in crack mode from Mode I to mixed mode. (b) Highly magnified image of the transition point labeled "Region A" revealing distinctly contrasting fracture surface textures.

Oxidation at the crack tip may be a dominant factor to fatigue crack growth at 538ºC. It is known that oxide induced closure causes crack tip blunting and reduces crack growth rates.[19] This process was observed in CMSX-4 and René N5 where the γ matrix was preferentially oxidized after 1 hour of exposure during 3-point bend cyclic testing at f = 0.25 Hz (T = 650ºC).[19] Further analysis of the thickness of the oxide layer would be needed to attribute the fatigue degradation to oxygen interaction with material at the crack tip.

Reed and Miller[19] have also reported that crack initiation within CMSX-4 was controlled by porosity and/or oxidation depending on the temperature and applied stress levels. Generally, tests performed in vacuum gave longer lifetimes at 650°C than in air. This also provides an explanation to the longer lifetimes exhibited in samples which incurred internal crack initiations from casting pores in comparison to subsurface initiations (Chapter 5).

| (a) | (b) |
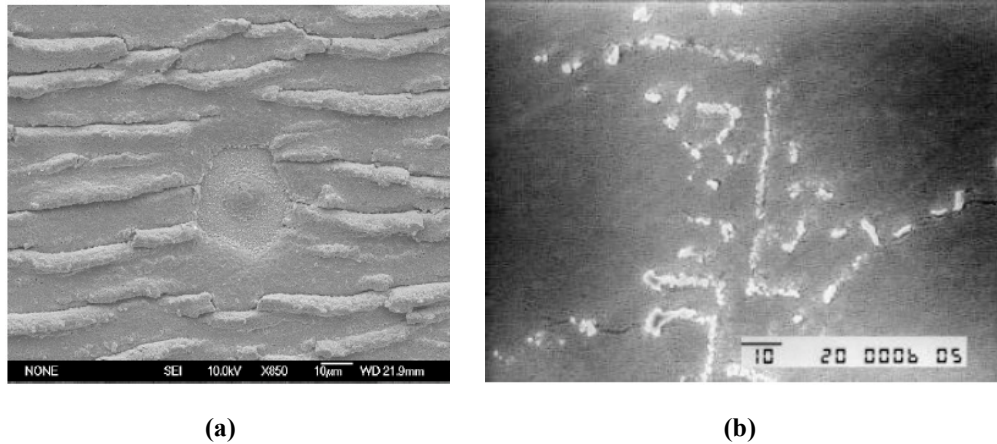
Figure 6.42 (a) Rumpled oxide scale in notch root of CMSX-4 and circular in-filled surface pore. (b) Oxidized interdendritic carbides in René N5 sample after exposure in air for 1 hour.[19]

6.8   Influence of High Temperature on Fatigue Crack Growth

Figure 6.43 displays a LMC sample that was subjected to fatigue testing at 720°C, in which more increment steps of cycling were imposed to initiate a crack (shown in Table 6.1). The SEM image in Figure 6.43 displays the crack growing predominately perpendicular to the stress axis. The corresponding X-ray image is displayed in Figure 6.45.
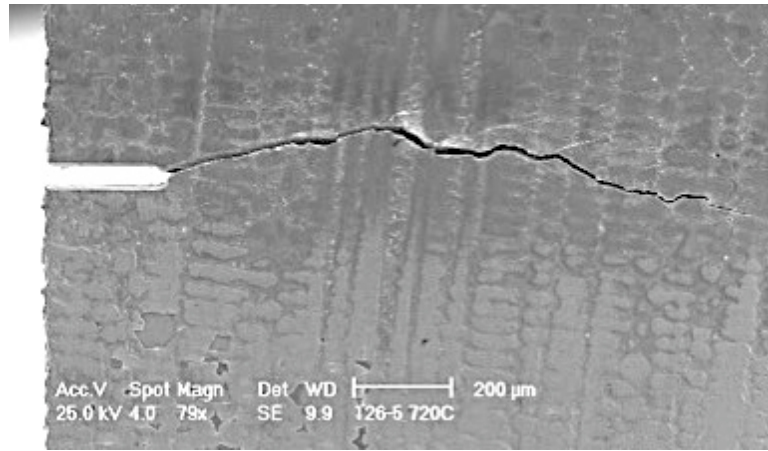
Figure 6.43 SEM image of LMC-10 sample, cracked at 720°C, $\Delta\sigma$ = 113 M
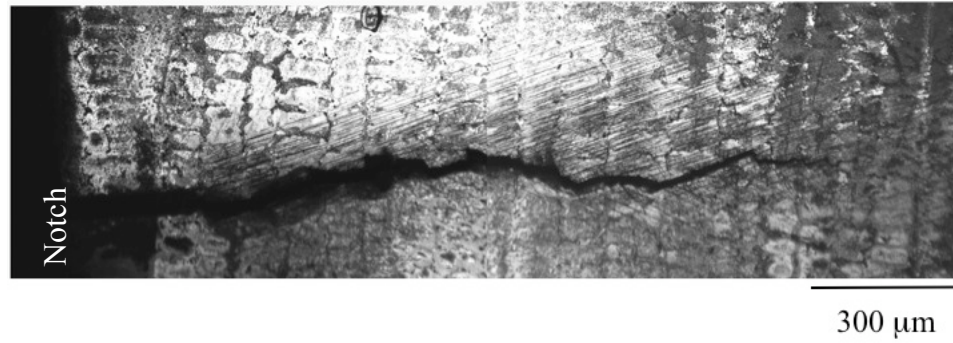
Figure 6.44 Optical micrograph of LMC-10 sample, cracked at 720°C, $\Delta\sigma$ = 113 MPa, displaying the intense slip bands near the (top-half) crack.
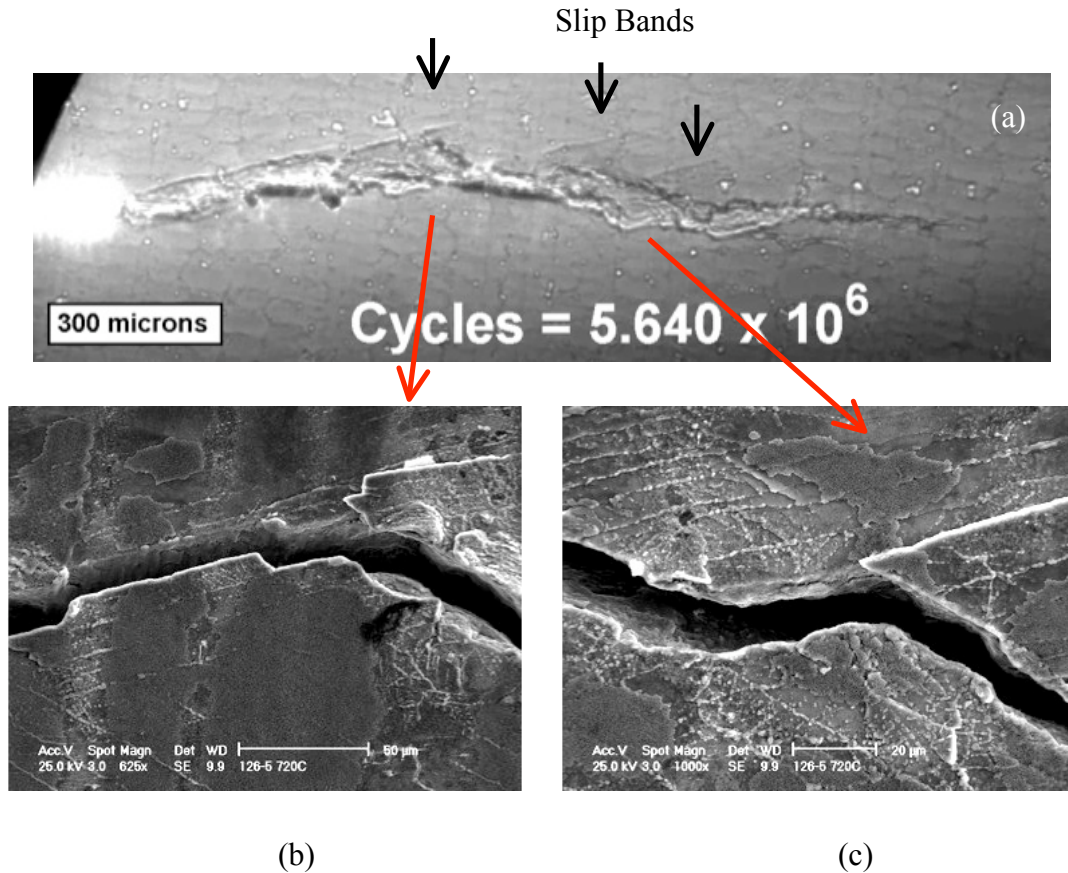
Figure 6.45 X-ray image and corresponding SEM image locations of cracked sample LMC-10 tested at 720ºC, $\Delta\sigma$ = 113 MPa .

When comparing the X-ray image to the SEM image, there appears to be sinusoidal crack path through the microstructure. At various "inflection" points of the wavy crack, deformation slip bands can be observed at various angles with respect to the notch plane. The lighter areas in Figure 6.45b and c represent the interdendritic area. Interestingly, these slip bands are clearly evident in the X-ray image, indicating that the deformation extended through a large proportion of the thickness of the sample.

High magnification SEM images in Figure 6.45 revealed the slip bands near the inflection points, where the bands intersect at certain areas. Various locations of the fracture surface are shown in Figure 6.46. The images reveal a rougher fracture surface than exhibited at lower temperatures. Figure 6.47 displays a tilted view of the fracture surface, giving an alternative view of the rough surface with respect to the crack direction.
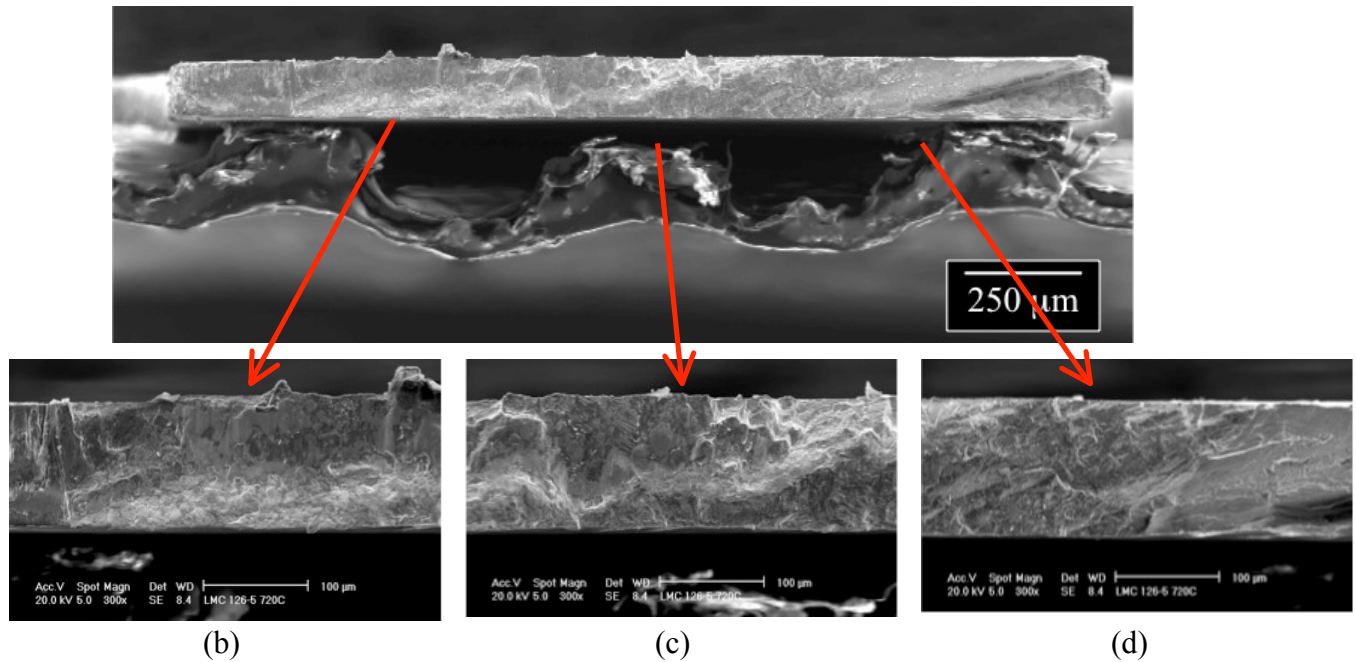
Figure 6.46 Fracture surface showing the [001] view of LMC-10 sample tested at 720°C, $\Delta\sigma$ = 113 MPa.
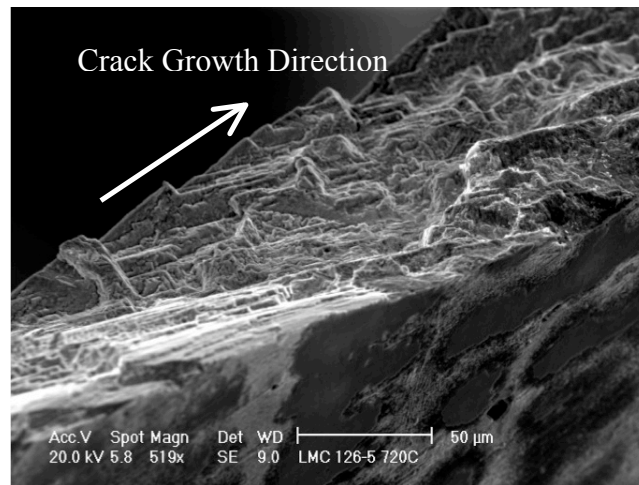
Figure 6.47 High magnification SEM image of the rough fracture surface produced during crack growth at 720°C in LMC-10 ($\Delta\sigma$ = 113 MPa).

6.9 Influence of Dendritic Structure on Crack Growth

Since it was of interest to investigate the influence of refinement in microstructure on the fatigue crack propagation behavior, fractographic analysis of the Bridgman cast samples is presented in this section at 538°C and 720°C to compare to the cracking behavior exhibited in the refined structures presented in the previous sections. Crystallographic crack growth was observed in the Bridgman cast sample at both

temperatures, with a smaller inclination angle from the notch in comparison to the ambient temperature cracks. Additional cycling steps, imposing larger stress intensities were required to initiate a crack in the Bridgman specimens in comparison to LMC. Variations in image contrast were observed in the coarse dendritically spaced microstructures at various regions before testing. As cracks grew through the microstructure, enhanced diffraction contrast arose due to the crack tip plasticity.

(a)

Darkened areas due to enhanced contrast →
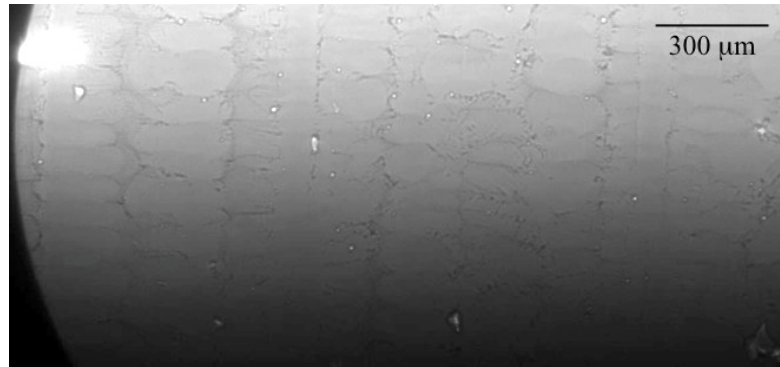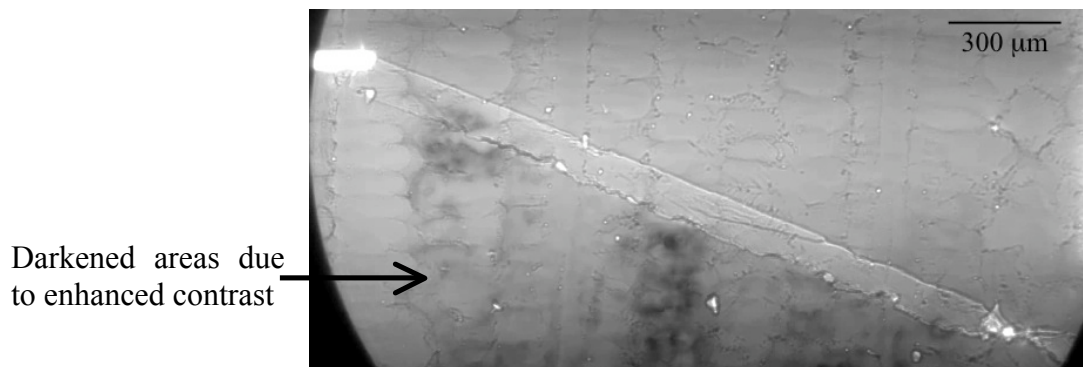
(b)

Figure 6.48 (a) A Bridgman solidified sample before fatigue testing. (b) Sample cracked at 538°C with the emergence of enhanced diffraction contrast variations within the dendritic structure.

The SEM image shown at 538°C for the Bridgman cast sample (Figure 6.50), reveals the smooth faceted crack. This same crack growth was exhibited in the refined structures at temperatures at 538°C. However, since a crystallographic mixed-mode cracking behavior was exhibited at higher temperatures in the coarser microstructure (Figure 6.49), as opposed to Mode I opening behavior in the refined structure ($T >$

174

580°C), there is apparently an influence of dendritic structure on the crack growth mode at higher temperatures.

300 microns   Cycles = 0.228 x 10⁶
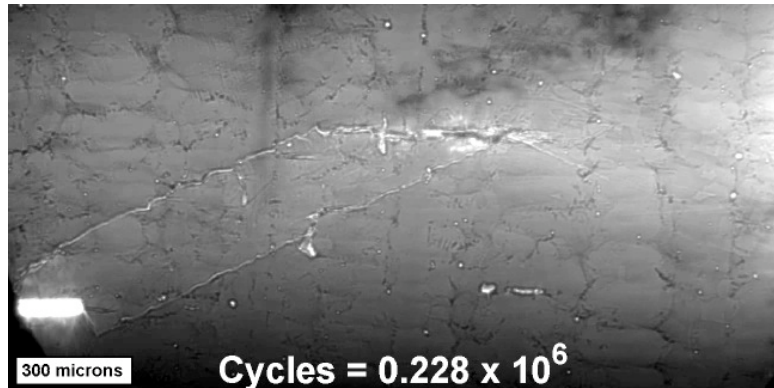
Figure 6.49 Crack produced at 720°C within a Bridgman solidified sample, displaying the crystallographic crack growth behavior.
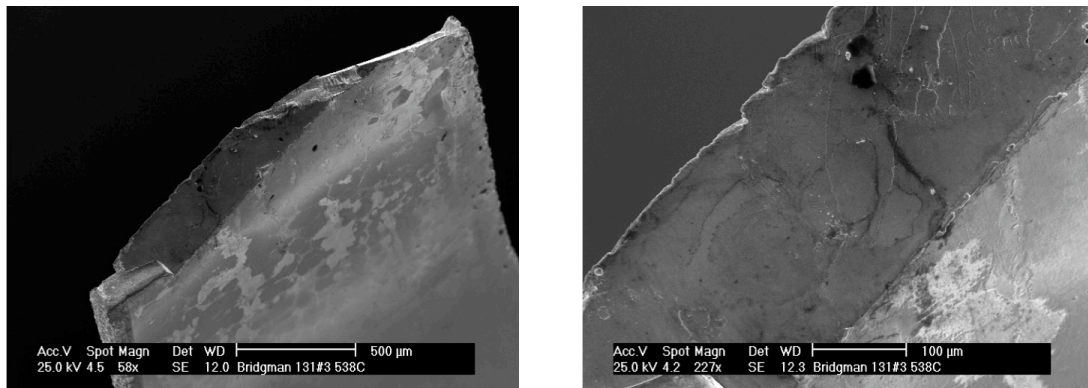
(a)   (b)

Figure 6.50 SEM image of a fracture surface of a Bridgman cast sample tested at 538°C. A higher magnified image is shown in (b).

The crack growth rates at 538°C for fine and coarse microstructures are shown in Figure 6.51 using an effective stress intensity factor, defined as

$$K_{eff} = \sqrt{K_I^2 + K_{II}^2}$$

[6.21]

Since the threshold stress intensity for René N5 has been recorded at 6.5 MPa-m$^{\frac{1}{2}}$, it is likely that cracking below this threshold would reside within the small crack growth regime. Therefore, it is expected that in the long crack growth (Paris) regime, there is no significant influence of microstructure scale on the fatigue crack growth rate at 538°C.

175
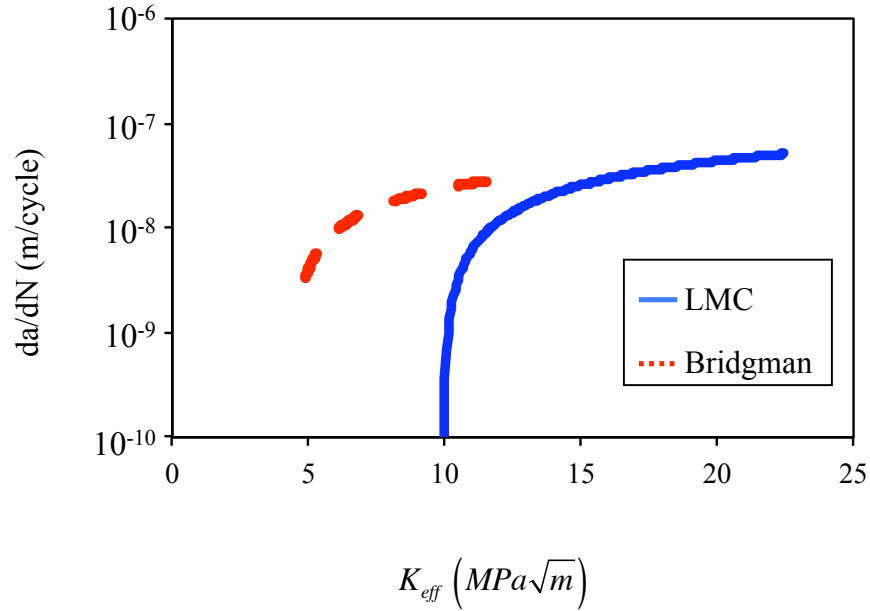
Figure 6.51 Stress intensity factor calculations for a LMC and Bridgman solidified sample fatigued at 538°C.

6.10   Influence of Stress Level

X-ray images displaying crack growth within a Bridgman solidified sample at 538°C are shown in Figure 6.52.   A crack emanated from the notch, growing perpendicular to the stress axis for a distance of 672 μm before arresting for a period of time at the interface of a dendritic/interdendritic region.

Changes in diffraction contrast can be observed with the growth of the crack with increasing cycles at 538°C (Figure 6.52). Diffraction contrast due to initial dislocation content in the interdendritic region is represented by the darkened region, which subsequently disappeared at the vicinity of the notch once the crack began propagating at a 45° inclination angle with respect to the tensile axis (Figure 6.52c). The location of the region which initially exhibited diffraction contrast is indicated with the arrow in the micrograph. This change is likely due to the generation of new dislocations during fatigue within the plastic zone. Contrastingly, changes in lattice distortion were not observed in the X-ray images in the finer dendritically spaced microstructure at 538°C. The size of the plastic zone, r_p, can be quantified using Equation 6.19:

176

$$r_p = \frac{1}{\pi}\left(\frac{\Delta K}{2\sigma_y}\right)^2 \qquad [6.22]$$

where ΔK is the stress intensity factor range and σ_y is the yield strength. With increases in ΔK, the plastic zone size should enlarge, encompassing more interdendritic area and generating increased dislocation generation. For the coarser microstructure presented in Figure 6.52, a larger strain amplitude was applied resulting in a higher stress intensity factor range than the finer scale microstructures (Table 6.1). The applied stress intensity recorded was 11.8 MPa-m$^{\frac{1}{2}}$, which is above the threshold stress intensity for René N5.[20] The high degree of diffraction contrast within the interdendritic region within the coarse microstructure is an important finding since these areas are sources of dislocations that will shear precipitates and eventually localize into slip bands.

(a)   (b)

(c)   (d)
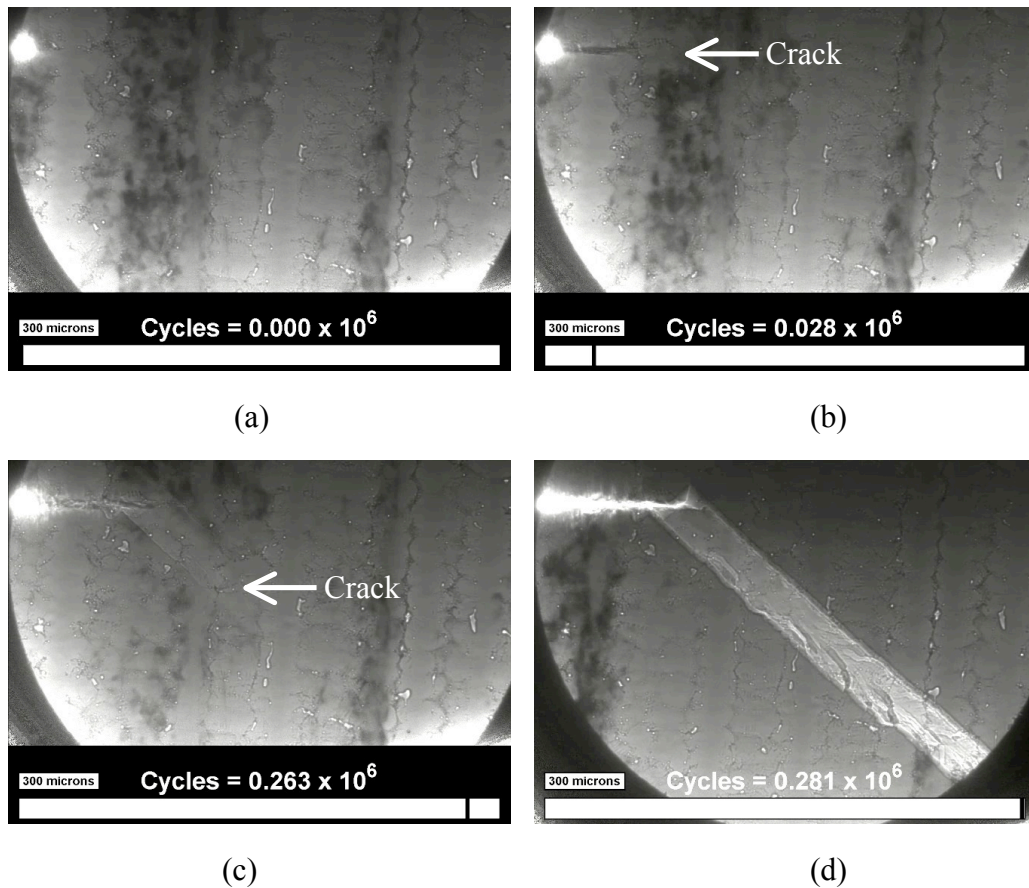
Figure 6.52 A Bridgman solidified sample subjected to fatigue cycling ($\Delta\sigma$ = 313 MPa) at 538°C.

Figure 6.53 presents the crack growth data for Figure 6.52, where faster cracking was observed during the inclined portion of the propagation. The substantial period of crack arrest after 1051 μm of crack growth can be observed in the plot with the flat portion of the curve.
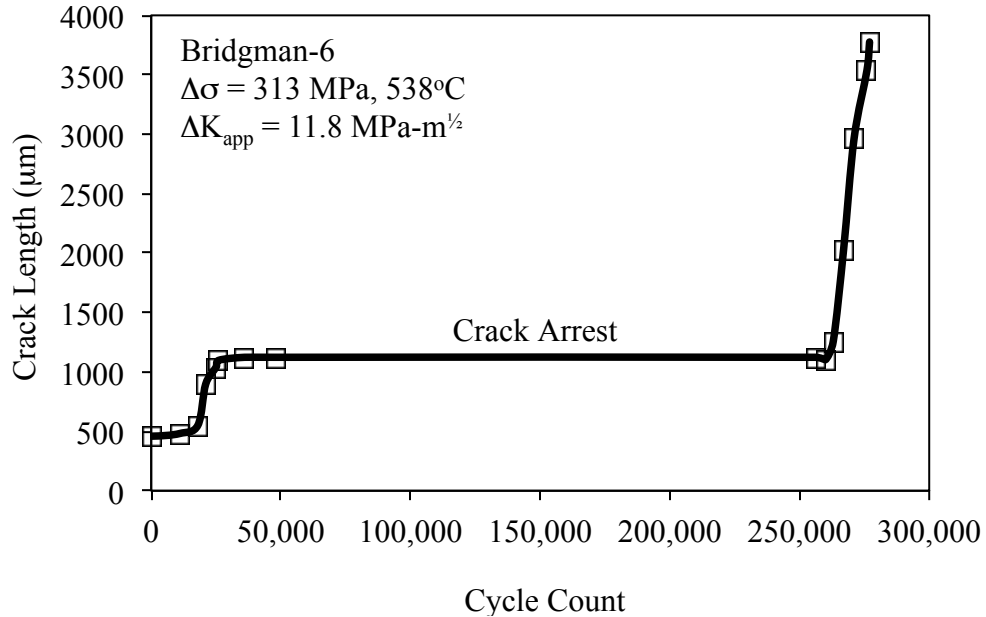
Figure 6.53 Crack growth with increasing cycles for a Bridgman cast sample tested at 538°C, $\Delta\sigma$ = 313 MPa.

SEM images revealed the Mode I opening crack that initiated from the notch, followed by the mixed mode cracking along a specific crystallographic plane. The free surface along the crack path was investigated, where various locations are magnified, Figure 6.54. In Figure 6.54c, the precipitates on the fracture surface appear as triangles, which is indicative of the shearing process that occurred along {111} planes. A magnified view of this shearing is shown in Figure 6.55. A discernible change in the texture on the fracture surface can be observed in Figure 6.56 at the transition region from Mode I to mixed mode.

(a)

500 μm

(b)

RN5 E

Notch

Acc.V Spot Magn Det WD 10 μ
20.0 kV 4.0 3200x SE 9.9 RN5 BM7 538C

(c)

100 μm

Acc.V Spot Magn Det WD 5 μm
20.0 kV 3.0 4000x SE 9.9 RN5 BM7 538C
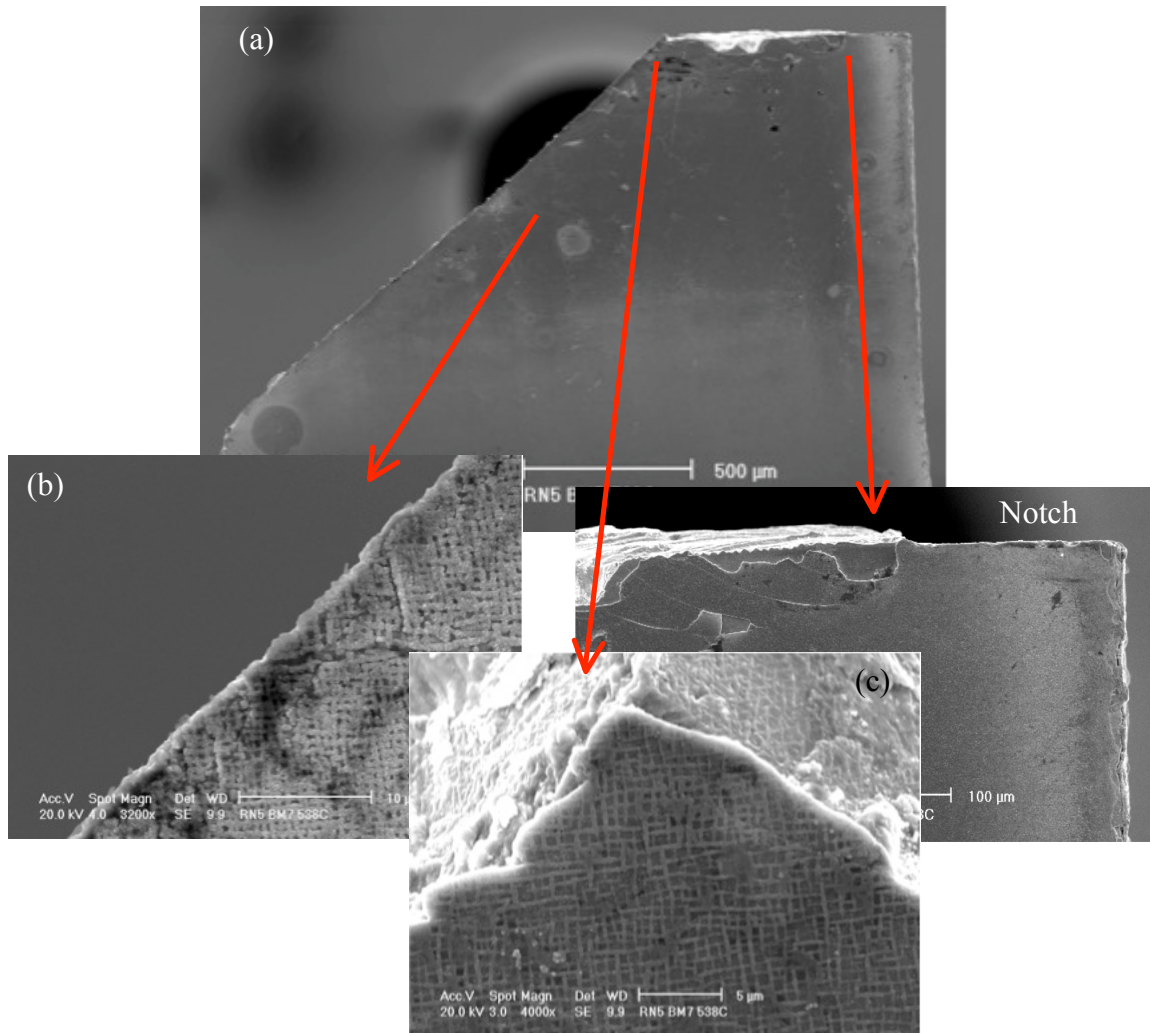
Figure 6.54 SEM images of the fracture surface of a Bridgman cast sample tested at 538°C, $\Delta\sigma$ = 313 MPa. The change in crack mode from Mode I to mixed-mode loading is emphasized in the highly magnified SEM image in (c).

Acc.V Spot Magn Det WD 2 μm
20.0 kV 3.0 8000x SE 9.9 RN5 BM7 538C
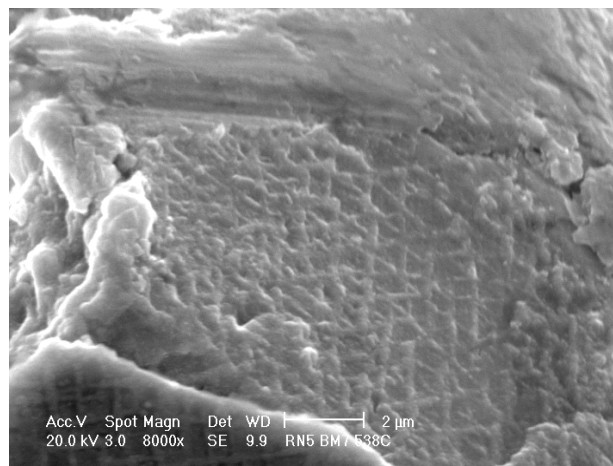
Figure 6.55 Magnified view of location shown in Figure 6.54c, displaying the result of shearing of precipitates during fatigue of sample Bridgman-6 at 538°C.

179

(a)   (b)

(c)
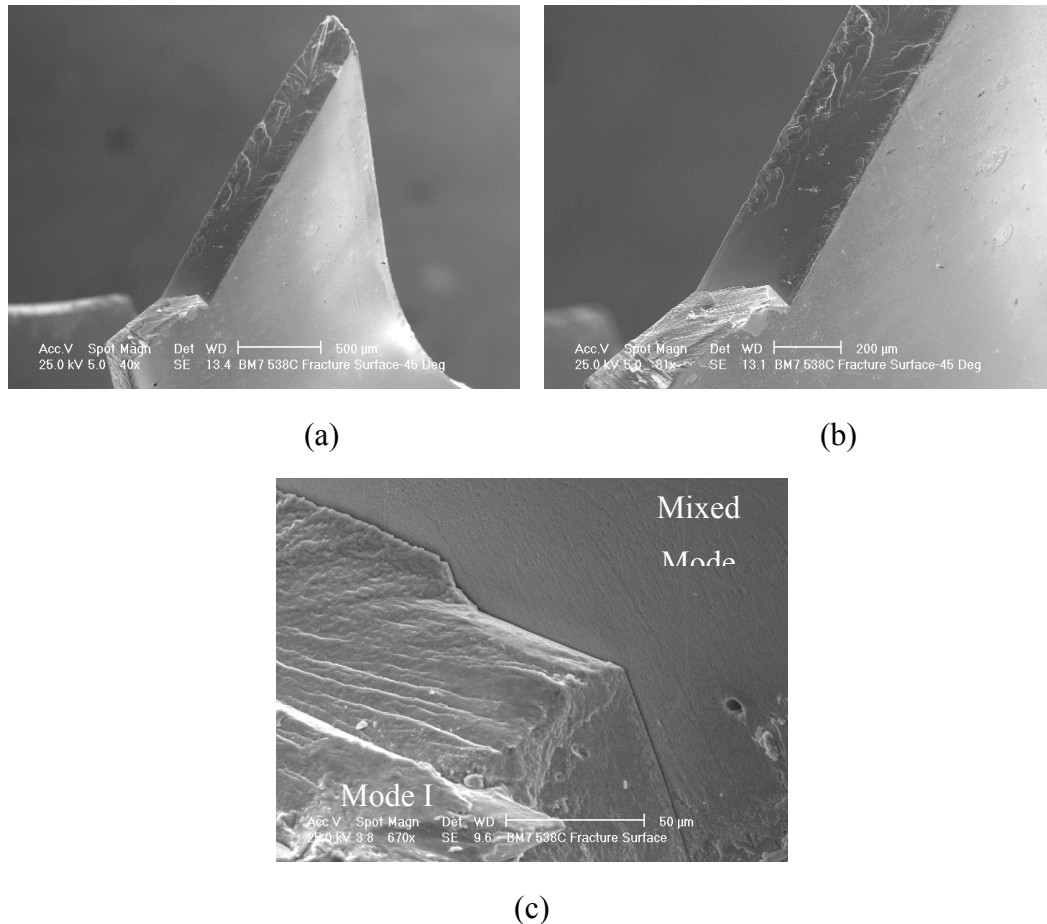
Figure 6.56 SEM images a Bridgman cast sample tested at 538$^{\text{o}}$C, $\Delta\sigma$ = 313 MPa. A notable difference in the surface corresponding to Mode I opening and mixed-mode conditions is emphasized in (c), where the low magnification images of this region are shown in (a) and (b).

6.11   Summary

High brilliance X-ray radiation studies were successfully performed at high temperatures on thin-sheet single-crystal René N5 specimens with fine and coarse microstructure scales. Three-dimensional projections of cracks allowed for observations of unique features unattainable from conventional microscopy techniques. Absorption contrast, phase contrast, diffraction contrast and thickness variations contributed to the ability to view the interaction of the cracks with the microstructure features. Differences in diffraction contrast between the interdendritic and dendritic regions were observed during fatigue cracking within the coarser microstructure. This variation in image contrast was not readily observed in the finer scaled structure during fatigue.

180

The mode of crack growth in single crystal René N5 does not exhibit a strong frequency effect at 538°C for bulk and thin-sheet specimens. Cracking along {111}-type crystallographic crack planes was present at f = 0.5 and 20 kHz. The similar crack growth behavior in thin-sheet and bulk fatigue specimens allowed for direct comparison of the mixed-mode crack growth rates for the coarse and finer scale microstructures.

Mixed-mode cracking was prevalent at temperatures below 538°C for all microstructure scales. Inclination angles of the cracks with respect to the notch decreased with increasing temperature, which required mixed-mode stress intensity solutions. It is suitable to apply Mode I stress intensity solutions to cracks that propagate normal to the stress axis. The change in crack growth mode at this temperature was attributed to the effect crack-tip oxidation. Transitions in crystal plane crack path were observed at all temperatures tested, owing to high resolved shear stress intensities on multiple octahedral planes.

The influence of refinement in dendritic spacings is evident at 720°C, where Mode I cracking predominates, and mixed-mode crack growth exists in the coarsely spaced microstructures. It can now be assumed that similar mixed-mode crack growth rates were exhibited for the coarse and fine microstructures tested at 538°C in Chapter 5. The data collected in this chapter also suggests that a fatigue life model must incorporate the change in crack growth mode at higher temperatures for single crystal fatigue. This result underscores the importance of understanding the basis mechanisms of fracture and fatigue when establishing design margins and generating a fatigue property model.

[1]   N. Husseini, D.P. Kumah, J.Z. Yi, C.J. Torbet, D.A. Arms, E.M. Dufresne, T.M. Pollock, J.W. Jones, and R. Clarke: *Acta Mater.*, 2008, 56, pp. 4715-4723.

[2]   L. Liu, C.J. Torbet, N.S. Husseini, R. Clarke, T.M. Pollock, and J.W. Jones: *Acta Metall.*, 2010 submitted.

[3]   L. Liu, N.S Husseini, C.J. Torbet, D.P. Kumah, R. Clarke, T.M. Pollock, and J.W. Jones: *J. of Eng. Mat. Tech.*, 2008, 130, pp. 021008-1-6.

[4]   R. Naik, D.P. DeLuca, and D.M. Shah: *J. Eng. Gas. Turb. Power*, 2004, 126, pp. 391-400.

[5]   K.S. Chan and T. A Cruse: *Eng. Fract. Mech.*, 1986, 23, pp. 863-874.

[6]   G.P. Zhang and Z.G. Wang: *Fat. Fract. Engng. Mater. Struct.*, 1997, 6, pp. 883-894.

[7]   S.G. Lekhnitskii: *Theory of Elasticity of an Anisotropic Elastic Body*, Holden-Day, Oakland, CA, 1963.

[8]   T. Tinga: *Engng. Fract. Mech.*, 2006, 73, pp. 1679-1692.

[9]   D.J. Duquette and M. Gell: *Metall. Trans.,* 1971, 2, pp. 1325-31.

[10]   S. Timoshenko and J.N. Goodier: Theory of Elasticity, 2nd Edition, New York, McGraw-Hill, 1951.

[11]   P. Lukas, L. Kunz, and M. Svoboda: *Int. J. Fatigue*, 2005, 27, pp. 1535-1540.

[12]   R.J. Morrissey and P.J. Golden: *Int. J. Fat.*, 2007, 29, pp. 2079-2084.

[13]   D.W. MacLachlan and D.W. Knowles: *Fat. Fract. Eng. Mater. Struct.*, 2001, 24, pp. 503-521.

[14]   D.J. Duquette, M. Gell and J.W. Piteo: *Metall. Trans.*, 1970, 1, pp. 3107-3115.

[15]   S.E. Cunningham, D.P. DeLuca, and F.K. Haake: Report # WL-TR-94-4089, 1994.

[16]   S.D. Antolovich and N. Jayaraman: in *Proc. of the 27th Sagamore Army Materials Research Conference,* J.J. Burke and V. Weiss, eds., 1983, pp. 119-144.

[17]   J.J. McGowan and H.W. Liu: *in Proc. of the 27th Sagamore Army Materials Research Conference*, J.J. Burke and V. Weiss, eds., 1983, pp. 377-390.

[18]   J. Telesman and L.J. Ghosn: *ASME J. Eng. Gas Turbines and Power*, 1996, vol. 118, pp. 399-405.

[19]   P.A.S. Reed and M.D. Miller: in *Superalloys 2008*, R.C. Reed, K.A. Green, P. Caron, T. Gabb, M.G. Fahrmann, E. Huron, and S.A. Woodward, eds., Seven Springs, PA, TMS, 2008, pp. 527-533.

[20]   C. Yablinsky, *PhD Thesis*, The Ohio State University, 2005.

Chapter 7

**MICROSTRUCTURE-BASED FATIGUE MODELING OF SINGLE CRYSTAL
SUPERALLOYS**

The traditional approach of developing single crystal alloys involves trial-and-error methodologies based on modifications of existing alloys, followed by extensive experimental programs to evaluate material modifications, develop processing parameters and certify performance. Average as well as minimum properties and statistical variability must be evaluated. The process is costly and requires a development cycle for materials that is much longer than the design cycle for components. The motivation of this chapter is to establish a connection between processing, resulting microstructure and fatigue life in order to provide a mechanistically sound model that will aid in alloy and process development.

This chapter will address the micromechanical model presented in Chapter 5, which can be used to predict the low cycle fatigue life (LCF) of the René N5 and modified Hi-Ta alloys at 538°C ($R = 0$) using a microstructure-based approach. A detailed description of the parameters integrated into this micromechanical model will be given, and the important role of solidification-induced porosity will be addressed. The most critical microstructural features that influence the crack initiation stage will be discussed in order to present a microstructure-based crack-initiation model applicable to single crystal superalloys. A deterministic crack-initiation model has been developed to predict the initiation life and to combine to the propagation life. Lastly, it will be shown how the developed micromechanical model provides a vital connection between cooling rate ($G{\times}V$) and fatigue life.

7.1 Modeling Fatigue Crack Initiation and Growth

It has been determined that the strain-controlled LCF life at 538°C for single crystal René N5 is strongly dependent on the microstructure scale and is predominately limited by solidification-induced porosity. Changes in alloy chemistry that provide larger pores will ultimately shorten the life, regardless of possible strengthening benefits. In this section, two modeling approaches for predicting the fatigue life are considered. The first is a fracture mechanics-based approach. Beyond this, an initiation model that supports the fracture mechanics correlations is developed. A flaw size dependent model is necessary due to the wide range in fatigue initiating pore sizes, the pore-pore stress-concentrating interactions, and the stress dependence on the crack initiation life. Additionally, the impact of crack initiation versus crack growth on the mechanical model will be discussed. A comparison to a typical fracture mechanics approach to model the fatigue life of metallic materials will be presented.

7.2 Stress Intensity at the Initiation Site

Fractographic analysis and stress intensities associated with pores within the solidified structure were shown in Chapter 5 using an initial stress intensity factor range, ΔK, calculated using the following formulae:[1]

$$\Delta K = 0.65 \Delta \sigma \sqrt{\pi \sqrt{A_{defect}}}$$ [7.1]

for surface crack initiation,

$$\Delta K = 0.5 \Delta \sigma \sqrt{\pi \sqrt{A_{defect}}}$$ [7.2]

for internal crack initiation,

where $\Delta \sigma$ is the stress range applied and A_{defect} is the projected area (on a plane $\perp$ to the σ-axis) of the defect measured from the fracture surface. Modification of these equations to reflect an initial Mode II stress intensity factor, K_{II}, is shown as

$$K_{II} = Y \tau \sqrt{\pi \sqrt{A_{defect}}}$$ [7.3]

184

Previous research has shown that the stress intensity is influenced by pore shape by less than 10%.[2] Other studies have also indicated that it is the size of defects, rather than their shape, that influences crack initiation,[3-5] and, therefore, pore shape is not considered in subsequent analyses. Figure 7.1 displays the relationship between stress intensities and the number of cycles to failure, as shown in Chapter 5. For the four alloy/process variants analyzed, the lives decreased with an increase in initial stress intensity.
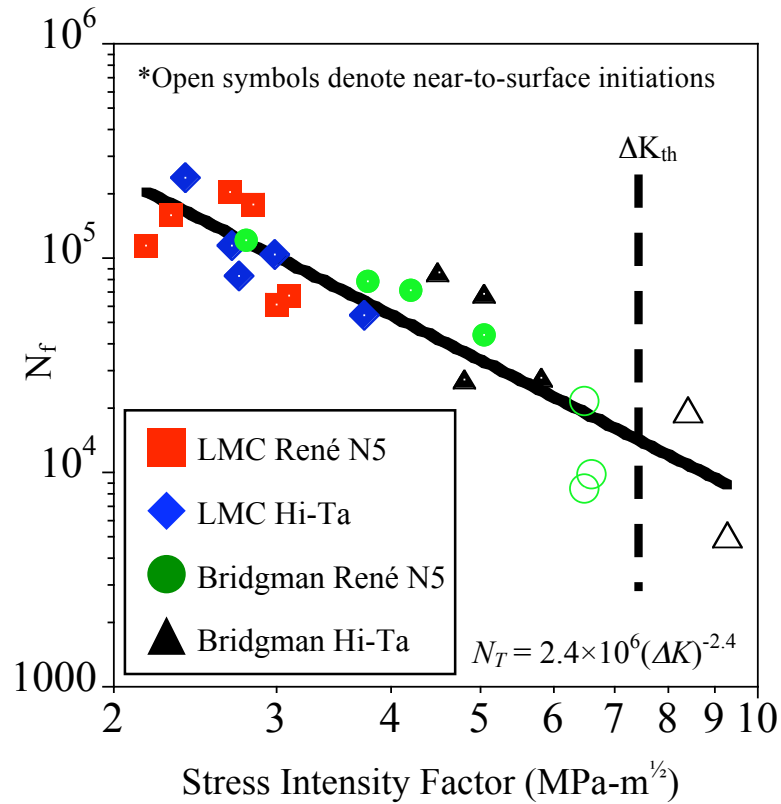
Figure 7.1 Stress intensities plotted for LMC and Bridgman solidified René N5 and modified René N5 alloys from LCF testing at 538°C, $R = 0$.

Smaller stress intensities were associated with the pores with the LMC refined microstructure. In the LMC-processed materials, the stress intensities were far below the ΔK_{th} of René N5, [6] represented by a dashed line in Figure 7.1. Open symbols represent near-to-surface initiations from pores. It should be noted that these initiations produced shorter lives in comparison to internal fractures. Interestingly, near-to-surface initiations

occurred at intensity values near or greater than the threshold. The data presented in Figure 7.1 can be represented by the following power-law relationship:

$$N_T = 2.4 \times 10^6 \left(\Delta K \right)^{-2.4} \qquad [7.4]$$

Knowing that the total life, N_T, is composed of the crack initiation (N_i) and propagation (N_p) stages as

$$N_T = N_i + N_p \qquad [7.5]$$

where using the Paris-Erdogen power law[7-9] to estimate N_p is given as

$$\frac{da}{dN} = C \left(\Delta K \right)^m \qquad [7.6]$$

Integration of Equation 7.6 utilizing constants C and m as 10^{-11} MPa$^{-3.6}$-m$^{-1.81}$ and 3.6,[6] respectively, gives

$$N_f = \frac{1}{C \Delta \sigma^m Y^m \pi^{m/2}} \left[\frac{2a_0^{1-m/2} - 2a_f^{1-m/2}}{m-2} \right] \qquad [7.7]$$

where Y represents the flaw size geometry and a_o and a_f are the initial and final crack sizes, respectively. The crack growth life is sensitive to the initial flaw size a_0, but also depends on microstructure, which can alter intrinsic material properties.[10] Despite the larger range in initial flaw sizes (Table 5.3), representative of crack-initiating pores, significant underestimations of the total lives of the specimens were predicted when only using the Paris-Erdogen law for the alloy/process variants, which has also been noted elsewhere.[8] From the low stress intensity values shown in Figure 7.1, it is likely that majority of the life is consumed during the crack initiation stage. Under that assumption, the total life equation can be expressed as

$$2.4 \times 10^6 \left(\Delta K \right)^{-2.4} = N_i + \frac{1}{C \Delta \sigma^m Y^m \pi^{m/2}} \left[\frac{2a_0^{1-m/2} - 2a_f^{1-m/2}}{m-2} \right] \qquad [7.8]$$

It is clear that a comprehensive crack initiation model that estimates the majority of the fatigue life of single crystal superalloys is necessary. The stress dependence from the crack growth stage and the micromechanical model within ΔK indicates that a crack initiation model that considers stress dependence and flaw size should be employed here.

7.3   Microstructure-Based Fatigue Crack Initiation Model

Generally, fatigue life prediction models for metallic materials regard pores as existing microcracks and assume that crack initiation life is negligible compared to the total life. Probabilistic models are typically applied to estimate the fatigue life from a given distribution of potential crack initiating pore sizes. These models revolve around the notion that the nucleation of cracks depends on the defect distribution and the heterogeneity in the surrounding material. A crack initiation model will be presented in the following sections to predict the fatigue crack initiation life from microstructure features. The model of Tanaka and Mura considers the accumulation of dislocation dipoles generated by irreversible slip in slip bands as the rate-dependent damage process lead to crack initiation.[11,13] Microscopy techniques utilized in the literature to measure slip band spacings and slip height displacement are considered. It should be noted that the model developed by Tanaka and Mura[11] has yet to be applied to single crystal superalloys with large pore initiating defects.

7.3.1   Slip Band Models

The initiation process near pores occurs due to the stress concentration, which locally enhances the dislocation processes.[12] A magnified view of surface intrusions and extrusions near a crack initiating pore site within a LMC solidified sample is shown in Figure 7.2. This surface relief can be attributed to the reversible and irreversible dislocation motion along slip planes, which results in the gradual formation of surface slip markings. It can be deduced from Figure 7.2 and other descriptions in the literature[5] that the crack initiation process from pores was preceded by irreversible dislocation slip processes. This surface topography causing a geometrical stress concentration and the specific configuration of the dislocation structure—preventing local stress relaxation—is the likely process for crack initiation.
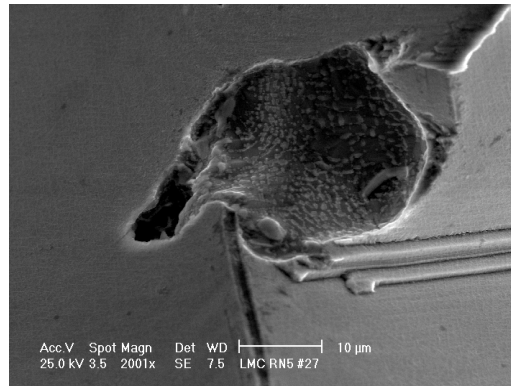
Figure 7.2 Magnified view of the surface relief near a crack initiation site within a LMC solidified sample tested at $\Delta\sigma = 380$ MPa, $T = 538^{\circ}$C.

Following an approach developed by Tanaka and co-workers,[11,13-15] fatigue crack initiation has been modeled by considering the accumulation of dislocation dipoles generated on slip bands near inclusions during fatigue cycling, Figure 7.3. For simplicity, only edge type dislocations are considered. Venkataraman *et al*.[15] has extended the model developed by Mura and Tanaka[11] to develop an expression for optimum slip band spacing in polycrystalline materials, which can be influenced by temperature, strain amplitude and environment. It is of particular interest to understand how pore size, microstructure scale and material strength from the René N5 and Ta-modified alloy impacts slip band formation during the LCF process. The upcoming sections will show how relevant features from slip band theories can be used to predict the crack initiation life of these single crystals.
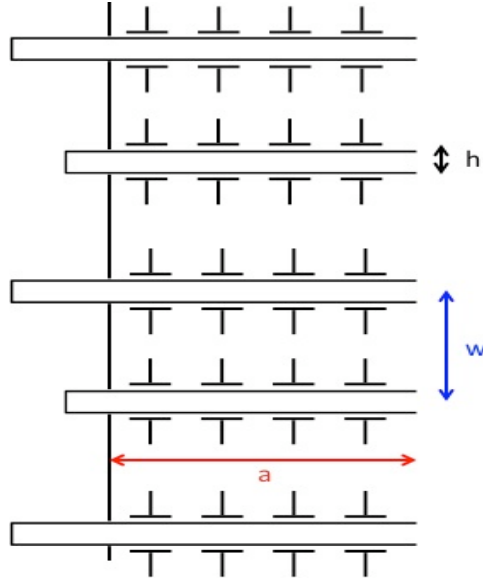
Figure 7.3 Schematic of *m* slip bands with accumulated dislocation dipoles and associated extruded material. Shown in Venkataraman *et al.*[15]

In a series of three articles, Tanaka and Mura proposed dislocation models for initiation at slip bands, inclusions and notches applicable to polycrystalline structural alloys such as steels, Al-, Ti-, TiAl-, and Ni-based alloys.[11,13,16] For crack initiation along a slip band, the dislocation-dipole accumulation model is given by[11]

$$(\Delta\tau - 2k)(N_i)^{\frac{1}{2}} = \left[\frac{8GW_s}{\pi d}\right]^{\frac{1}{2}}$$
[7.9]

where $\Delta\tau$ is the shear-stress range, k is the frictional stress necessary to move dislocations, G is the shear modulus, d is the grain size, and W_s is the specific fracture energy. The fracture energy can be expressed as[11]

$$W_s = \frac{\Delta K_{th}^2}{2E}$$
[7.10]

where E is the Young's modulus. It can be assumed that higher thresholds will increase the fracture energy and produce longer lives. A simplified form of this model can be given as follows: [17]

189

$$N_i = \frac{AW_s}{(\Delta\tau - 2k)^2} \qquad [7.11]$$

The variable A is a function that depends on the material properties and the type of initial defects as

$$A = \qquad [7.12]$$

$$\begin{cases} \dfrac{4G}{\pi(1-v)l} & \text{crack initiation along slip bands} \\[2em] \dfrac{4G(G+G_i)h^2}{G_i(h+l)^2 a_i} & \text{crack initiation along the interface of an inclusion} \end{cases}$$

where G is the bulk shear modulus, G_i is the shear modulus of an inclusion, l is the semi-length of a slip band, h is the semi-mirror length of an elliptical slip band area, and v is the Poisson's ratio. For the René N5 alloys, G was taken as 120 GPa. Assumptions for the model include:[11]

1. The inclusion (pore) size is representative of a crack initiation size

2. The frictional stress, k, can be regarded as half the fatigue limit.

Modification of the function, A, to represent a fatigue initiating pore size, in terms of radius, a_0, gives

$$A = \frac{4Gh^2}{(h+l)^2 a_0} \qquad [7.13]$$

For continued plastic deformation under the condition of complete irreversibility, equilibrium of stresses on the slip planes requires the following:[11]

1. The resolved shear stress range $\Delta\tau$ must overcome the effective frictional resistance $2k$ to generate an additional number of dislocations on the two layers with each fatigue cycle.

2. Additional dislocations must have an effective dislocation stress equal to ($\Delta\tau$ – $2k$).

Therefore, the total dislocation stress on a layer of pile-up after n fatigue cycles must equate to $n(\Delta\tau - 2k)$. However, this approach has been found to lead to an overestimation of the dislocation density since the majority of slip is reversible,[18] which requires further investigation of slip band formation using more advanced microscopy techniques, such as transmission electron microscopy (TEM) or atomic force microscopy (AFM).

Using the Von Mises yield criterion for uniaxial loading, the relationship between the shear stress amplitude and the applied stress range is:

$$\Delta\tau = \frac{\sqrt{2}}{3}\Delta\sigma \quad .$$
[7.14]

Table 7.1 gives the estimations of the initiation lives using Equation 7.11 and 7.13. Values of h, l and a_0 were determined from fractographic analysis of failed samples using SEM. The fatigue limit was estimated at 310 MPa for R = 0.[19] Only samples where slip band measurements could clearly be obtained are displayed. For nearby pores, l and h measurements were taken only near the largest sized pore surface. Examples of samples with clearly visible slip bands near the pore surfaces are shown in Figure 7.4 and 7.5. The large discrepancies between the predicted and actual number of cycles is likely due to the accuracy in the surface offset measurements. Profilometry may be an alternative method to obtaining more accurate measurements of the topographic features.

Table 7.1 Estimations of N_i using a crack initiation-based slip band model for René N5 alloys.

Alloy	Process	h (μm)	l (μm)	σ_{ALT} (MPa)	Pore Radius (μm)	Predicted N_i (cycles)	N_f (cycles)
René N5	LMC	1.0	10.0	448	14.7	90,446	114,934
René N5	LMC	6.8	20.0	448	22.6	460,402	157,764
René N5	LMC	1.0	10.0	413	25.6	83,881	204,131
Hi-Ta	LMC	3.0	8.0	482	20.6	428,354	82,532
René N5	Bridgman	1.0	2.1	482	73.4	42,052	44,180
René N5	Bridgman	0.5	2.5	413	59.6	52,020	70,933
Hi-Ta	Bridgman	4.1	7.6	448	70.0	87,838	27,650
Hi-Ta	Bridgman	1.3	5.6	380	75.7	85,403	86,216
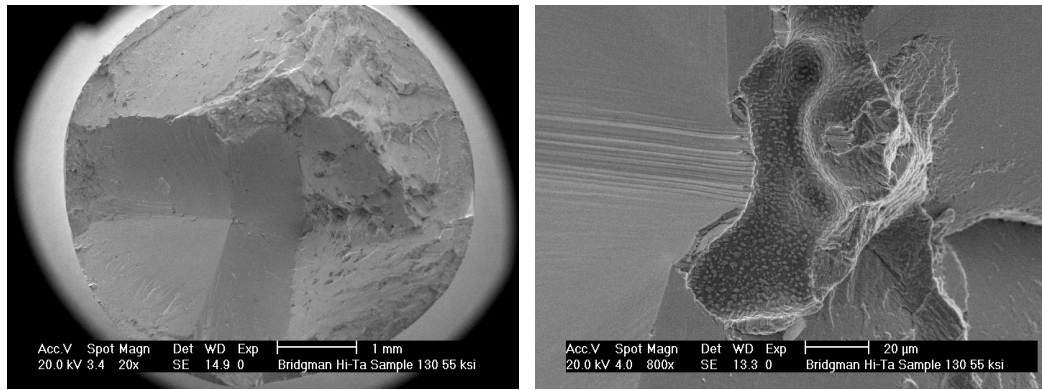
(a)   (b)

Figure 7.4 (a) Fracture surface of a Bridgman solidified specimen tested at 448 MPa producing an internal initiation. (b) Intense slip bands near a crack-initiating pore. Estimated initiation life = 83,083 cycles.
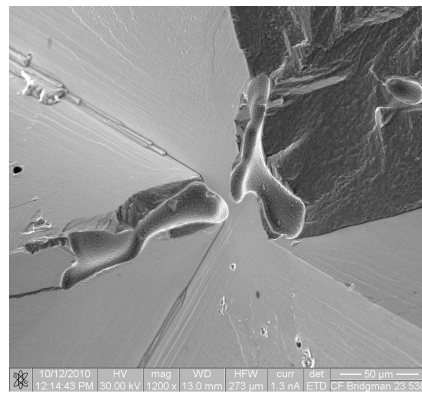
Figure 7.5 Crack initiation site within a Bridgman solidified sample owing to a 96% initiation life, N_i = 42,052 cycles.

Equation 7.11 is sensitive to stress level and pore size, with a dependence of:

$$N_i = \frac{A'}{a_0 \Delta \sigma^2}$$ [7.15]

where A' is representative of the constants in Equation 7.11. Using Equation 7.8 and 7.11, the total life of the alloy can now be presented as

$$N_T = \frac{4Gh^2}{(h+l)^2 a_0} \left(\frac{W_s}{(\Delta \tau - 2k)^2} \right) + \frac{1}{C\Delta\sigma^m Y^m \pi^{m/2}} \left[\frac{2a_0^{1-m/2} - 2a_f^{1-m/2}}{m-2} \right]$$ [7.16]

and since

$$N_T = \frac{2.4 \times 10^6}{\left(Y\Delta\sigma \sqrt{\pi \sqrt{A_{defect}}} \right)^{2.4}} \approx \frac{C'}{a_0^{1.2} \Delta\sigma^{2.4}}$$ [7.17]

where C' represents the constants. The total fatigue life can be expressed as

$$N_T \approx \frac{A'}{a_0 \Delta\sigma^2} + \frac{B'}{a_0^{0.81} \Delta\sigma^{3.6}}$$ [7.18]

Equations 7.16-7.18 summarize the stress and pore size dependence on the total fatigue life, which gives an explanation to the effectiveness of the power law relationship (Equation 7.4) at modeling the life of both alloys and processes. The initiation stage is more strongly dependent on pore size, with smaller pores producing longer lives for a given stress level. The crack initiation expression is also sensitive to the frictional stress required to move dislocations (Equation 7.11), which may change with alloy chemistry. The crack growth stage relies on the stress level, which can dramatically change with the variation in the Paris exponent, m. Additionally, the exponent, m, can change with stress ratio, alloy composition,[20] and temperature.[6] However, it is expected that only a slight variation in m will be present for the René N5 and Ta-modified alloys.

The micromechanical model should be useful for a various alloys and processes to predict the fatigue life of a single crystal if a range of pore size within the material is known. The correlation should break down when the defect sizes are on the same order

of magnitude of the microstructural features, such as the dendritic spacings (>150 μm),[4] causing immediate crack initiation.[26] Also, cycling at σ_{ALT} values above the yield stress will also cause the correlation to break down. The next section will demonstrate the usefulness of the fracture mechanics-based micromechanical model to connecting processing conditions to the fatigue life.

7.4   Connecting Fatigue Properties to Microstructure

Figure 7.6 displays the LCF results at 538°C (R = 0) in terms of microstructure scale showing λ_1 = 150 μm (LMC) and 360 μm (Bridgman). A similar improvement in fatigue life (T = 800°C) with refinement in dendritic spacings was shown (Figure 7.7)[21] by evaluating various solidification conditions to grow PWA 1483 single-crystal samples with average PDAS values of 250 μm, 400 μm and 600 μm. Large pores were found to be responsible for the fatigue failures, initiating cracks along octahedral crystallographic planes at this elevated temperature with R = -1. The longest fatigue life was obtained for the most refined dendrite structure (PDAS = 250 μm), similar to trend found in this study. It is more than likely that the pore location and stress level had a substantial effect on the life of the alloy (Figure 7.9), thus the micromechanical model presented in Section 7.1 would be applicable for this 800°C data. Unfortunately, the conditions employed for testing PWA 1483 varied from what was used in this study, so the model would need to be refined to consider varying R ratios .

The fatigue tests at 538°C and 800°C are presented to emphasize the substantial benefit of utilizing a higher thermal gradient casting method to augment the fatigue life over a wide range of dendrite arm-spacings, in comparison to improvement through the addition of the refractory alloying element, Ta. Figures 5.1 and 5.2 demonstrated that an increase in Ta to the René N5 composition was effective increasing the strength of the alloy, but also resulted in a fatigue debit, due to larger pores.

194
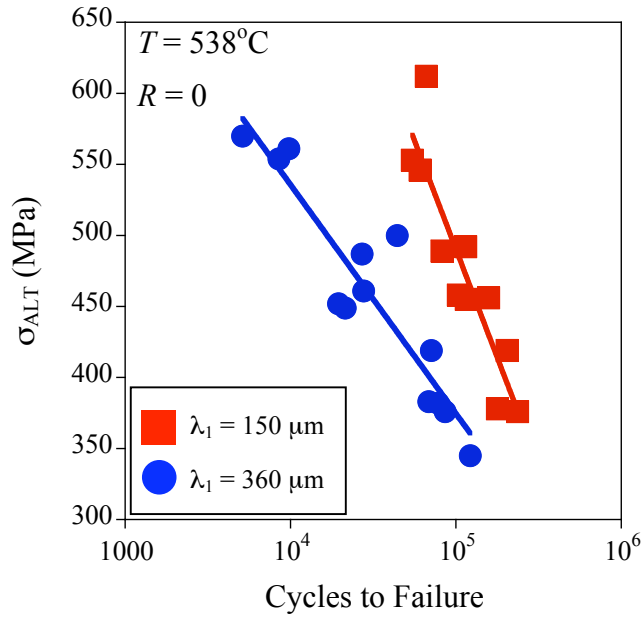
Figure 7.6 Fatigue life for René N5 at 538°C (*R* = 0) for two average primary dendrite arm spacings, 150 μm and 360 μm.
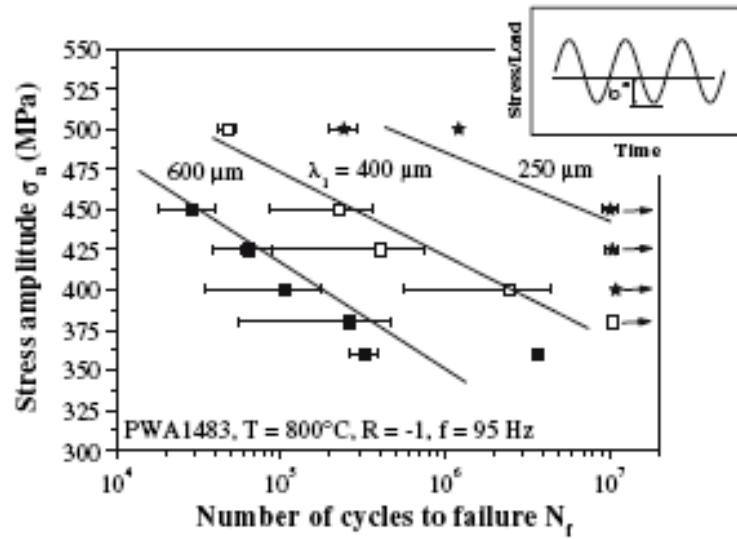
Figure 7.7 Fatigue life for PWA 1483 at 800°C (*R* = -1) for various primary dendritic scales, 250 μm, 400 μm and 600 μm.[21]
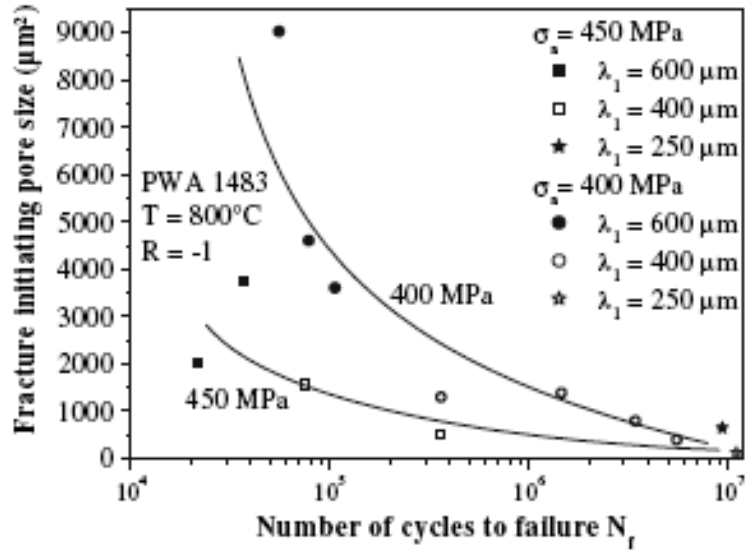
Figure 7.8 Lifetimes for various fracture initiating pore sizes within single-crystal PWA 1483 solidified with various withdrawal rates to produce average PDAS values of 250 μm, 400 μm and 600 μm.[21]
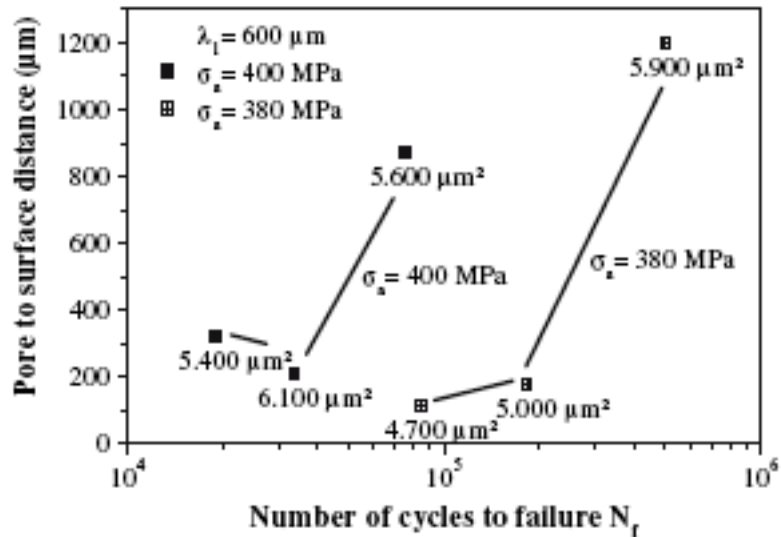
Figure 7.9 Influence of pore to surface distance on the lifetime for PWA 1483 single crystal superalloy at 800°C, _R_ = -1. [21]

Figure 7.10 demonstrates the ability of the LMC process to refine the primary dendrite arm spacings, with a limit to PDAS structure refinement apparent at a solidification rate of 12.7 mm/min. However, due to the strong pore size scaling with the SDAS, the most important factor in achieving improved fatigue life is defect size reduction, not necessarily PDAS refinement since it is heavily dependent on dendrite

196

growth history and interface curvature.[22-24] Therefore, it is suggested that a processing-property model identify the connection between processing and pore size.
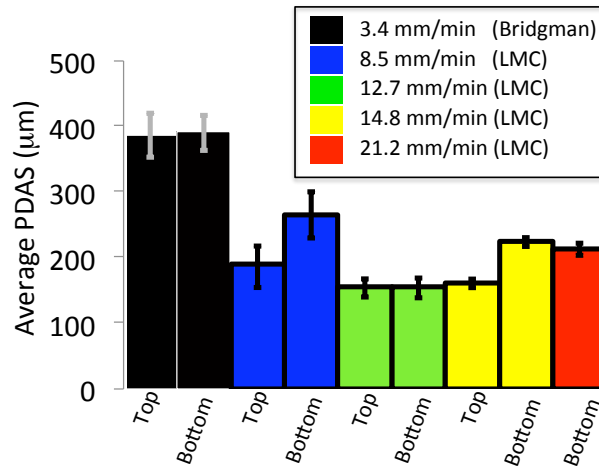
Figure 7.10 Average PDAS for various withdrawal rates using the Bridgman and LMC processes to grow single crystal René N5 bars.
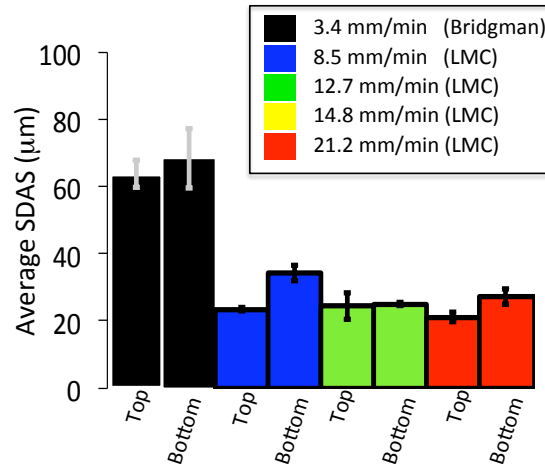
Figure 7.11 Average SDAS for various withdrawal rates using the Bridgman and LMC processes to grow single crystal René N5 bars.

<center>(a)   (b)   (c)</center>
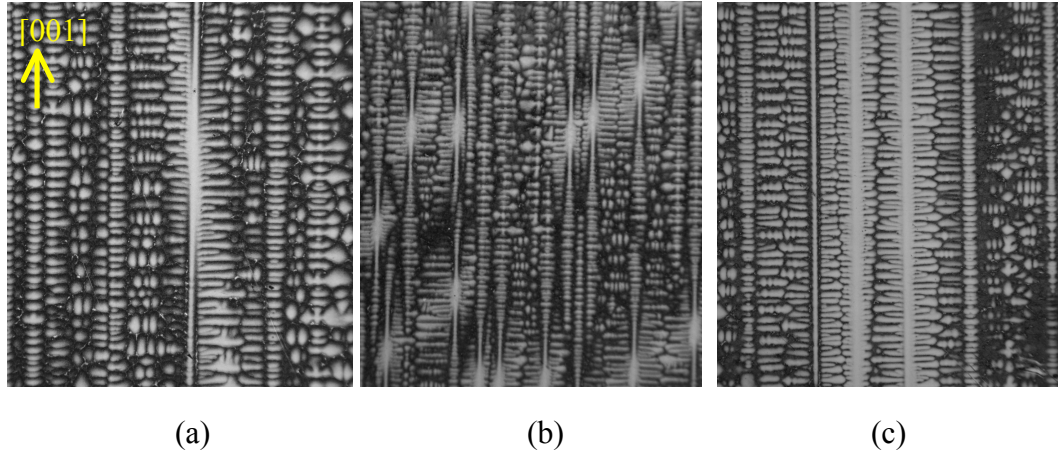
Figure 7.12 Micrographs of LMC solidified structures displaying the refinement in SDAS. Withdrawal rates are shown for (a) 8.5 mm/min, (b) 12.7 m/min and (c) 21.2 mm/min, solidified using the LMC process. Solidification direction is parallel to the plane of the page.
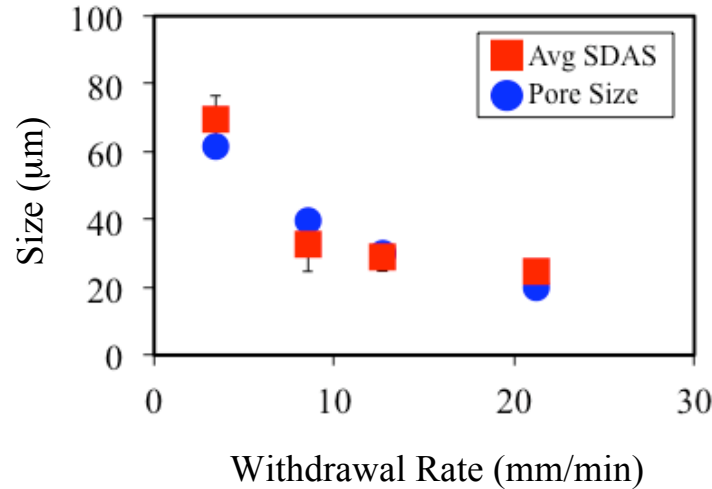
Figure 7.13 Dependence of maximum pore size and average SDAS on withdrawal rate for the LMC solidified bars at 8.5-21.2 mm/min and Bridgman cast bars at 3.4 mm/min. Each SDAS data point represents a total average measurement obtained only from nearby pore locations.

A relationship between the pore diameter and SDAS is displayed in Equation 7.19. This is an important finding since a correlation between average pore size and SDAS has not been previously presented in the literature for single crystal alloys.

$$d_{pore} = 1.15\lambda_2 \qquad\qquad [7.19]$$

It is evident that a relationship between cooling rate and maximum pore size is exists, which would connect the processing conditions to the fatigue initiating defect size. Solidification experiments have validated that the SDAS is related to the cooling rate (G

<center>198</center>

× *V*) and subsequent coarsening, which is equal to the thermal gradient (*G*) × solidification rate (*V*) as:[25]

$$\lambda_2 \propto \left(G \times V\right)^{-1/3} \qquad\qquad [7.20]$$

For this reason, the SDAS should reliable indicator of the overall cooling rate, thermal conditions and maximum defect size that limits the fatigue life, particularly in high gradient growth processes such as LMC.

Numerous studies of cast Al alloys have demonstrated that porosity is key factor that controls the fatigue properties.[26-28] Fatigue modeling of these alloys has focused on predicting the cyclic properties with a thorough characterization of the pore population in the material and obtaining a relation to SDAS. When the pore size strongly correlates to the fatigue life, the term dendrite cell size (DCS), analogous to the SDAS, is commonly used.[28-30] Here, the DCS is a measure of microstructure scale. Similar to single crystal directionally solidified alloys, pores within Al alloys correspond to the microshrinkage, which appears at the end of the solidification. The growth of these pores is geometrically hindered by the dendrites, which also provides tortuous shapes (low sphericity). This again supports the idea that single crystal fatigue life should be analyzed in terms of SDAS, or if possible cooling rate.

A plot of measured SDAS against an experimentally determined thermal gradient and solidification velocity using Equation 7.20 is shown in Figure 7.14.[31] As expected, extensive refinement is observed with faster cooling rates. It can be assumed that pore size reduction correlates with the refinement, until a limit is reached. Due to the extensive lateral growth of secondary dendrite arms, which occurs at velocities greater than 21.2 mm/min, the feeding of liquid within the interdendritic channels may be blocked during solidification, thus creating large voids. However, further solidification studies at higher growth rates are necessary to verify the details of this process.
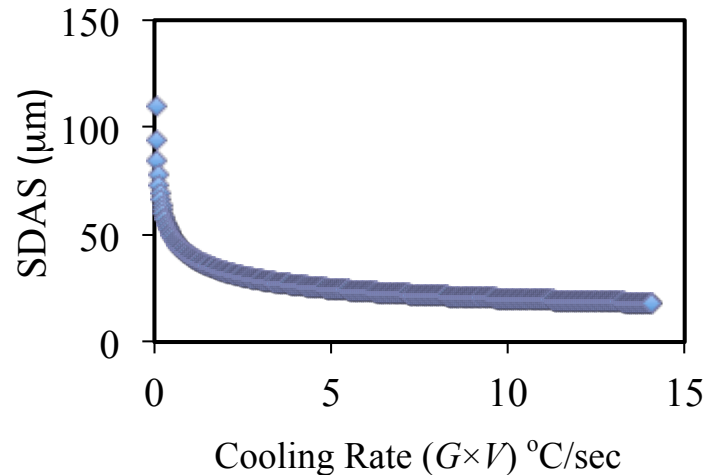
Figure 7.14 SDAS plotted as a function of experimentally determined $(G \times V)^{-0.33}$ for a single crystal nickel based superalloy cast with the LMC process.[31]

7.5   A Microstructure-Based Micromechanical Model

Using the micromechanical model presented in Section 7.1.1 and the relationship between fatigue life and average SDAS, the fatigue life can be represented as

$$N_T = 2.4 \times 10^6 \left(Y \Delta \sigma \sqrt{\pi \left(1.15 \lambda_2 \right)^{0.95}} \right)^{-2.4}$$

[7.21]

where N_T is the total life (crack initiation + crack propagation), Y is the geometric factor related to defect location, specifically 0.5 and 0.65 for internal and surface defects, respectively. For a range of stress levels, $\Delta \sigma$, the predicted fatigue curves are displayed in Figure 7.15 for two SDAS scales at $T = 538^{\circ}C$, assuming internal pores ($Y = 0.5$). The data points represent the actual lives for the given stress levels. Less scatter is observed in the data for the LMC solidified castings. The large scatter exhibited in the Bridgman castings was attributed to the interconnected pores, as indicated in Figure 7.15.
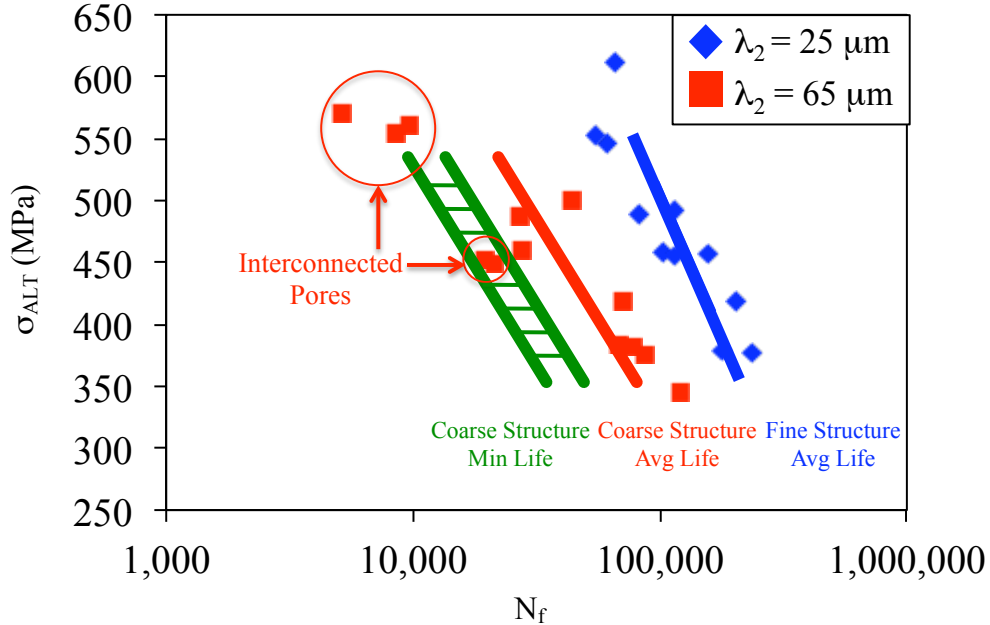
Figure 7.15 Predicted LCF lives for single crystal alloys subjected to various stress levels at 538°C (R = 0) for two average λ₂ scales. Actual data points are shown in the plot. Data points that contribute to the scatter in fatigue due to pore-pore interactions are highlighted.

To account for the scatter attributed to the adjacent pores, a scaling factor can be included as

$$N_f = 2.4 \times 10^6 \left(Y \Delta\sigma \sqrt{A\pi \left(1.15\lambda_2\right)^{0.95}} \right)^{-2.4} \qquad [7.22]$$

where A is the scaling coefficient for pore-pore interaction, which was found to lie between 1.5 and 2. The scaling coefficient was ascertained by measuring the ratios of maximum to minimum pore areas at the crack initiation site. A scatter band generated from the interconnected pores is displayed in Figure 7.15.

Understanding the influence of microstructure variability on the fatigue properties is key for the selection of processing parameters and design of materials for single crystal components. This micromechanical model demonstrates the feasibility of linking effects of microstructure variability on the cyclic plasticity scale of the intrinsic microstructure of a single crystal superalloy. A higher thermal gradient process that further refines the SDAS and pore size will shift the curves towards longer lives and reduced variability. This is especially relevant when considering design constraints of

201

single crystal blades during operation at a specific temperature. From the SDAS, one would have the capability of estimating specific stress levels that would initiate cracks after a specific lifetime. Following this logic, specific SDAS values can be targeted for various regions of the blade during directional solidification, such as the tip, blade, platform and root.

Combining the crack initiation model and crack growth law (Equation 7.15) allows one to extend the empirical model to predict fatigue lives of other commercial nickel-base superalloys. With alloy chemistry variation, the specific fracture energy (W_s), shear modulus (G), and crack growth material constants, C and m would likely increase or decrease, depending on the strength of the material. Studies on various 2nd generation single crystal Ni-base alloys have shown that the onset of crack initiation depends on the damage accumulation within the γ and γ' phases, as dislocations are able to readily penetrate the γ' precipitates.[32] The formation of stacking faults during LCF, typically observed in heavily alloyed single crystal compositions, can influence the fraction of slip irreversibility, f, defined as

$$f \Delta \varepsilon_p = \frac{\delta}{L}$$
[7.23]

and is based on the the fraction of plasticity emerging at the free surface.[33,34] Equation 7.23 corresponds to the amount of strain emerging after one cycle at the surface, where δ is the surface upset created by one cycle, L is the spacing between slip bands, and $\Delta \varepsilon_p$ is the applied plastic strain range. For N loading cycles, Equation 7.23 becomes

$$f = \frac{\delta^{cum}}{N \Delta \varepsilon_p L}$$
[7.24]

where δ^{cum} is the cumulative surface upset, typically measured with atomic force microscopy (AFM). With changes f, W_s, and G due to the variation in alloy chemistry, it can be expected that the coefficient, 2.4×10^6, in the model (Equation 7.22) will modify and produce a liner shift of the function, but leaving the slope unchanged.

To account the strength differences into Equation 7.22, the cyclic stress is normalized with the yield stress of René N5 and Hi-Ta alloys (Figure 7.16). Here the power-law scaling exponents for the René N5 and Hi-Ta alloys have similar values of -2.8 and -2.7, respectively. However, alloys such as DD32, SRR99 or CMSX-4, which contain much larger yield strengths, will cause a linear shift of the function up or down. Yet, the basic form and the slope should remain unchanged.

$$Y \times \frac{\sigma}{\sigma_Y}\left(\sqrt{\pi\sqrt{A_{defect}}}\right) \times 10^3 \, MPa$$
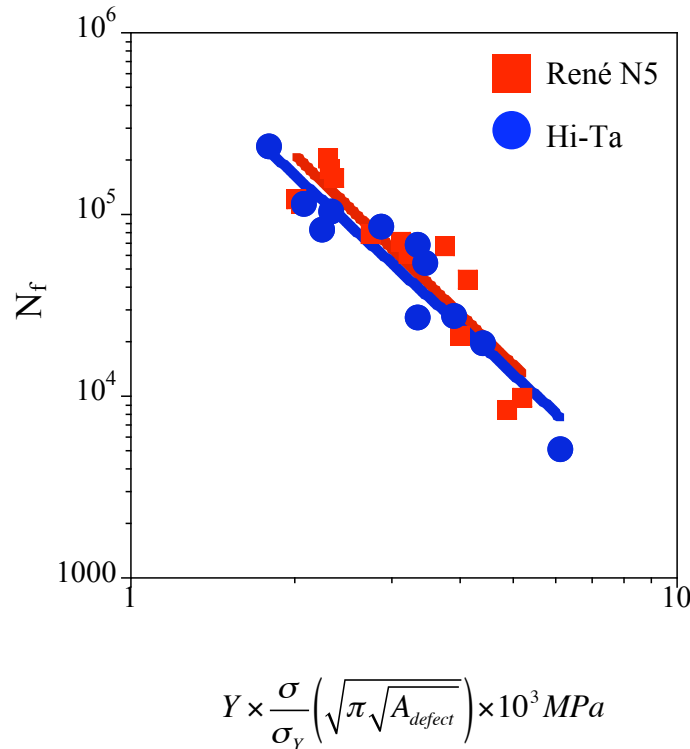
Figure 7.16 Lifetime vs normalized tensile stress with the yield strength of René N5 and Hi-Ta alloys.

Nonetheless, the main objective for turbine blade fatigue property improvement should focus on the relation of defect size to crack initiation life. From the information obtained from microstructure modeling of the solidification structure (Chapter 3), the spatial distributions of dendritic spacings can be predicted based on local thermal history. Generally a manufacturing analysis is initiated after the final design and lifetime prediction of an engine component are completed.[35] However, with the acquired modeling data, one can provide a more realistic fatigue property prediction and allow for extensive component design improvements by adjusting the processing variables and the

component dimensions. Again, this should include specific SDAS values and avoiding a breakdown of single crystal microstructure.

7.6   Benefits of Higher Gradient Casting on Fatigue Life

Figure 7.17 displays the fatigue life as a function of cooling rate for specific conditions: $T = 538^{\circ}C$, $R = 0$, $Y = 0.5$. The SDAS is also plotted on a separate axis. This unit is presented here to emphasize the tremendous increase in fatigue life achieved when scaling up a higher thermal gradient process or when reducing casting cross-section size, i.e. from small-scale to larger-scale industrial gas turbine (IGT) blades for power generation. The fatigue data points are shown for the Bridgman and LMC processed bars presented in Chapter 5, assuming internal initiations ($Y = 0.50$). The estimated fatigue lives for large-area cross-sections using data provided by Elliott[31] is indicated by the gray box in Figure 7.17.
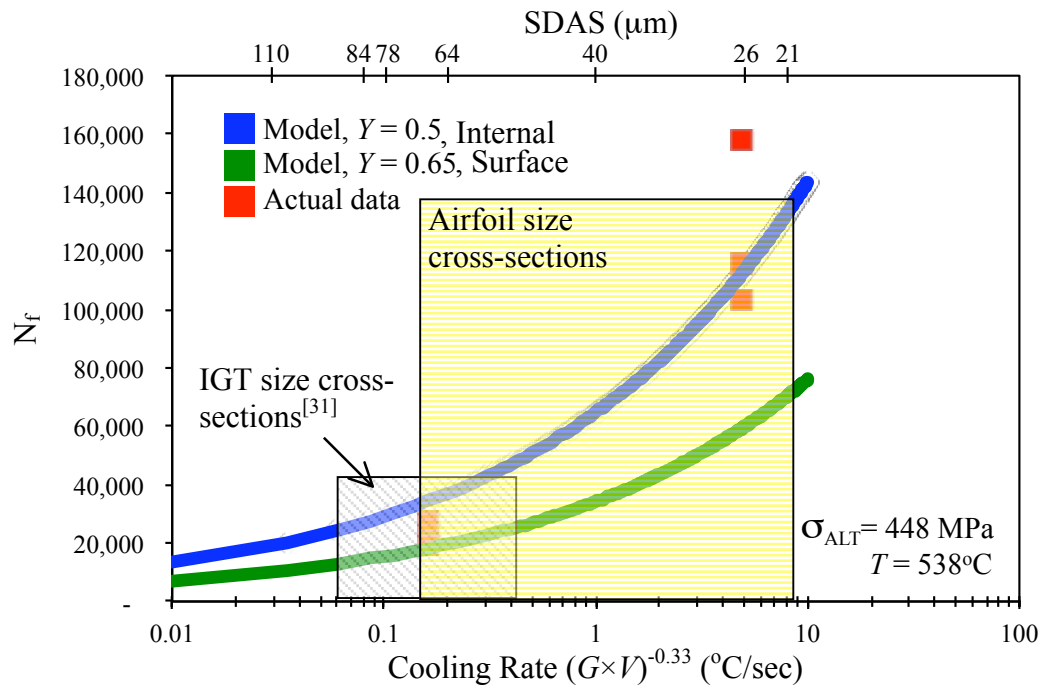
Figure 7.17 Fatigue life as a function of cooling rate for $T = 538^{\circ}C$, $R= 0$ applied to single crystal superalloys. Curve generated for internal initiation sites only.

Fatigue life curves for various stress levels are shown in Figure 7.18 for the same conditions as Figure 7.17. Shaded regions indicate the SDAS range for large IGT components and the target scales to airfoils. As expected, shorter lives are predicted for higher stress levels. A substantial benefit to the fatigue life is not expected at SDAS ≤ 18

μm for these conditions since there is a minimum pore size that can reside as the largest stress-concentrating defect in the material, in comparison to carbides.
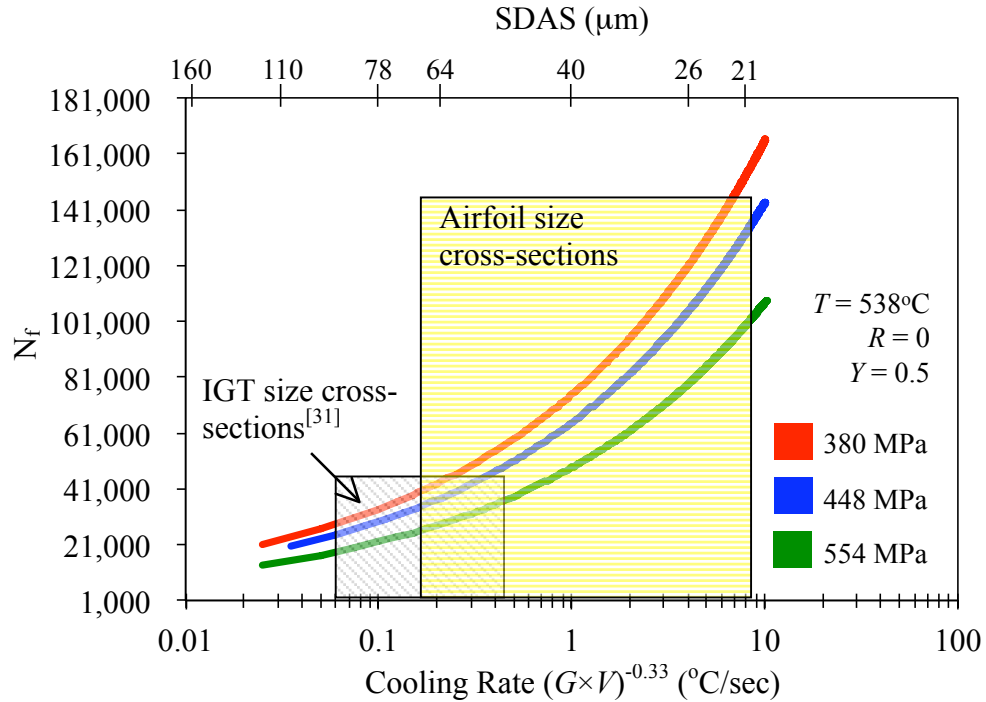
Figure 7.18 Predicted LCF life ($T = 538^{\circ}$C, $R = 0$) as a function of cooling rate for various stress levels. Curve generated for internal initiation sites only, $Y = 0.5$.

When the fatigue lifetime of single crystal component is critical, both for design decisions and subsequent system maintenance and support, the bounds for maximum, minimum and average properties are especially relevant. From a global standpoint, the utilization of this processing-structure-property model will hopefully decrease component design and process development costs and cycle time, lowering manufacturing costs, improving material life-cycle prognosis, and ultimately allow for a quick response to changing market demands.

7.6.1   Implications of a Processing-Property Model

The N_f vs cooling rate data is applicable to any higher thermal gradient solidification process that provides a refinement to dendritic spacings, as well as defect size. The curves presented in Figure 7.18 assume a homogeneous microstructure without a breakdown in single crystal microstructure and excessive lateral growth of secondaries. The model also assumes a longer crack initiation life in comparison to crack growth life,

considering crack initiation along crystallographic planes from internal pores within a component. The model is extremely useful for generating standards for evaluating material modification by including the minimum properties and statistical variability.

7.7   Summary

A micromechanical model was developed to predict the fatigue life by quantifying stress intensity factors based on flaw sizes and the relative distances from the surface. Improving single crystal fatigue properties should focus on reducing the maximum pore size to produce stress intensities far below the threshold of the material.

The stress level, cyclic plasticity at large pore sizes and their location with respect to the surface were critical factors of the micromechanical model. The stress dependence from both the crack initiation stage and the crack propagation period strongly contributes to the total life.

Stress intensities were found to be lower than published threshold stress intensity for LMC processed material, suggesting a significant crack initiation period during the fatigue process. A model for initiation, based on observed slip localization events, demonstrated similar stress dependencies in both initiation and growth phases. This model was formulated on the principles of slip band formation, which was attributed to the accumulation of dislocation dipoles on planar slip bands near casting pores. The crack initiation life was reasonably estimated by measurement of slip band features near pore initiating surfaces, and material parameters. These estimations were modified from slip band theories generally applied to polycrystalline alloys.

Changes in solidification processes that increase the cooling rate and produce homogeneous, dendritically-spaced, single-crystal microstructures will significantly benefit the fatigue life, as shown in this chapter by using the LMC process to obtain a 3-7X improvement. The developed model relating the cooling rate to the fatigue life will be applicable to a variety of alloys, component geometries and scales.

[1]   Y. Murakami: *Metal Fatigue: Effects of Small Defects and Nonmetallic Inclusions,* Elsevier Science, 2002.

[2]   J.-Y. Buffière, S. Savelli, P.H. Jounweau, E. Maire, and R. Fougères: *Mater. Sci. Eng. A,* 2001, A316, pp. 115-126.

[3]   Y.X. Gao, J.Z. Yi, P.D. Lee, and T.C. Lindley: *Fat. Fract. Eng. Mater. Struct.*, 2004, 27, pp. 559–70.

[4]   Y. Murakami and M. Endo: *Int. J. Fatigue*, 1994, 16, pp. 163–82.

[5]   K. Gall, M.F. Horstemeyer, B.W. Degner, D.L. McDowell, and J. Fan: *Int. J. Fract.*, 2001, 108, pp. 207–33.

[6]   C. Yablinsky: *PhD Thesis*, The Ohio State University, Columbus, OH, 2010

[7]   A. Sengupta, S.K. Putatunda, and M. Balogh: *J. Mater. Engng. Performance*, 1994, 3, pp. 540-550.

[8]   P.A.S. Reed and M.D. Miller: in *Superalloys 2008*, R.C. Reed, K.A. Green, R. Caron, T.P. Gabb, M.G. Fahrmann, E.S. Huron and S.A. Woodward, eds., The Minerals, Metals and Materials Society 2008, pp. 527-533.

[9]   W.J. Evans, R. Lancaster, A. Steele, and N. Jones: in *Superalloys 2008*, R.C. Reed, K.A. Green, R. Caron, T.P. Gabb, M.G. Fahrmann, E.S. Huron, and S.A. Woodward, eds., The Minerals, Metals and Materials Society, 2008, pp. 425-431.

[10]   K.S. Chan and T.-Y. Torng: *ASME J. Eng. Mater. Tech.*, 1996, 118, pp. 379-386.

[11]   K. Tanaka and T. Mura: *ASME J. Appl. Mech.*, 1981, 48, pp. 97-103.

[12]   P. Lukas and L. Kunz: *Mater. Sci. Eng. A.*, 2001, A314, pp. 75-80.

[13]   K. Tanaka and T. Mura: *Metall. Mater. Trans. A*, 1982, 13A, pp. 117-23.

[14]   T. Mura and Nakasone: *J. Appl. Mech.,* 1981, 57, pp. 1.

[15]   G. Venkataraman, Y.W. Chung, Y Nakasone, and T. Mura: *Acta Metall.*, 1990, 38, pp. 31.

[16]   M.R. Lin, M.E. Fine, and T. Mura: *Acta Metall.*, 1986, 34, pp. 619-28.

[17]   Q. Wang, C. Bathias, N. Kawagoishi, and Q. Chen: Int. J. Fat., 2002, 24, pp. 1269-1274.

[18]   H. Mughrabi, R. Wang, K. Differt, and U. Essmann: in *Fatigue Mechanisms*, J. Lankford, D.L. Davidson, W.L. Morris, and R.P. Wei, eds., ASTM-STP 811, 1983, pp. 5.

[19]   J.Z. Yi, unpublished research, 2006.

[20] C. Mercer, A.B.O. Soboyeho and W.O. Soboyejo: *Acta Mater.*, 1999, 47, pp. 2727-2740.

[21] M. Lamm and R.F. Singer: *Metall. Mater. Trans. A*, 2007, 38A, pp. 1177-1183.

[22] H. Weidong, G. Xingguo, and Z. Yaohe: *J. Cryst. Growth*: 1993, 134, pp. 105-115.

[23] W. Wang, P.D. Lee, and M. McLean: in *Modeling, Casting, Welding and Advanced Solidification Processes*, D.M. Stefanescu, J. Warren, J. Jolly, and M. Krane, eds., TMS, Warrendale, PA 2003, pp. 83-90.

[24] X. Wan, Q. Han, and J.D. Hunt: *Acta Mater.*, 1997, 10, pp. 3975-3979.

[25] W. Kurz and D.J. Fisher: *Fundamentals of Solidification*, 4th rev. ed, Trans. Tech. Publications, Enfield, NH, 1998.

[26] J.Z. Yi, Y.X. Gao, P.D. Lee and T.C. Lindley: *Metall. Mater. Trans. B*, 2006, 37B, pp. 301-11.

[27] X. Zhu, J.Z. Yi, J.W. Jones, and J.E. Allison: *Metall. Mater. Trans. A*, 2007, 38A, pp. 1111-1122.

[28] B. Zhang, D.R. Poirier, and W. Chen: *Metall. Mater. Trans. A*, 1999, 30A, pp. 2659-66.

[29] D.A. Lados, D. Apelian, and J.F. Major: *Metall. Mater. Trans. A*, 2006, 37A, pp. 2405-18.

[30] D.A. Lados and D. Apelian: *Mater. Sci. Eng. A*, 2001, 385, pp. 200-11.

[31] A.J. Elliott: *PhD Thesis*, University of Michigan, Ann Arbor, MI, 2005.

[32] K.S. Chan, J.E. Hack, and G.R. Leverant: *Metall. Mater. Trans. A*, 1987, 18A, pp. 581-591.

[33] S.E. Harvey, P.G. Marsh, M.D. Kriese, and W.W. Gerberich: *Scripta Metall. Mater*, 1995, 33, pp. 825.

[34] W.W. Gerberich, S.E. Harvey, D.E. Kramer, J.W. Hoehn: *Acta Mater.*, 1998, 46, pp. 5007.

[35] R.E. Schafrik, S. Walston: in *Superalloys 2008*, R.C. Reed, K.A. Green, R. Caron, T.P. Gabb, M.G. Fahrmann, E.S. Huron and S.A. Woodward, eds., The Minerals, Metals and Materials Society 2008, pp. 3-9.

Chapter 8

CONCLUSIONS AND RECOMMENDATIONS

The overall objective of this research was to evaluate the benefits of a high thermal gradient LMC solidification process for structure refinement and property improvement for section sizes relevant to aircraft engine airfoils. Previous research has demonstrated that this high gradient process can substantially reduce solidification defects in section sizes within large-scale IGT blades,[1-3] however, none of the prior LMC investigations have fully quantified the fatigue property benefits. This research has demonstrated that airfoils can be produced using new processes that produce higher quality next generation materials with fatigue properties that are improved through structure refinement. In this chapter, the key findings are first summarized. Following this, the implications for (1) LMC processing, (2) defect size reduction, (3) modeling of the microstructure, and (4) processing-structure-fatigue relationships are discussed along with recommendations for future research.

The key findings from a direct comparison of the Bridgman and LMC processes to grow single crystal prototype blades are as follows:

1. Up to a 50 pct refinement in PDAS was achieved at an intermediate solidification velocity of 12.7 mm/min using the LMC process for growing 1.6 cm diameter cylindrical bars.

    a. A distribution in dendritic spacings was produced with both Bridgman and LMC processes, with the smallest range in spacing exhibited at the optimal solidification rate (12.7 mm/min).

2. A limit to PDAS structure refinement was observed at a 12.7 mm/min solidification velocity, where the instability of the solid/liquid interface at faster rates increased the PDAS.

   a. Overgrowth of secondary arms and breakdown of the single crystal structure was observed at 21.2 mm/min due to the imbalance of axial and lateral thermal gradients.

   b. Greater control of the axial and lateral thermal gradients at faster solidification velocities will prevent lateral growth, single crystal breakdown, and produce homogenously refined microstructures throughout the entire component.

3. Increases in cooling rate with faster solidification velocities (>12.7 mm/min) further refined the SDAS and maximum pore size by over 70 pct, despite the increase in PDAS.

   a. The largest pores reside near the overall average λ_1, which is due to the competition between the final size of the γ/γ' eutectic pools and interdendritic liquid feeding.

   b. The SDAS more strongly correlates to the maximum pore size, than does PDAS.

4. The possible change in solidification path by the additional weight pct of refractory element, Ta, increased the maximum pore size for both LMC and Bridgman processes by up to 20 pct.

   a. A higher probability of pore agglomeration is present due to the precipitation of large, blocky TaC, impeding fluid flow between solidified dendrites during solidification.

   b. The presence of interconnected pores within the interdendritic area yields a lower degree of maximum pore size predictability within a component using SEV analysis.

5. The increase in Ta weight pct to the superalloy composition is useful to fatigue properties if pores can be suppressed.

210

6. Up to a 7X improvement in LCF life at 538°C was obtained using the LMC process at an optimal withdrawal rate, in comparison to Bridgman casting.

  a. Pore size drives the LCF life, where larger pores degrade the fatigue resistance. The strengthening benefits attained in the Ta-modified alloys compensated for the degradation of fatigue life with larger pores.

7. A micromechanical model developed Murakami and co-workers[4,5] was utilized to capture the initial stress intensity dependence from pore size and location on fatigue life.

  a. Smaller pores nucleated with LMC casting produced intensities well below the threshold, ΔK_{th}, which required more cycles to initiate cracks and produced long initiation lives according to the developed crack-initiation based model.

  b. The formulation of a crack initiation model, which extended the work of Tanaka and Mura,[6] was based on the accumulation of dislocation dipoles on planar slip bands near pore surfaces. Total life predictions incorporated the initiation-based model and the widely used Paris-Erdogen crack growth law, due to the similar crack growth rates exhibited at 538°C for fine and coarse scale microstructures.

  c. A model for initiation combined with propagation predicted fatigue life and demonstrated a similar stress dependence in both initiation and growth phases.

8. A model relating processing conditions, critical microstructure features and LCF life was developed to predict the fatigue life for a range of cooling rates. This model should be appropriate for predicting the fatigue life of various component sizes, dendritic scales, alloy chemistries and high gradient processes.

8.1 Advantages of LMC for Single-Crystal Airfoil Structure Refinement

Considering the experimental solidification results, it is quite apparent that the LMC process provides a substantial refinement for small-scale single crystal castings. This study has demonstrated that higher thermal gradient solidification processes can be practical for a range of geometries and scales.[1,7] Important aspects of the solidification

experiments were defining the limits of structure refinement with increasing thermal gradient, and identification of an optimal solidification velocity for growing homogeneous structures throughout the entire cast bar. Maintaining a planar solid/liquid interface at the baffle line at faster solidification velocities is a critical factor to increasing the cooling rate and growing finer scaled single-crystal components. Achieving a balance between the axial and radial thermal gradient using a tin-coolant ($T_m = 232^{\circ}$C) with the LMC process is crucial to preventing overgrowth of secondary arms and grain nucleation within the casting.

Higher cooling rates, attributed to the faster withdrawal speed, were successfully achieved using LMC for improved heat extraction. The primary and secondary dendrite arm spacings were found to decrease by 50 and 60 pct, respectively, for the 1.6 cm diameter rods at the optimal solidification rate for the investigated experiments. The 65 pct reduction in crack initiating defect size was the major factor in obtaining a 7X increase in LCF life at 538°C. More importantly, a quantitative relationship between processing conditions and defect size was established, due to the strong dependence of pore size on cooling rate. It should be emphasized that is a newly ascertained relationship for single crystal superalloys.

The increased weight pct of Ta to the René N5 alloy chemistry did not affect the primary or secondary dendrite arm spacings for either Bridgman or LMC processes. The ability of LMC casting to reduce segregation of refractory content single crystals, eliminate freckle defects, while providing superior strengthening benefits presents a promising manufacturing process for future turbine blade alloy development for overall mechanical property advancement. However, the solidification experiments identified the detriment of increasing the weight pct of Ta due to increased defect size. Minimizing this effect should provide further increases in fatigue life due to the strengthening benefits by resisting shearing of γ' precipitates. Due to the increase in the maximum pore size within the Ta-modified material and the similar fatigue lives exhibited, one may question the worthiness of utilizing this refractory element. Figure 8.1 addresses the creep life benefits using Ta-modified alloys for various stress levels at 982°C. It is obvious that alloy chemistry modification benefits creep life in comparison to refinement in dendritic

scale for the investigated geometry. The two scales presented are solidified with the LMC and Bridgman processes using rates of 12.7 mm/min and 3.4 mm/min, respectively.

(a)

(b)

(c)
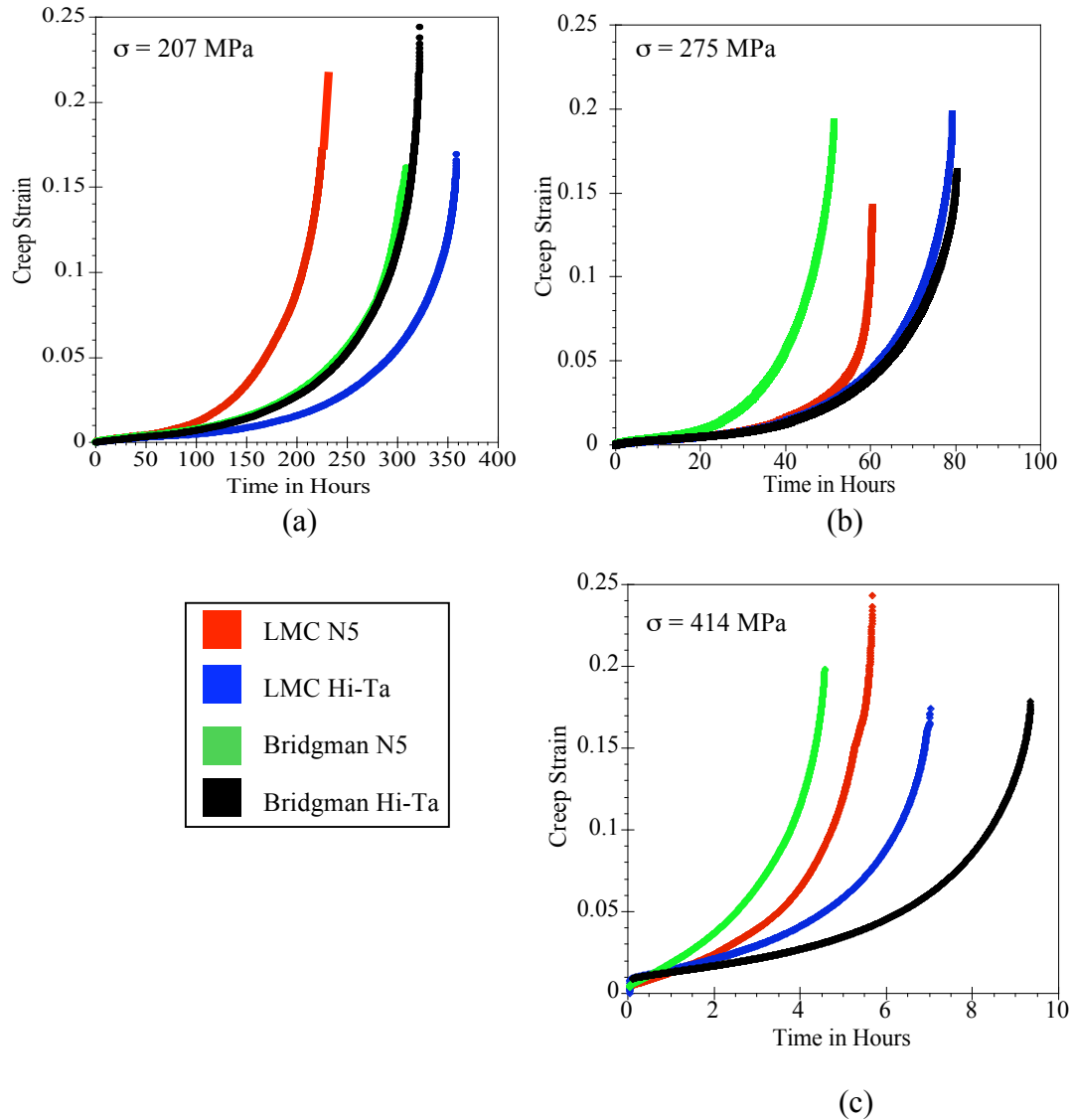
Figure 8.1 Creep lives for the four variants investigated at (a) 207 MPa, (b) 275 MPa and (c) 414 MPa at 982°C. LMC solidified alloys contain SDAS = 25 μm, whereas Bridgman solidified alloys = 65 μm.

Balsone *et al.*[8] also found the benefits of using LMC for improved fatigue life and reduction of scatter for hold-time fatigue (Figure 8.2) at a higher temperature of 871°C. It should be emphasized that since creep and fatigue are both important factors to increasing the overall life of a component, a combined approach employing a high gradient solidification process with alloying to improve both creep and fatigue properties is likely to yield maximum performance benefits.

Strain Controlled LCF
T=871°C, F=0.333Hz, Hold time=2min, A=-1
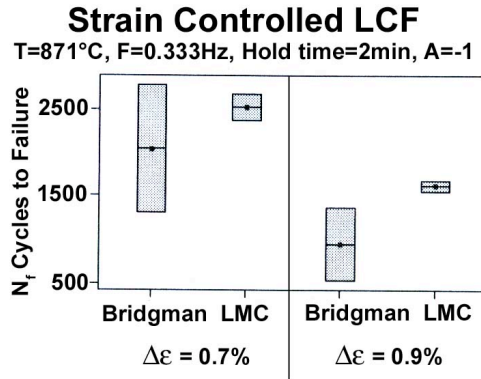
Figure 8.2 LCF lives of Bridgman solidified and LMC solidified material at 871°C. The box plots indicate the average value (small black square) and standard deviation (the shaded region) for each test condition.[8]

8.2   Optimization of Processing Conditions for Defect Size Reduction and Variability

Extensive statistical analyses of microstructures solidified at 8.5, 12.7 and 21.2 mm/min withdrawal rates demonstrated the existence of a range of primary dendrite arm spacings and pore sizes throughout a solidified bar.   This is a new finding since most dendrite studies and production quality control measurements solely employ an average spacing value to characterize an entire section. A vital link between the heterogeneity in dendritic spacings and the maximum pore size was obtained in this study.   This was accomplished through modeling of the microstructure using a uniquely developed Matlab code, which incorporated Voronoi tessellations.   Using the X-Y coordinates of primary dendrite cores and pore locations, Voronoi-dendrite maps were speedily processed from metallographic as-cast sections from various regions of a cast bar.   From this analysis, valuable microstructural information of a post-cast section was obtained including:

1. The maximum, minimum, average and full range of PDAS for a given area

2. Quick estimates of the variation in spacings radially (edge versus center) in order to give insight to the solid/liquid interface conditions during solidification

3. Identification of the preferred locations for solidification shrinkage pores within the dendritic structure

4. The occurrence of large, adjacent pores that increase the stress intensity and enhance local cyclic plasticity.

214

It should be noted that due to the variation in geometry of a casting, there might be local differences in PDAS in regions such as the platform, tip, root or blade. Analysis of the variation in spacings at various areas can assist in adjusting processing parameters for a specific location to produce a more dendritically homogeneous part.

An example of the practicality of Voronoi-dendrite maps to airfoil microstructure analysis is shown in Figure 8.3. If the biaxial or triaxial stress state of the blade is known, the pore size distributions can be integrated into the stress analysis process. Additionally, non-destructive methods that enable locating pores within the dense superalloy microstructure can be introduced.
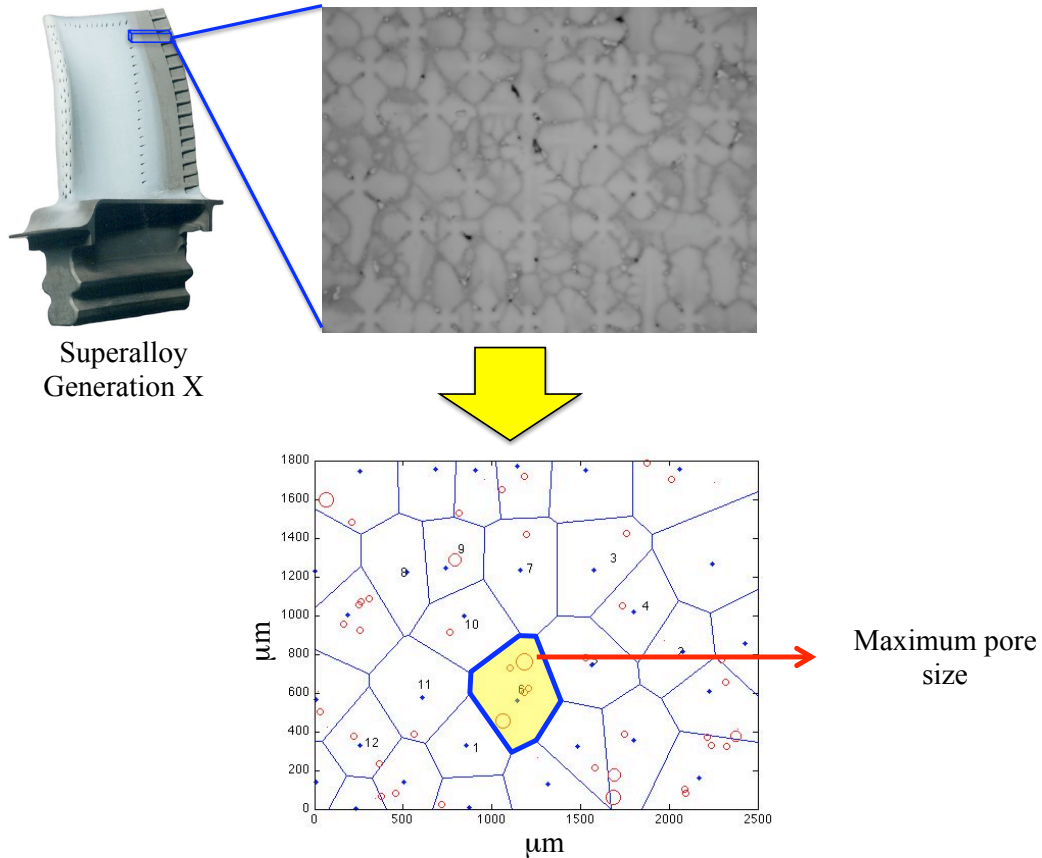

Figure 8.3 Illustration of the feasibility of implementing microstructure modeling on an as-cast airfoil using Voronoi-dendrite maps.

8.2.1   New Methodologies to Predict Maximum Pore Size

Due to the range in pore size produced during solidification processing, statistical formulae along with stereology provided a reasonable estimation of the maximum pore

215

size within a predicted volume. The pore characterization techniques described in this thesis will be advantageous during the manufacturing of these alloys since nondestructive inspection procedures must be applied to assure component quality. When it is of particular importance to identify the minimum fatigue properties of a component, use of the statistics of extremes (SEV) can provide a lower bound of fatigue properties. This technique will increase the probability of measuring the largest defect size and aid in adhering to design constraints, which in some cases require a limit to the maximum allowable size. Currently, the maximum pore is discovered through random and tedious metallographic sectioning. The SEV method will likely reduce time, costs, avoid destruction of material, and increase accuracy.

A relationship between dendritic spacing and pore diameter was found to correlate more strongly to the SDAS. This was attributed to the dependence of cooling rate on SDAS, and close relation of PDAS to the thermal gradient. Therefore, when aiming to employ a higher thermal gradient process for defect size reduction, the focus should reside on refining the SDAS, while simultaneously avoiding breakdown the single crystal structure.
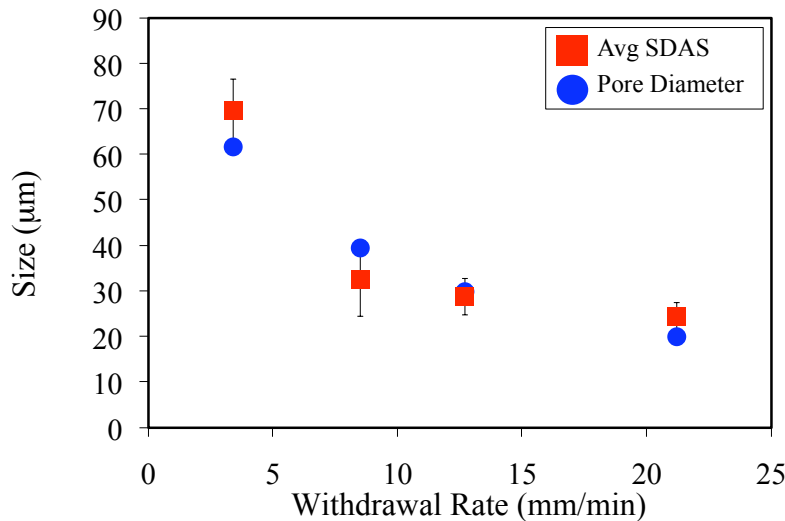
Figure 8.4 Relationship between SDAS and pore size for various solidification conditions.

8.3   Impact of Defect Size on Single Crystal Fatigue

The 3-7X increase in LCF life at 538°C ($R = 0$) was owed to the 65 pct refinement in maximum pore size using the LMC process ($V = 12.7$ mm/min), in comparison to

Bridgman (V = 3.4 mm/min) casting. It should be noted that these rates were selected for comparison because they provided the most refined and homogeneously distributed microstructures. However, an important finding was that the optimal LMC solidification rate may not have achieved a minimized pore size.

It has been determined that for the single crystals investigated, the fatigue life is pore size driven, yielding an initiation life in excess of 90 pct of the total life. Smaller pores were found to initiate cracks, all from internal locations, within the refined microstructure at all stress levels below σ_y. Calculated stress intensities associated with pore sites revealed that the finer-scaled pores contributed to producing stress intensities far below the threshold. Thus, crack initiation, rather than crack growth constituted the major fraction of fatigue life for the conditions investigated. Pores that initiated cracks from intensities close to the threshold, coincided with near-to-surface initiations; in these cases the fatigue life is dominated to a greater extent by crack growth. These findings could be incorporated into design and life prediction schemes that explicitly consider maximum predicted pore sizes within an as-cast component.

Crystallographic cracks emanated from pores at internal locations within the specimen for both microstructure scales. At higher applied stress levels, cracks initiated from pores closer to the specimen surface. Near-to-surface initiations, initiating Mode I opening cracks, occurred at σ_{ALT} > 551 MPa within the Bridgman solidified material. From a design perspective, the capability of initiating pores from locations further from the surface will increase the fatigue life. It is hoped that this new finding will assist in adjusting the current stress tolerance limits when employing higher thermal gradient casting processes.

A high probability of initiating cracks from mutually interconnected or nearby pores was prevalent in the Ta-modified cast specimens at all stress levels. These sites were found to nearly triple the predicted size, which was estimated with SEV. The detriment of amplification of intense slip localization during fatigue due to pore-pore interactions was offset by the increasing the resistance to shearing of γ' precipitates due to Ta addition. This is of significant importance for designing newer alloys that aim for

strength increase, yet produce larger defects due to the inherent solidification path attributed to the alloying elements.

For generating a fatigue life model that incorporates both crack initiation and crack growth stages, crack growth studies using X-ray techniques were successfully conducted at elevated temperatures. Similar crack growth rates were exhibited at 538°C for both microstructure scales. The crack growth studies along with fractographic analysis have determined that microstructure refinement influences the crack initiation stage more strongly than propagation. Therefore, a microstructure-based fatigue initiation model that captured the stress and defect size dependence was utilized to complement the typically used Paris-Erdogen crack growth law. As a result, two modeling approaches were presented for predicting the fatigue life: a fracture mechanics-based approach and an initiation model that supported fracture mechanics correlations. These studies have demonstrated that a model that assumes a long initiation life from internal defects is crucial for more accurate life predictions of single crystals grown with higher thermal gradient processes. The traditional approach of using modified crack propagation equations to estimate the single crystal fatigue life will no longer be valid with an extended initiation life. It can also be assumed that a single crystal subjected to a HIP process, producing significantly smaller pores, can benefit from the crack initiation model. However, the literature has suggested that HIPing single crystals may produce recrystallization and re-formation of pores during the post-HIP heat treatment process.[7] Thus, higher gradient casting processes that produce smaller pores is a more reasonable means of increasing the fatigue life.

8.4   Processing-Structure-Fatigue Relationships

New relationships between the processing conditions, defect size, stress level and fatigue life at 538°C were developed and integrated into a model in order to generate practicable fatigue life predictions in terms of cooling rate. This model illustrated the significant benefit to employing higher thermal gradient casting processes to increase the fatigue life for a range of dendritic scales. This model is applicable to a range of alloy compositions, geometries, component scales and processes.

One can envision the benefits to improving the fatigue life when applying this model to large IGT blades, which currently possess average PDAS values of approximately 600 μm.[7] Laboratory scale LMC experiments shown in Elliott *et al*.[1] demonstrated a significant refinement in both PDAS and SDAS with higher cooling rates using various processing conditions for large area cross-sections. However, the fatigue life benefits were not evaluated for a range of dendritic scales. Taking into account the SDAS data acquired from large area cross-sections, shown in Figure 8.6, the developed model can estimate the fatigue life without performing tedious pore size measurements on the sections.

Figure 8.5 Average PDAS measurements plotted as a function of section thickness. Various withdrawal rates and casting parameters were employed to generate this plot.[1]
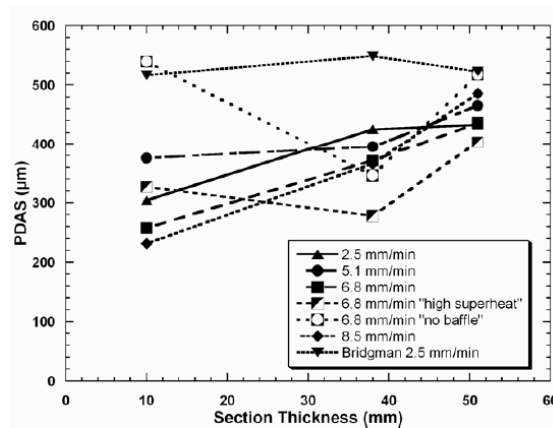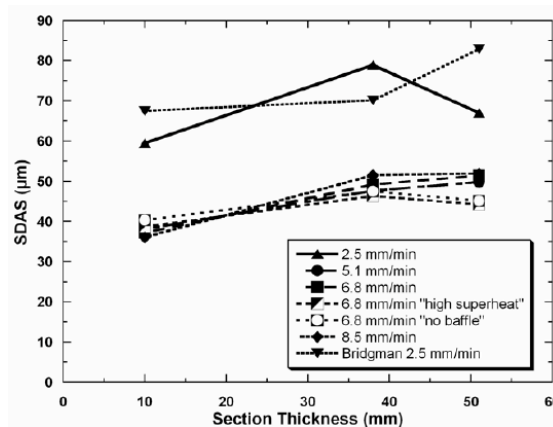

Figure 8.6 Average SDAS measurements plotted as a function of section thickness. Various withdrawal rates and casting parameters were employed to generate this plot.[1]

The developed connections between cooling rate, dendritic scale and defect size should be useful for evaluating advanced directional solidification processes, such as gas

cooling casting (GCC),[9] fluidized-bed quenching (FBQ),[10] zone intensified overheating and melting and liquid metal cooling (ZILMC or ZIOLMC).[11,12] These processes have emerged to elevate the thermal gradient in order to meet the requirements of industrial gas turbine efficiency. An example of refinement in dendritic scale using the ZIOLMC process is shown in Table 8.1. It should be noted that while some of these techniques are currently being investigated on a laboratory scale. It is hoped that the processing-structure-fatigue model developed in this thesis will assist in advancing these techniques for eventual use for production.

Table 8.1 Values of thermal gradient, T, PDAS (λ_1) and SDAS (λ_2) for various solidification rates using ZIOLMC for growing single crystal DZ125 superalloy.

V (μm /s)	50	100	255	500	800
T (K/s)	2.53	5.15	13.17	24.88	36.4
$\lambda 1$ (μm)	94±2.1	79.5±2.3	65.8±1.7	43.2±1.8	35.8±0.52
$\lambda 2$ (μm)	18.4±0.5	17±0.5	12.8±0.4	9.3±0.2	7.3±0.2

The nonlinear regression equation representing the PDAS (λ_1) was shown as

$$\lambda_1 = -0.00226 + 0.6082G^{0.5}V^{-0.25}$$ [8.1]

and SDAS was represented as

$$\lambda_2 = 0.00039V^{-0.3}$$ [8.2]

Using the relationship shown in Chapter 7 as

$$d_{pore} = 1.15\lambda_2$$ [8.3]

Clearly a significant refinement is observed with the ZIOLMC process for the small diameter bars (0.7 cm) with increasing solidification rate (0.3 to 48 mm/min). It should be noted that the diameter for the study was smaller than the samples tested in this thesis (1.6 cm). By using the processing-structure-property model, predicted fatigue lives for these specimens would be greater than 160,000 cycles at $\sigma_{ALT} = 448$ MPa. However, it is uncertain as to whether such small pores would be the largest defect in the microstructure at this scale. Nonetheless, the processing-structure-property model

developed in this thesis can assist in evaluating and employing newer high gradient casting processes for the production of newer materials.

8.5 Implications and Recommendations for Higher Gradient Processes

LMC investigations targeted to fabricate airfoils with improved fatigue properties show promising results for the manufacture of newer single crystal materials. The successful use of a higher gradient casting method to grow single-crystal components is contingent upon overcoming processing problems such as defect formation, and maintaining microstructural stability once in service. The increased number of elemental additions in a Ni-based superalloy and the complex interactions of these additions reveal a need to investigate elemental variation effects on microstructural stability, phase transformation temperatures, and solidification-induced segregation. Due to the increase in defect size that can arise from MC carbide precipitation from Ta additions, one may consider employing thermodynamic modeling using Scheil-type analysis to manipulate the solidification path. Additionally, the developed relationships connecting processing conditions, dendritic homogeneity, and solidification defect sizes are relevant factors to incorporate into solidification modeling software, such as ProCast^{TM}.

From a processing standpoint, control over the solid/liquid interface when employing faster cooling rates is critical to attaining the most refined homogeneous microstructures for complex airfoil components. An accomplishment of this research includes the identification of important solidification parameters that should be further analyzed to reduce defect formation.   If the solid/liquid interface is not planar and drifts away from the baffle zone during casting, a large spatial distribution in properties may arise. Additionally, lateral growth may occur at faster rates. For the purpose of improved quality control of single crystal parts, Voronoi-dendrite pore maps and SEV analyses provide a valuable means of determining the range of properties for an entire component. Adjustment of quality control and damage tolerance standards can be applied with the implementation of both of these techniques.

When aiming to improve the fatigue properties, manufacturing processes should focus on achieving cooling rates that refine defects within the dendritic structure. The

LMC process is a viable means to accomplish this. Structure refinement provides benefits via delaying the onset of fatigue crack growth, thus new approaches to predicting cyclic life may be required. Therefore, the current focus on understanding crack propagation in single crystal superalloys should shift to investigating initiation mechanisms, particularly in newer, fatigue-resistant alloys.

The initiation model described should be applicable to a range of pore sizes that initiate cracks at intensities below or near the threshold. Additionally, if initiations emanate from carbides, the model can simply be modified for inclusion cracking. It is suggested that for further improvement of the LCF life, one should focus on modeling strain localization with detailed consideration of the role of precipitate shearing. Furthermore, since these turbine parts operate in extremely aggressive environments of high velocity hot combustion gas-air mixtures carrying highly corrosive ingredients at high pressures, it is especially crucial to maximizing the strengthening benefits from alloy chemistry modification, weighed with the competing influence of solidification path and the formation of fatigue-initiating defects.

The solidification experiments, spatial distribution modeling and fatigue property relationships discussed in this thesis will ultimately bridge the gap between solidification processing, microstructure characterization and mechanical property design for single crystals. It should be noted that materials design for achieving higher turbine entry temperature for increased fuel efficiency is an extremely challenging process. Continued development of processing-structure-property models to accelerate this process is essential for rapid progress.

8.6   Recommendations & Future Research

The solidification experiments, microstructure modeling and fatigue results have demonstrated that improved fatigue properties can be obtained by increasing the cooling rate during solidification to refine the microstructure. Yet, improved understanding of single crystal superalloys from each area (processing vs microstructure analysis vs mechanical properties) can aid in generating a total life model (fatigue life + creep life + oxidation), which would provide significant benefits to the industry. This section will

discuss the future directions to consider in order to further improve the high temperature capabilities of advanced single crystal turbine performance.

8.6.1 Solidification Modeling

Consideration of the fundamental features of the LMC solidification process has motivated investigations of physically-realistic process models using ProCast solidification software packages. Miller[13] has utilized ProCast to generate physically-reliable sets of 3-D finite-element (FE) solidification model parameters that captured the physics of the LMC and Bridgman process for growing single crystals.   By integrating processing parameters and defect size data obtained in this thesis, further optimization of higher gradient processes can be achieved to generate preferred thermal fields during solidification.

With regard to developing newer refractory-containing alloys with improved mechanical properties, one can incorporate thermodynamic modeling to minimize the nucleation and/or precipitation of defects. This thesis has identified the key factors that contribute to defect formation, therefore, it is necessary for future work to include modeling approaches that minimize these effects and maximize the strengthening benefits to resist fatigue damage.

8.6.2 Microstructure Evaluation

The unique characterization techniques presented in this thesis have shown that variability in microstructure (dendrite arm spacings and interdendritic solidification feature size) contributes to the scatter in fatigue life. It is recommended that porosity measurements at various cooling rates along with fatigue experiments should be conducted to further validate the processing-structure-property model. Applying the SEV analysis to predict the maximum defect size in an actual airfoil component should be involved in future work. Incorporating the maximum defect size predicted with SEV into the model, rather than an average pore size, should be an item of future work as well.

Performing Voronoi analysis on large-area cross-sections, relevant to the size of IGT blades, will indefinitely verify the applicability of this technique to the industry.

Large turbine blades have complex geometries, which require varying solidification conditions in specific locations in order to maintain a dendritically homogeneous component. Voronoi analysis can become an asset to performing quality control on single crystal parts post-solidification and identify deviations in PDAS, problems in unexpected areas, and trends in shrinkage pores. Using solidification modeling and dendrite mapping with Voronoi tessellations to understand the conditions that promote the most homogeneous microstructures with minimal defects is crucial to extending the crack initiation life. Future work should combine ProCast modeling and Voronoi mapping to identify and reduce favorable defect nucleation sites within a casting for a variety of compositions.

Acquiring 3-D data sets of porosity within the single crystal Rene N5 and Ta-modified alloys would be useful to validate the SEV approach. 3-D microstructural analysis of René N5 alloys to understand the conditions under which 3-D pores form would be valuable for solidification-defect modeling. Moreover, it would be valuable to obtain a 3-D view of the agglomerated pores within the Bridgman Ta-modified alloy to understand their relationship to the dendrite structure and carbide formation.

8.6.3   Mechanical Property Assessment

It is clear that the LMC process can improve the LCF and HCF resistance of single crystal alloys, yet its impact on creep, stress rupture and thermo-mechanical fatigue benefits have not been fully addressed for airfoils. To assess a component's total life and durability, extensive high temperature creep, thermo-mechanical and tensile testing of single crystal specimens should be conducted. Once these properties are acquired from the refined single crystals, a total life model can be generated. Additionally, fatigue testing at higher temperatures will validate the model for a range of temperatures. Fatigue testing at temperatures higher than $720^{\circ}C$, where the mode of cracking may change from mixed-mode to Mode I opening behavior, should be considered.

A better understanding of crack initiation process, arising from the intense slip localization near pores, can be obtained by performing additional electron microscopy

studies, especially transmission electron microscopy (TEM). Detailed measurements of slip band spacing and dislocation density within the bands, near pores would further improve the model by adding a factor relating dislocation arrangement to the relevant features of pores. This would be a useful discovery since it is still unclear whether the slip band formation favors pore size or certain geometric aspects of pore surfaces.

Understanding the impact of stronger and refined alloys on the deformation mechanisms at the scale of precipitates, and within the plastic zone ahead of a crack tip, will allow for appropriate design changes. *In-situ* strain mapping near defects during cycling would enable one to correlate the number of cycles to initiation to the slip band formation and strain development to validate the initiation model. This could be performed on thin-sheet material, using digital image correlation analysis.[14]

Additionally, improvement to the initiation model can be achieved with finite element modeling (FEM) of the plastic shear strain influence on slip band formation near pore surfaces at various stress levels and temperatures. This has been performed by Fan *et al*.[15] on polycrystalline Al alloys and described in Chapter 7 for a specific stress state and temperature. Modeling parameters should include: pore size and geometry, fracture energy, elastic modulus, yield strength, temperature, stress level, frequency and *R*-ratio for various alloy compositions.

[1] A.J. Elliott: *PhD Thesis*, University of Michigan, Ann Arbor, MI, 2005.

[2] P.N. Quested and S. Osgerby: *Mat. Sci. Technol*. 1986, 2, pp. 461-475.

[3] A. Kermanpur, M. Rappaz, N. Varahram, and P. Davami: *Metall. Mater. Trans. A*, 2000, 31B, pp. 1293-1304.

[4] Y. Murakami: *Metal Fatigue: Effects of Small Defects and Nonmetallic Inclusions*, Elsevier Science, 2002.

[5] Y. Murakami and M. Endo: *Int. J. Fatigue*, 1994, 16, pp. 163–82.

[6]   K. Tanaka and T. Mura: *ASME J. Appl. Mech.*, 1981, 48, pp. 97-103.

[7]   M. Lamm and R.F. Singer: *Metall. Mater Trans. A*, 2007, 38A, pp. 1177-1183.

[8]   S. Balsone, G. Feng, and J. Schaeffer: in *Solidification Processes and Microstructures*: *A Symposium in Honor of Winfried Kurz*, M. Rappaz, C. Beckermann, and R. Trivedi, eds., TMS, Warrendale, PA, 2004, pp. 77-83.

[9]   M. Konter, E. Kats, and N. Hofman: in *Superalloys 2000*, T.M. Pollock, R.D. Kissinger, R.R. Bowman, K.A. Green, M. McLean, S.L. Olson, and J.J. Schirra, eds., TMS, Warrendale, PA, 2000, pp. 189-200.

[10]   Y.G. Nakagawa, Y. Ohotomo, and Y. Saiga: in *Superalloys 1980*, J.K. Tien, S.T. Wlodek, H.I. Morrow, M. Gell, and G.E. Maurer, ASME, Metals Park, OH, 1980, pp. 267-274.

[11]   H.Z. Fu and L.Liu: *Mater. Sci. Forum*, 2005, 475-479, pp. 607-612.

[12]   H.Z. Fu, X.G. Geng: *Sci. Tech. of Adv. Mater.*, 2001, 2, pp. 197-204.

[13]   J.D. Miller: *PhD Thesis*, The University of Michigan, Ann Arbor, MI, 2010.

[14]   H-J. Pohl, O. Weibrecht, and U. Wiesenburg: US Patent # 3997795, 1976.

[15]   J. Fan, D.L. McDowell, M.F. Horstemeyer, and K.A. Gall: *Engng. Fract. Mech.*, 2003, 70, pp. 1281-1302.